The Dissertation Committee for Will A. Goth Certifies that this is the approved version of the following Dissertation:

RAPID WIDE-FIELD IMAGING OF SOFT-TISSUE MICROSTRUCTURE

Committee:

James W. Tunnell, Supervisor

Michael S. Sacks, Co-Supervisor

Thomas E. Milner

Krishnaswamy Ravi-Chandar

RAPID WIDE-FIELD IMAGING OF SOFT-TISSUE MICROSTRUCTURE

by

Will A. Goth

Dissertation

Presented to the Faculty of the Graduate School of

The University of Texas at Austin

in Partial Fulfillment

of the Requirements

for the Degree of

Doctor of Philosophy

The University of Texas at Austin

December 2018

In memory of my father, Paul R. Goth.

Acknowledgements

I'd first like to acknowledge both of my graduate supervisors, Dr. James Tunnell & Dr. Michael Sacks, for their mentorship and guidance during the past five years, as well as the flexibility in pursuing a wide variety of personal interests and applications of my research. I was fortunate to work with such thorough and thoughtful academic mentors. Additionally, I would like to thank my committee members Dr. Thomas Milner and Dr. Krishnaswamy Ravi-Chandar, who have been invaluable resources for completing my thesis work. I have also had the privilege of working with a number of impactful mentors throughout my undergraduate and graduate years. In particular, I'd like to Dr. Charles DiMarzio, Dr. Eman Namati, and Dr. Giuliano Scarcelli, each of whom contributed greatly to pursuing graduate school and obtaining my graduate degrees.

All of the members of the Biophotonics Lab I have had the fortune of overlapping with have been instrumental in shaping my day-to-day life in graduate school. Between lab lunches, collaborative projects, and inclusion in a variety of cultural events, sharing my time here with you all has been inspiring and enjoyable. To Manu Sharma, Varun Pattani, Sam Lim, Bin Yang, Ricky Hennesy, Xu Feng, Austin Moy, Andrew Stier, Yao Zhang, Hieu Nguyen, Susie Torres-Hurtado: thank you!

There were also a number of undergraduate students who deserve recognition for their help: Reece Stevens, my first undergraduate assistant, who set a high bar to match for all those that followed; Mason Dana, whom I met on my first day in Austin at soccer club tryouts, and eventually worked alongside as he began preparing for medical school; and finally Tyler Chinn and Justin Fasman, who have helped this past summer in making sure my systems are useable after I leave. To each of you, along with all the others I have been a TA for or mentored, I hope our work together provided you at least a small amount of

the opportunities that my mentors provided me; I certainly learned a lot about mentorship and management from our experiences.

I have also worked with a number of other people in the **WCCMS** and the **BME** department who have helped me immeasurably in my dissertation work. I had extensive and productive collaborative work with Dr. Alicia Allen, who taught me about polymer fabrication and characterization, and made electrospun fiber samples for me to validate my imaging system. Dr. Salma Ayoub and Dr. Dwight Romanovicz both helped me learn the ropes for SEM imaging of many different samples. Sam Potter has been instrumental in tissue preparation and imaging of heart valve leaflets for my dissertation work, along with being a much appreciated resource for good-natured venting about graduate school. And last but certainly not least, the lab managers of the **WCCMS** – John Lesicko, Jordan Graves, and John Carruth – have all been phenomenal resources of knowledge and thoroughly enjoyable to work with closely.

Finally, I would like to acknowledge my family. To my late father, Paul, whose footsteps I've unintentionally but proudly followed here at UT – I wish you could be here to see what you've inspired. To my older sister, Andrea, who has been a benchmark for both intellect and adventure throughout my life. To my mother, Brenda, who has sent an unending stream of love and support, and has commiserated and celebrated every step of the way with me. And finally to my girlfriend Nicole, who has stuck with me from afar and supported me unwaveringly over these past five years – I can't wait to be close to you again! I love you all, and am excited to begin this next chapter of my life with you.

Abstract

RAPID WIDE-FIELD IMAGING OF SOFT-TISSUE MICROSTRUCTURE

Will A. Goth, Ph.D.

The University of Texas at Austin, 2018

Supervisor: James W. Tunnell

Co-Supervisor: Michael S. Sacks

Tissue microstructure is pivotal in determining the function, behavior, and disease state of biological tissues. Histology and advanced optical techniques are commonly used to examine the cellular, extracellular, and subcellular constituents that define tissue microstructure. However, these techniques frequently require tedious and destructive tissue preparations and lengthy imaging times, or have limited fields of view. Therefore, it is challenging to study soft-tissue microstructure within the macroscopic spatial and temporal context of tissue- and organ-level function. Wide-field imaging techniques provide a non-destructive alternative to rapidly assess tissue microstructure across macroscopic fields of view. Rather than resolving microstructure directly, these techniques are sensitive to light-scattering characteristics of tissue that indicate the underlying microstructure. This dissertation develops light-scattering models to interpret tissue microstructure from light-scattering across macroscopic fields of view rapidly and non-destructively.

The first half of the dissertation uses spatial frequency domain imaging (**SFDI**) to quantify the sub-diffuse light-scattering characteristics of tissues that are intrinsically linked to microstructure. It then introduces a novel empirical model which allows rapid fitting of **SFDI** data and is sensitive to changes in microparticle size. This technique is then

demonstrated as a potential surgical guidance tool for Mohs Micrographic Surgery by rapidly and non-destructively demarcating tumor boundaries in skin biopsies. The imaging and processing speeds achieved with this technique can improve clinical workflows, particularly tissue-conserving surgical procedures, which are currently hindered by the time necessary to determine tumor boundaries using histopathology. Improvements to this technique by use of higher spatial frequencies are also considered.

The second section investigates polarization-dependent scattering in tissues that is a result of collagen fiber microstructure. An experimentally-validated computational model is developed to allow direct conversion of polarized-light measurements into absolute measures of collagen fiber alignment in tissues. Furthermore, a combined polarized light **SFDI** system (**pSFDI**) is demonstrated to measure distinct fiber alignments in multi-layered tissue samples. The increased speed and versatility of this system is employed to map wide-field microfiber kinematics during mechanical tissue deformation. This technique enables direct examination of the contributions of local fiber kinematics to tissue- and organ-level scales of growth and remodeling.

Table of Contents

List of Tables

List of Figures

Chapter 1: Introduction

This chapter will discuss key soft tissue structures and the traditional techniques used to investigate these structures. The improvements to these techniques made possible with biomedical optics are discussed, as well as unmet contemporary needs in quantifying tissue structure. Finally, this chapter introduces the imaging techniques that are the focus of this dissertation, spatial frequency domain imaging and polarized light imaging, and summarizes the ensuing chapters of this work. Several portions of this chapter are excerpts from a previously published review paper (Goth, Lesicko et al. 2016). The author of this dissertation was also the primary author of the review, writing all sections except portions of the introduction and conclusion, with input on structure and content from the co-authors.

1.1 THE IMPORTANCE OF SOFT TISSUE MICROSTRUCTURE

1.1.1 Key soft tissue structures

The term "soft tissue" broadly encompasses many distinct tissue types, including tendons, muscles, and brain matter. Each type of soft tissue varies in terms of constitutive structure and composition, yielding vast distinctions in characteristic forms and functions between types. In this dissertation, the primary structural types are classified into two main groups: cellular structures and extracellular matrix (**ECM**) support structures. Cellular structures are defined by their varieties of cell types and their organization. In particular, the proliferation of cells is a structural indicator which is often used to differentiate healthy tissue regions, inflammation, immune responses, and tumor genesis. This dissertation focuses on cellular aggregation as a structural indicator of physiological and pathological tissue state. Additionally, subcellular components such as the nucleus and mitochondria may be used to identify cellular organization, as these are the binding sites of many histological dyes and also may also have an influence on cellular light transport.

Among the extracellular support structures, collagen and elastin are crucial to the mechanical behavior of soft tissues, excluding muscular tissues and nervous tissues.

Elastin, unsurprisingly, dictates the elasticity of tissue, which allows the tissue to return to its initial state after deformation (Sandberg, Soskel et al. 1981). The concentration and organization of collagen fibers is arguably the most predictive component of soft tissue mechanical function. The arrangement of collagen fibers into rope-like bundles enables the remarkable tensile strength of tendons and ligaments, while transversely isotropic fibers in skin, heart valve leaflets, and the inner and outer cervix wall provide stable macroscale membrane structures. Since type I collagen is the most abundant protein in the body and is the major determinant of dense connective tissue mechanical behavior, this dissertation focuses on quantifying collagen fiber structure in terms of its directional organization to provide a mechanistic understanding of soft tissue response to deformation (Parry 1988, Gelse, Pöschl et al. 2003).

1.1.2 Tissue structure and function relationships

Determining how tissue microstructural constituents function, both individually and organizationally, can provide significant insight into macroscopic tissue- and organ-level function. The health and behavior of the cell populations in soft tissue are directly related to **ECM** properties, and vice-versa. Additionally, microscopic **ECM** and cell behavior both contribute to macroscopic organ-level function, and organ-level factors, such as injury or disease, affect local microstructure. Tissue microstructure is the chief mechanistic link between these disparate scales; it is therefore essential that both the local tissue microstructure and the macroscopic context are considered when examining the physiological state and function of tissues and organs. However, the soft tissue microenvironment is characterized by constant activity; cell growth, cell death, differentiation, propagation, protein production, signaling, and mechanical stimulation constantly occur. Tissue microstructure offers merely a snapshot of the highly dynamic physiological state of tissues and organs. Therefore, a more complete determination of the relationships between tissue microstructures, macroscopic functions, and physiological states can only be achieved when tissue microstructure is studied within the context of tissue- and organ-level spatial and temporal scales.

1.1.3 Applications

Major, immediate benefits result from understanding the relationships between tissue microstructure and tissue- and organ-level function. Tissue microstructure and morphology have long been the gold standard for differential diagnostics for a broad range of diseases and for differentiating between malignant tumors, benign tumors, and healthy tissues. Current diagnostic techniques typically require histological analysis of biopsied tissue. However, real-time knowledge of tissue microstructures would allow surgeries and procedures to be more accurate exercises rather than static protocols, in which the surgeon can assess progress more reliably throughout the process (Vannier and Marsh 1996, Goldberg, Grassi et al. 2005, Xing, Thorndyke et al. 2006). Explicitly defining disease boundaries using microstructures can vastly improve patient outcomes by enabling physicians to ensure that all diseased or damaged tissue is removed or repaired while healthy tissue remains undisturbed.

Computational models of tissues and living tissue systems can off improved patient-specific treatment of diseases. For example, applying unique patient models of valvular dysfunction can allow the use of custom tailored bioprosthetic heart valves which are more effective in treating diseases in the long-term and necessitate fewer invasive surgeries (Aggarwal, Aguilar et al. 2013). However, highly precise inputs in relation to structure, composition, and material properties must be used for these models to accurately simulate real tissue mechanical behavior (Sun and Lal 2002). Some of the most accurate contemporary models of tissue growth and remodeling require accurate knowledge of fiber microstructure throughout the entire tissue (Fung 1990, Sacks 2003). The fiber orientation distribution function is one of the most common microstructural metrics that has been incorporated into biomechanical modeling; this can be expressed either as two- or three-dimensional probability density functions or summary statistics which describe the distribution, such as alignment variance or skew.

Information concerning native tissue structure and material properties is also necessary to produce genuinely biomimetic synthetic tissues that can sustain functionality in highly dynamic biological environments (Courtney, Sacks et al. 2006, Amoroso,

D'Amore et al. 2011). Microstructural heterogeneity across large scales is pivotal to the enduring functional performance of native tissues. However, while engineered tissues have become increasingly complex, most possess relatively homogeneous microstructures relative to native tissues. A mechanistic understanding of the contributions of microstructural heterogeneity to macroscopic function can facilitate the development of synthetic tissues which meet or exceed the performance of native tissues.

1.2 IMAGING TISSUE STRUCTURE

1.2.1 Traditional medical imaging techniques

Non-optical techniques have been commonly adopted as modern medical imaging standards, particularly in the areas of large-scale morphology, tissue differentiation, and biomechanics. These methods are effective primarily due to their relatively large fields of view, intrinsic contrast mechanisms, and broad *in vivo* utility. However, they also face fundamental limitations in terms of accessing important microscopic scales of tissue structure.

Ultrasound, which detects differences in tissue densities, is a form of localized tomography which is non-destructive and easily administered to a broad variety of tissues (Shung and Thieme 1992, Tranquart, Grenier et al. 1999). Although ultrasound can yield images of macroscopic tissue- and organ-level morphology at functional-imaging rates, density differences at the microstructural level of tissue are often too insignificant to obtain meaningful contrast to microstructures.

Magnetic resonance imaging (**MRI**) and other nuclear imaging techniques also have relatively broad fields of view, with scales ranging from organ- to body-level (Lauterbur 1973). Magnetic resonance imaging is particularly appropriate for hemodynamic functional imaging; however, it requires extensive acquisition times for smaller scale, static structural data and has spatial resolution limits of around $0.5 - 1\ mm$ for conventional systems (Haacke, Brown et al. 1999, Prasad 2006). Higher overall resolution is achievable by enhancing the signal-to-noise ratio substantially with stronger

magnetic fields, but this requires instrumentation that is either prohibitively costly or ill-suited for imaging biological tissue (Degen, Poggio et al. 2009). For example, producing a high magnetic field **MRI** to attain a $0.1\,mm$ resolution in conventional MRI format would cost over $\$250$ Million (Vedrine, Aubert et al. 2008).

Conventional X-ray computed tomography (**CT**) is the most capable of obtaining micron-level resolution while maintaining large imaging depths and fields of view (Flannery, Deckman et al. 1987, Hsieh 2009). However, ionizing radiation associated with X-rays limits exposure time before severely damaging biological tissues, which renders it a non-option for extended use (Brenner, Elliston et al. 2001, Brenner and Elliston 2004, Smith-Bindman, Lipson et al. 2009).

1.2.2 Histological techniques

Light-based microscopy has historically been among the most powerful tools for understanding biological organisms (Hodgkin and Lister 1827, Bloom, Fawcett et al. 1962). The most significant advantage of light microscopy is that the images it produces can be broadly interpreted by researchers with disparate backgrounds, although specialized training is necessary for precise clinical interpretation. Light microscopy also enjoys a nearly unmatched versatility in its application; it can function as both a simple low-level magnifier and as a probe of cellular and sub-cellular scales. Bright-field microscopy is the simplest form of light microscopy and one with which most people are familiar (Keller and Goldman 2006); it involves a thin sample being placed on a slide between an illumination source and an objective lens which relays the transmitted image to the viewing ports. Contrast is created primarily by the absorption of light as it passes through the sample, which produces a 'shadow' of the sample structure.

Bright-field microscopy relies entirely upon intrinsic absorption, which often results in low contrast in most prepared thin samples. Histological stains, or dyes which bind to specific tissue or cellular and **ECM** components, are often necessary to achieve suitable contrast in bright-field microscopy. To apply wide-field light microscopy to untreated tissues, other methods of endogenous contrast enhancement have been

investigated. Phase contrast, differential interference contrast (**DIC**), and dark field microscopy all utilize different sources of endogenous tissue contrast in order to produce greater detail in terms of untreated tissue structure. These techniques can be particularly effective when each is combined onto a single microscope stage so that the sample can be imaged using different modalities.

The primary limitation of using traditional light-based microscopy techniques to examine tissue microstructure is these techniques destructiveness; samples must be fixed and thinly sectioned, and the resulting microstructure may be altered by the preparations such that it is no longer representative of functional, *in vivo* tissue. Additionally, the tissue is unusable for continued study after imaging, meaning that dynamic tissue changes such as fiber kinematics are essentially impossible to determine except at experimental endpoints.

1.2.3 Advanced optical techniques

Laser-scanning is nearly ubiquitous among advanced optical microscopy techniques. Typically, a laser source is focused to a well-defined spot, the size of which determines the resolution. The reflected light is then detected, generally through the same objective optics. Advanced theories concerning the interactions between light and tissue allow powerful measurement and imaging of tissues, and resolutions achieved with these techniques have approached theoretical diffraction limitations (Balas 2009). Light within the visible and infrared spectrum is non-ionizing and can generally be employed in a non-destructive manner in thick tissues without the need for physical section, which enables tissue microstructure to be analyzed *in vivo* or at least in an *in situ* functional setting. Additionally, these optical techniques are capable of a broad range of scales, resolutions, and sources of both endogenous and exogenous contrast, which render them highly versatile for a vast array of applications. Importantly, advanced optical techniques offer degrees of freedom beyond spatial variation of intensity with which to perform quantitative measurements. Polarization-, wavelength-, and frequency-dependent measurements can enable the quantification of a greater variety of tissue metrics, including molecular

composition, fiber alignment, cellular structure, and mechanical properties. Importantly, advanced optical techniques often provide sensitivity to tissue microstructures without necessitating the resolution of the microstructures themselves. These factors make advanced optical techniques ideal for analyzing the microstructure of tissues. However, tradeoffs often characterize many of these techniques, particularly in terms of the extensive imaging times typically required to achieve high sensitivity and resolution at tissue- and organ-level scales; this imposes practical limits on the assessment of functional tissue microstructure within a macroscopic context.

1.2.3.1 Confocal Microscopy

Laser-scanning confocal microscopy uses intrinsic contrast to resolve microstructures with varying refractive indices, and has also demonstrated that specific biological molecules such as melanin provide particularly high contrast (Minsky 1961, Wilson 1990). Fluorescent dyes can also be used as markers to highlight specific areas of tissues and cells, and multiple fluorescent channels can be imaged simultaneously while maintaining exact registration (Brakenhoff, Voort et al. 1989, Murray 2005). This powerful technique is responsible for producing striking images of tissue and cell structure. The confocal principle is a method that entails filtering out any light aside from that reflected from the focal plane; this avoids a major problem in traditional light microscopy when investigating thick samples ($> 50\ \mu m$) with low endogenous contrast from absorption (Dunn, Smithpeter et al. 1996). Consequently, the axial and lateral resolutions of the system are entirely dependent upon its optical components, primarily the numerical aperture and confocal pinhole size of the system. Confocal microscopy has become particularly relevant in the advent of modern lasers, which can be focused significantly more precisely than incoherent light sources. Practical limits have increasingly approached the theoretical diffraction limits of sub-micron resolution in both axial and lateral dimensions. Commercially available objectives with a numerical aperture of at least 0.9 can expect to achieve axial and lateral resolution of approximately $0.5 - 5\ \mu m$ in practice (Pawley 2010).

The primary limitations of confocal laser-scanning microscopy techniques are related to the method of spatial filtering. Spatial filtering requires point-scanning, which results in substantially longer acquisition times, such that video-rate imaging ($> 20\ Hz$) is achievable, but only for limited spatial dimensions (Rajadhyaksha, Anderson et al. 1999). Typically, microstructural resolution must be sacrificed to permit sampling of larger fields of view ($> 1\ cm^2$). Line scanning and raster scanning techniques can achieve faster imaging speeds, although this also compromises the resolution and imaging field (Murray 2005). Additionally, the spatial filtering which eliminates out-of-focus light also rejects light that has been multiply scattered *en route* to and from the sample. This means that the depth penetration of confocal reflectance microscopy operating near ideal confocal performance is limited to about 3 to 4 transport lengths (**Chapter 2**) for an adequate signal-to-noise ratio (Smithpeter, Dunn et al. 1998). The transport length depends upon many factors, including the tissue optical properties and laser wavelength; for reference, confocal microscopy is generally limited to under $300\ \mu m$ in human skin tissue (Nehal, Gareau et al. 2008).

1.2.3.2 Non-linear Microscopy

Non-linear laser-scanning microscopy techniques, namely two photon and second harmonic generation (**SHG**), offer several advantages when compared to reflectance and fluorescence confocal techniques. In traditional fluorescence, a single incident photon results in the emission of a similar energy photon in fluorophores. In multi-photon fluorescence, two (or more) incident photons on a single molecule results in the emission of a photon with higher energy, which results in a higher frequency and a lower wavelength (Göppert-Mayer 1931, Kaiser and Garrett 1961). Because this phenomena only occurs when the photons arrive nearly simultaneously at the molecule, it confines the effect to the focal volume of the system, which results in submicron resolution imaging capabilities (Budnev, Ginzburg et al. 1975). **SHG** achieves essentially the same effect through a slightly different physical mechanism (Prasad and Williams 1991).

Non-linear laser-scanning microscopy techniques provide several advantages in relation to confocal and fluorescence microscopy (Denk, Strickler et al. 1990, Denk and Svoboda 1997). Longer excitation wavelengths in the red and near infrared allows significantly deeper penetration (up to $1\,mm$) while the maintaining the sub-micron resolution (So, Dong et al. 2000, Helmchen and Denk 2005). Additionally, multi-photon systems require substantially less illumination power, since no pinhole is necessary for optical sectioning, which results in less light being wasted through filtering, less photo-bleaching in final images, and less photo-damage to the sample (Patterson and Piston 2000). Emission wavelengths can be easily distinguished from the excitation wavelength, which results in a drastic improvement in terms of contrast when introduced as an imaging method (Denk, Piston et al. 1995). Most importantly, two-photon and **SHG** can measure intrinsic contrast differences from native tissue structures. Many structurally-relevant molecules, including collagen and elastin, can be specifically identified using two-photon excitation or second harmonic generation (Zipfel, Williams et al. 2003). Contrast enhancement and specific labeling of other tissue regions and constituents can also be achieved by using fluorophores similar to those used in confocal fluorescence imaging (Dickinson, Bearman et al. 2001, Rubart 2004).

Despite their superior performance, non-linear laser-scanning microscopy techniques for examining tissue microstructures possess notable limitations. Excitation wavelengths in the near IR have inherently larger diffraction-limited resolutions; however, this loss in resolution is primarily an issue in sub-cellular imaging, and the technique remains capable of resolving most of the fine details of tissue microstructure. While achieving a $1\,mm$ sampling depth is generally considerable in optical imaging, it typically requires physical staining of the sample with specific dyes or nanoparticles and often precipitates tissue damage due to the high fluence rates necessary. Finally, high-speed scanning with reduced lateral resolution can allow video-rate acquisition for small 2D planes, but not for substantial fields of view relative to tissue- and organ-level scales (Kim, Buehler et al. 1999). For example, a single plane, $0.25\,mm^2$ image with a pixel size of $8\,\mu m$ requires a 20-minute scan on contemporary two-photon imaging systems.

Additionally, the limited axial sectioning depth ($\sim 5 - 50\ \mu m$) often requires imaging multiple planes if the sample is not substantially flat.

1.2.3.3 Spectroscopic Techniques

Spectroscopic microscopy techniques use wavelength-dependent reflectance and fluorescence to quantify the structure and composition of tissues at cellular and molecular scales. Diffuse reflectance spectroscopy (**DRS**) uses light transport theory in heterogeneous tissue to characterize the bulk scattering and absorption of different regions. The signal has a distinct signature of diffuse reflectance from the tissue across a broad spectrum of wavelength. This can be used to identify specific scattering and absorption properties of the sample, and subsequently attributed to different tissue constituents (Farrell, Patterson et al. 1992, Doornbos, Lang et al. 1999). Similarly, laser-induced fluorescence spectroscopy (**LIFS**) uses a fluorescence spectrum to differentiate between tissue regions; this is similar to confocal fluorescence, but wavelength-dependence is considered across a larger, more highly resolved spectrum (Kinsey 1977, Cothren, Richards-Kortum et al. 1990).

Raman scattering spectroscopy investigates non-elastic scattering in tissue which occurs when scattered light interacts with high-frequency vibrations within the individual molecules and results in an increased or decreased wavelength, respectively (Long and Long 1977). The signal is several orders of magnitude weaker than in **DRS** or **LIFS**, but individual molecules illicit highly specific Raman scattering spectra, which can allow more reliable identification of tissue constituents. Additionally, the signal can be significantly enhanced by utilizing surface enhancement techniques of specific nanoparticles (Nie and Emory 1997, Movasaghi, Rehman et al. 2007).

The information obtained through these spectroscopic techniques using fiber probes reflects bulk local tissue characteristics rather than being confined to a focal volume. This results in generally larger lateral resolutions, which are typically defined by source-detector separation in the probes (approximately 100 to 1000 μm). Additionally, the signal is integrated along the entire axial dimension sampled, which means that the

axial resolution is an average measurement of reflectance or fluorescence across this sampling depth. Probe design can influence the depths at which the tissue is sampled; however, this cannot result in true optical sectioning to a specific plane, but only averaged depth sectioning.

Incorporating these techniques into confocal configurations can increase sampling resolution and sectioning capability but is also limited by scanning considerations for tissue- and organ-level fields-of-view. Each of these spectroscopic modalities may be adapted into laser-scanning microscopy systems to provide additional quantification of both cellular and molecular structure and composition; however, the techniques are then limited by the conflict between resolution, scale, and acquisition rate.

1.2.3.4 Optical Coherence Tomography

Optical coherence tomography (**OCT**) originated in the early $1990s$ and has rapidly been adapted for clinical use and commercial systems (Huang, Swanson et al. 1991). Optical coherence tomography is analogous to ultrasound, although it uses light rather than sound as its probing mechanism. It uses low coherence interferometry to identify regions of high back-scattering, which indicates interfaces within the sample. Axial resolution of **OCT** mostly relies upon the bandwidth of the laser and is normally around 10 to 15 μm (Brezinski 2006). There is a tradeoff between the lateral resolution and the axial field of view over which **OCT** can resolve an image; higher lateral resolution limits the depth of focus, while higher depths of focus are only achievable by compromising lateral resolution (71). Imaging depth is also limited by light attenuation, although most near-infrared wavelengths used are capable of low attenuation. Optical coherence tomography has been demonstrated to achieve a 6 mm axial field of view while maintaining a 10 μm lateral resolution (Ding, Ren et al. 2002). Lateral field of view is invariably only limited by the scanning instrumentation used.

Newer implementations of **OCT**, namely Fourier domain **OCT**, have allowed much higher axial scanning speed; video-rate ($> 30Hz$) $3D$ scans with relatively large fields of view have been accomplished with the advent of broadband and tunable laser

sources (Tearney, Brezinski et al. 1997). This has significantly impacted the incorporation of **OCT** systems into clinical environments, as it provides rapid volumetric imaging capability. In addition, newer lasers have allowed micro-**OCT** (**μOCT**), which is a technique that has been employed to improve axial resolution to $< 1\mu m$ and lateral resolution to $< 2\mu m$ (Drexler, Morgner et al. 1999, Liu, Gardecki et al. 2011). Optical coherence tomography can also be employed using fiber-optics, which allows imaging probes to navigate biological lumina of around $3\ mm$ in diameter (Tearney, Brezinski et al. 1996). The largest clinical application for **OCT** is in ophthalmology, in which retinal morphology can be easily accessed through the optically clear cornea evaluate for degenerative diseases. It is also employed conveniently as an endoscopic tool, particularly in intraluminal imaging, for which **OCT** probe geometry is particularly well-suited.

Overall, **OCT** is a robust, highly adaptable method for imaging tissue morphology. Its primary limitation is the shadowing effect, which can obscure deeper tissue regions and decrease contrast, although it is nevertheless suitable for many of the imaging tasks in which it is employed, where features near the surface of the tissue are important. It is useful in turbid, highly scattering tissues, and is capable of substantially higher penetration than confocal or non-linear techniques. It benefits from adequate resolution in both axial and lateral directions to resolve larger cellular structures and high speed acquisition capability for functional and intraoperative imaging; it can also image significantly deeper into turbid media while maintaining adequate resolution more effectively than most other optical imaging techniques. However, while recent studies in angularly resolved and polarization sensitive **OCT** have provided increased microstructural sensitivity, direct relationships between absolute microstructural measurements and **OCT** signals require further development to be used in a clinical environment.

1.2.3.5 Small Angle Light Scattering

Small angle laser light scattering (**SALS**) is a technique which was originally applied to study and characterize polymer chains suspended in solution by analyzing the behavior of light scattered from the medium. More recently, the technique has been adopted

as a means of seamlessly acquiring sample-wide soft tissue microstructure information (Sacks, Smith et al. 1997). Small angle laser light scattering techniques for collecting structural properties work by exposing samples to a non-polarized beam of low power ($\sim 5mW$) laser light. Light passing through the tissue is either transmitted or scattered, such that the spatial distribution of scattered light (**SALS** pattern) represents the sum of all structural information within the light beam envelope (Sacks, Smith et al. 1997). Photons scattered by tissue microstructural elements are characterized by two values, including scattering angle and azimuthal angle. The scattering angle is measured from the direction of the incident beam and is determined by the physical characteristics of the scattering structure, while the azimuthal angle is perpendicular to the orientation of the structure in the plane of the tissue sample, according to theories of cylindrical diffraction and scattering. The **SALS** pattern is the collection of diffracted and scattered photons by a photosensor or projection screen; highly aligned structures produce high eccentricity elliptical patterns and randomly distributed fibers yield circular patterns. From this pattern, the angular distribution of microstructure fibers can be directly obtained.

By raster scanning the sample through the path of the laser beam, microstructure maps with a large field-of-view can be created that denote fiber properties, including mean fiber direction, index of fiber alignment, and mean fiber diameter. The lateral spatial resolution of these maps is determined by the raster step size and the diameter of the laser beam. The **SALS** technique is capable of resolving properties from collections of fibers with diameters around the size of the illumination wavelength (~0.5 – 20 μm).

Notably, unlike some imaging modalities, **SALS** is unable to resolve structures axially through the sample; **SALS** point-scans yield structural information that is inherently an average of individual fiber properties across the area of the incident beam and through the depth of the sample. Additionally, because of the transmission-based nature of **SALS**, the technique requires translucent samples: If the sample is not sufficiently translucent, chemical clearing is required. In the case of multi-layered samples, the layer-specific microstructure will be averaged in the transmission measurement without further physical sectioning of the individual layers.

Small angle light scattering is most appropriate when tissue-wide microstructure is required and damage to the sample is a non-issue; it can be used for soft tissues following mechanical testing or fixation under load to examine microstructure-derived mechanical properties or in the characterization of healthy and diseased tissue. In constitutive model development, **SALS** has proven to be an effective experimental complement to mechanical testing of soft tissues with the direct inclusion of these microstructure maps (Sacks 2003). However, the need for optically clear samples, slow imaging speeds and insensitivity to layered structures are major limitations.

1.2.4 Current needs in tissue structure assessment

It is crucial for tissue imaging systems to be able to resolve or otherwise detect the smallest tissue features that relate to function. Depending upon the specific tissue or feature of interest, the absolute sizes of structures are often variable. For the purposes of this dissertation, features of interest will primarily include cells and collagen fibers, which range between about $10\ nm$ to $100\ \mu m$ in size. However, as long as microstructures can be detected reliably, explicitly resolving the microstructures through magnification or other means may not be necessary.

Many imaging techniques require physical sectioning of the tissue, which is undesirable for several reasons. Hydration, loading, and temperature are merely several of the dynamic changes that can impact the analysis of excised tissues, which may result in misleading and incorrect conclusions. Techniques which physically, chemically, or otherwise alter the normative physiological state of tissue during preparation or measurement are deemed destructive. Additionally, destructive techniques are often limited to experimental endpoints; therefore, the functional behavior of tissue microstructure over time cannot be observed. This dissertation emphasizes the need for samples to remain relatively undisturbed during imaging and minimize interaction with the tissue or its microstructure as a result of measurements. While the ultimate objective of non-destructive techniques may be *in vivo* imaging applications, immediate goals involve

permitting the study of tissue structure in its undisturbed or functional *in vitro* or *in situ* state.

Similarly, the rapid acquisition times of structural data are notable when investigating tissue function. In many imaging systems, resolution and field of view are inherently coupled with image acquisition time. Because most ultra-high-resolution imaging systems rely upon scanning a single point at a time, large fields of view require longer acquisition times. This is a major consideration for functional and intraoperative imaging: If high temporal resolution is paramount, then spatial resolution or field of view must be limited to compensate. Many optical imaging techniques are currently limited in their utility by their abilities to physically scan samples at tissue- and organ-level fields-of-view.

In the clinical environment, medical imaging typically serves as a guidance tool rather than as a diagnostic tool. Transformative clinical imaging systems integrate the ability of optical techniques to non-invasively probe soft tissue structure with the ability to quickly aid in determining accurate diagnostic or surgical decisions. Medical applications of optical techniques include rapid disease screening, patient-specific therapies, and real-time image-guided surgery. To achieve clinical relevance, imaging technologies must resolve or otherwise characterize *in vivo* or *in situ* tissue microstructure at large scales without compromising speed or becoming destructive. The low fields-of-view and slow acquisition times of ultra-high-resolution optical techniques limit their appropriateness in many clinical settings.

Systems that can detect signals which are indicative of tissue structure, though not explicitly resolving the structures themselves, may ameliorate the conflict between microstructural sensitivity, macroscopic scale, and temporal constraints. This dissertation introduces two wide-field reflectance imaging modalities, spatial frequency domain imaging and polarized light imaging, to rapidly measure tissue microstructures across meaningful spatial and temporal scales. For both techniques, this dissertation presents models which describe how light is scattered by certain microstructural features, including cells and fibers.

Spatial frequency domain imaging has been demonstrated to be highly sensitive to cellular microstructure which is representative of the physiological state of the tissue. Similarly, polarized light imaging is sensitive to the orientation distribution of collagen fibers. Sensitivity to multi-layered structures is demonstrated with a combined polarized light and spatial frequency domain imaging system, and is extended to study fiber kinematics as well as 3D fiber structure. Both techniques aim to improve current methods for studying and assessing tissue function and pathology by providing more rapid, wide-field sensitivity to tissue microstructures.

1.3 CHAPTER SUMMARIES

Chapter 2 discusses the foundation of light transport theory, which bridges diffuse scattering theory and ballistic scattering events. It first outlines the relationship between bulk optical properties of tissue and individual tissue components and then introduces spatial frequency domain imaging (**SFDI**). Finally, it describes a novel, rapid processing model for sub-diffuse (**sd**)**-SFDI** measurements that demonstrates microstructural sensitivity, and a validation experiment demonstrates the empirical model performance.

Chapter 3 discusses the use of the **sd-SFDI** model in a clinical setting, specifically as a surgical guidance tool for rapidly assessing tumor boundaries during Mohs micrographic surgeries to resect skin cancer tumors. Nodular basal cell carcinoma samples are imaged, and extracted optical model parameters are related to specific features in the tissue that correlate with those identified through expert histopathology. Finally, **Chapter 3** demonstrates a proof-of-concept experiment highlighting the discriminatory power of these optical model parameters to guide tumor boundary assessment.

Chapter 4 discusses polarized light-scattering from cylindrical particles, which are used to model collagen fibers. It then introduces a model which allows calculation of absolute structural anisotropy of fibers from their relative optical anisotropy measured with polarized spatial frequency domain imaging (**pSFDI**). Electrospun fibers are used to validate of the model, and a simulation of a large range of physiologically relevant fiber

parameters are used to establish a relationship between fiber orientation distributions based on their resultant polarization-dependent reflectance.

Chapter 5 addresses applications of polarized light imaging to native, bioprosthetic, and synthetic heart valve materials. First, it demonstrates that **pSFDI** can provide comparable fiber alignment information to an existing gold standard, **SALS**, at significantly higher speeds and with additional volumetric sampling control that allows measurement of specific fiber layers in native heart valve leaflets. Second, the improved speed of **pSFDI** is used to demonstrate pseudo-dynamic imaging of collagen fiber in bioprosthetic valve materials at multiple time points during biaxial mechanical deformation.

Chapter 6 summarizes the major contributions of this dissertation. It also addresses limitations and forecasts directions of future work.

Chapter 2: Modeling and measuring sub-diffuse light scattering from tissue microstructure

This chapter defines the theoretical expressions used to model light-scattering from spherical particles the size of cells and nuclei. First, it quantifies bulk scattering and absorption properties under the assumption of diffuse light propagation, which accounts for the average of many light-particle interactions. Second, Mie theory is applied to calculate the result of ballistic (single particle) scattering and absorption events. It then introduces spatial frequency domain imaging (**SFDI**), which is a technique used to measure optical properties of tissues across wide fields-of-view and explores how it can be used to investigate tissue structures at macroscopic scales. It introduces a novel empirical model which permits rapid processing of **SFDI** data and is sensitive to changes in the size of tissue microstructures; it also describes **SFDI** instrumentation and data collection extensively. Finally, it outlines the fabrication of tissue-mimicking phantoms with pre-determined optical properties and uses these phantoms to validate the conclusions about microstructure size from this dissertation's system measurements and models.

2.1 Light Diffusion In Turbid Media

This section's contents are based on established light transport theory. Though it refers to individual photon interactions for specific examples, the theories discussed assume "light" to be a collection of photons within the visible electromagnetic spectrum. Additionally, it only considers non-polarized light transport under a steady state and elastic scattering conditions from spherical scatterers. Unless otherwise indicated, the majority of the equation forms were adapted from the following sources: (Tuchin 2007, Wang and Wu 2012, Boas, Pitris et al. 2016).

2.1.1 Diffuse Optical Properties

As light propagates through biological tissues, it encounters various tissue components that cause it to be optically "turbid" (scattering and absorbing light). Tissue

structures which scatter light include cells, nuclei, and structural fibers, while the primary chromophores that absorb light within the visible spectrum include hemoglobin, melanin, lipids, and water (Jacques 2013). Scattering events occur when the direction of light propagation changes upon encountering a discontinuity in the refractive index. Absorption events are interactions that result in a decrease in the total energy of incident light, such as when the energy level of re-emitted photons changes (fluorescence). In terms of the scattering and absorption of tissue, it is useful to consider the mean-free-path (***MFP***) of photon propagation, which describes the average distance over which light propagates before a scattering or absorption event occurs. For example, when light propagates through a volume containing some scattering or absorbing elements, as in **Figure 2.1**., each of the three volumes has a different average ***MFP*** (grey) of the three available path-lengths (blue) for light traveling through the sample.

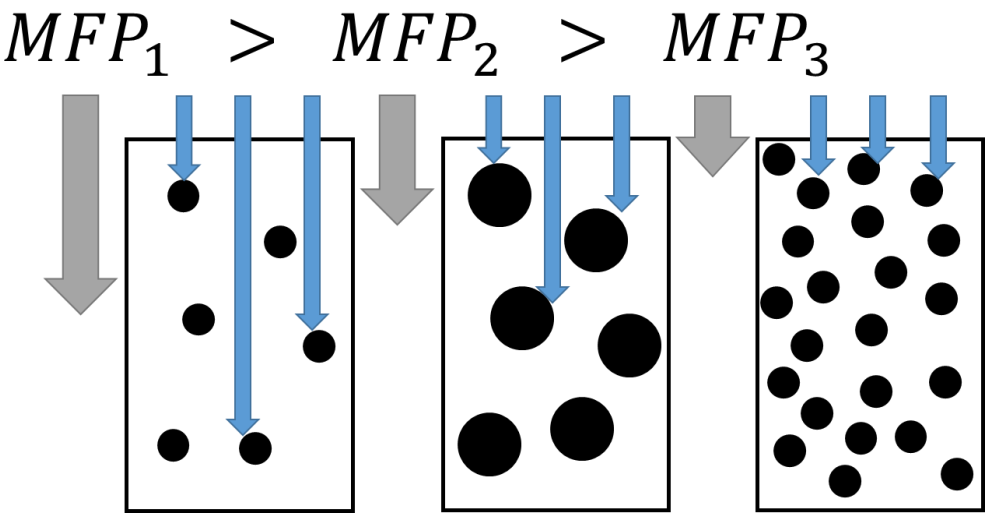

Figure 2.1: Examples of changes in mean free path (***MFP***) as a function of particle size and density.

Distinct ***MFP***s exist for absorption ($\boldsymbol{MFP_{abs}}$) and scattering ($\boldsymbol{MFP_{sca}}$) events in tissues. It is useful to quantify scattering and absorption by the inverse of their ***MFP***s and to describe the frequency of scattering or absorption events per unit length in mm^{-1} or

cm^{-1}. Therefore, the scattering coefficient $\boldsymbol{\mu_s}$ and absorption coefficient $\boldsymbol{\mu_a}$ can be defined as follows:

$$\mu_s = \frac{1}{MFP_{sca}} \tag{2.1}$$

$$\mu_a = \frac{1}{MFP_{abs}} \tag{2.2}$$

Additionally, the extinction coefficient $\boldsymbol{\mu_t}$ is the frequency of either a scattering or absorption event occurring per unit distance:

$$\mu_t = \mu_s + \mu_a \tag{2.3}$$

The inverse of $\boldsymbol{\mu_t}$ is the total $\boldsymbol{MFP}$ of light transport in turbid media, which is the average distance traveled between scattering or absorption events. **Figure 2.1** illustrates that $\boldsymbol{MFP}$s are primarily dependent upon two factors, including the size of the scattering or absorbing elements and the number of elements per unit volume. Therefore, the scattering and absorption coefficients can also be defined based on these factors:

$$\mu_s = N_s \sigma_{sca} \tag{2.4}$$

$$\mu_a = N_a \sigma_{abs} \tag{2.5}$$

Above, $\boldsymbol{N_s}$ and $\boldsymbol{N_s}$ indicate the density of the scatterers or absorbers per unit volume in $\#/cm^3$; $\boldsymbol{\sigma_{sca}}$ and $\boldsymbol{\sigma_{sca}}$ indicate the scattering or absorption cross-sections in cm^2. However, there are many cases when the scattering or absorption cross-section is not equal to the geometric cross-section of the particle. The scattering and absorption cross-sections are therefore products of the geometrical cross-section of the particle and the scattering or absorption efficiency of the particle:

$$\sigma_{sca} = \sigma_g Q_{sca} \quad \textbf{(2.6)}$$

$$\sigma_{abs} = \sigma_g Q_{abs} \quad \textbf{(2.7)}$$

Above, $\boldsymbol{\sigma_g}$ is the geometrical cross-section of the individual particles, which is often assumed to be spherical and is therefore equal to the circular profile created by a sphere ($\boldsymbol{\sigma_g = \pi r^2}$). $\boldsymbol{Q_{sca}}$ and $\boldsymbol{Q_{abs}}$ indicate the total scattering and absorption efficiencies of the particles. These efficiencies depend upon numerous factors, including the dielectric properties of the particle, the geometry of the particle, and the size of the particle relative to the wavelength of the incident light. For individual interactions with single particles, these efficiencies can be calculated by solving approximate models of light transport or numerically by using the Mie solution, the latter of which **Chapter 2.2** delineates. For real tissues, however, there are not singular types of scattering or absorbing particles: Many diverse tissue structures and chromophores contribute to light propagation. Therefore, the bulk tissue scattering and absorption are a sum of the scattering and absorption contributions from all of the individual particles for a sampled volume:

$$\mu_s^{tissue} = \sum \mu_s^{particles} \quad \textbf{(2.8)}$$

$$\mu_a^{tissue} = \sum \mu_a^{particles} \quad \textbf{(2.9)}$$

2.1.2 The Radiative Transport Equation (RTE)

The Boltzmann radiative transport equation (**RTE**) is an energy balance equation which can be applied to describe light transport in turbid media for differential volume, solid angle, and time (Case and Zweifel 1967). Light propagation in this equation is

quantified by radiance, $\boldsymbol{L}(\hat{\boldsymbol{r}}, \hat{\boldsymbol{s}}, \boldsymbol{t})$, which corresponds with units of watts per square meter per steradian [$W \cdot m^{-2} \cdot sr^{-1}$] and depends upon six variables, including three for position, which are described in vector coordinates as $\hat{\boldsymbol{r}}(\boldsymbol{x}, \boldsymbol{y}, \boldsymbol{z})$, two for direction, which are described in polar and azimuthal angles as $\hat{\boldsymbol{s}}(\boldsymbol{\theta}, \boldsymbol{\varphi})$, and one for time, $\boldsymbol{t}$. The full **RTE** is as follows:

$$\frac{n}{c}\frac{\partial L(\hat{r}, \hat{s}, t)}{\partial t} + \nabla \cdot L(\hat{r}, \hat{s}, t)\hat{s} = \tag{2.10}$$

$$-\mu_t L(\hat{r}, \hat{s}, t) + \mu_s \int_0^{4\pi} L(\hat{r}, \hat{s}', t) p(\hat{s} \cdot \hat{s}') d\Omega' + Q(\hat{r}, \hat{s}, t)$$

The first term in the **RTE** is the change in radiance over time, normalized to the speed of light in the tissue, $\boldsymbol{n/c}$. This dissertation ignores this term and only considers steady-state light diffusion using continuous-wave sources. The second term is the gradient of radiance in direction $\hat{\boldsymbol{s}}$, which accounts for non-scattering or absorption losses of light due to divergence. The third term is the radiance extinguished by either absorption within the differential element or the scattering out of the differential element; it is scaled by the bulk extinction coefficient $\boldsymbol{\mu_t}$. The fourth term is the differential scattering cross-section, which describes directional light-scattering amplitude at all angles from the differential element. This term is scaled by the bulk scattering coefficient $\boldsymbol{\mu_s}$ and contains the vector representation of scattering phase function $\boldsymbol{p}(\hat{\boldsymbol{s}} \cdot \hat{\boldsymbol{s}}')$ (see **Chapter 2.2**). The fifth and final term accounts for sources of radiant energy injected into the differential element, such as that from a lamp, LED, or laser.

2.1.3 The Diffusion Approximation

The **RTE** has no readily tractable closed-form solution and is therefore solved numerically or approximately. Finite-difference and Monte Carlo numerical methods are highly accurate in calculating exact light transport for a large range of bulk optical properties but are often too computationally exhaustive for simulating samples with high

spatial heterogeneity of scattering and absorption (Carp, Prahl et al. 2004, Boas, Pitris et al. 2016). Instead, approximations to the **RTE** can be made, such that the resulting differential equation has a tractable closed-form solution (Ishimaru 1989, Farrell, Patterson et al. 1992, Star 1995). This dissertation's modeling of light propagation in tissues will henceforth be conducted under the following assumptions:

1. Scattering-dominated transport (scattering occurs significantly more often than absorption);
2. Isotropic scattering (scattering is relatively equal in all directions).

Light transport which satisfies these conditions is deemed within the diffusion regime, which is generally appropriate for describing light propagation in biological tissues. Tissues have high amounts of elastic scattering relative to absorption events, which satisfies assumption 1. However, assumption 2 of isotropic scattering does not apply to tissue, which has highly anisotropic, forward-directed scattering. The **P1** approximation regards the scattering anisotropy $\boldsymbol{g}$ as the first moment of the scattering phase function. It is calculated as the average cosine of the resultant scattering angle from the initial direction of propagation (discussed further in **Chapter 2.2**). Biological tissues have a scattering anisotropy of: $\boldsymbol{g} \approx 0.9$. Fortunately, the scattering coefficient can be modified to a reduced form to account for anisotropic scattering within the diffusion approximation:

$$\mu_s{}' = (1 - g)\mu_s \tag{2.11}$$

In the equation above, $\boldsymbol{\mu_s'}$ is the reduced scattering coefficient. The modified transport coefficient becomes the following:

$$\mu_{tr} = \mu_s' + \mu_a \tag{2.12}$$

It is useful to understand the implications of accounting for anisotropy in the reduced scattering coefficient by considering the number of scattering interactions per unit of length. As $\boldsymbol{g}$ increases, $\boldsymbol{\mu_s'}$ increases, which indicates that the number of scattering events

for a given unit length is higher in the case of anisotropic scattering media. When $\boldsymbol{g} = 0$, diffuse light propagation tends to adhere to a more indirect (diffuse) path. In other words, $\boldsymbol{g}$ acts as a proportionality factor to ensure that anisotropic scattering can be represented in terms of isotropic diffusion. Under these conditions, the simplified steady-state diffusion approximation form of the **RTE** can now be established:

$$\nabla^2\Phi - \mu_{eff}^2\Phi = -3\mu_{tr}I \qquad \textbf{(2.13)}$$

In this equation, $\boldsymbol{\Phi}$ is the fluence rate, $\boldsymbol{I}$ is a source, and $\boldsymbol{\mu_{eff}}$ is the effective transport coefficient:

$$\mu_{eff} = \sqrt{3\mu_a\mu_{tr}} \qquad \textbf{(2.14)}$$

2.1.4 Considerations of the Diffusion Regime

Defining light propagation by the diffusion approximation in **EQ 2.13** facilitates the measurement of the optical properties of tissue. Firstly, this form allows for any spatially varying source $\boldsymbol{I}$ to be analyzed by convolving a differential point source of light with the beam profile of any physical source. Similarly, measurements of real fluence can also be calculated by summing differential fluence over any area described by a detection geometry that is an arbitrary distance from the source. Describing light transport in fluence rates $[W/cm^2]$ is also useful because this is the irradiation that is typically measured for light source and detectors. Subsequently, the bulk optical coefficients of tissue can be measured with high accuracy using these techniques (Farrell, Patterson et al. 1992, Kienle, Lilge et al. 1996, Doornbos, Lang et al. 1999, O'Sullivan, Cerussi et al. 2012).

However, some limitations are inherent to the diffusion approximation. First, for the reduced scattering coefficient to properly correct for anisotropic light scattering, measurements of light propagation must be performed after light has undergone numerous

scattering events sufficient to become diffuse, such that the initial direction of incidence is lost. The diffusion coefficient indicates that the minimum physical distance light must travel from a source before it can be considered appropriately diffuse and behave in terms of the diffusion approximation. In tissues, which are scattering-dominant and have a typical bulk-reduced scattering coefficient of approximately $\mu_s' \sim 1\ mm^{-1}$, the diffusion length is about $1/3\ mm$. In other words, only light that is sampled outside of this distance can be reliably described as diffuse and adheres to the predictions of the **RTE**. For light sampled at distances shorter than the diffusion length from the source, corrections for higher orders of the phase function must be applied (Bevilacqua and Depeursinge 1999, Hull and Foster 2001).

2.2 Mie Solutions to Ballistic Scattering from Spherical Particles

Gustav Mie originally developed "Mie theory" in the early 1900s to explain wavelength-dependent scattering and absorption from gold nanoparticles of varying sizes (Mie 1908). The observation of distinct colors in these particle solutions, despite their identical molecular composition, suggested that the geometry of particles is pivotal in the wavelength-dependent scattering and absorption of light. Mie theory describes the solution to Maxwell's equations of light incident onto a single particle with known geometry, size, and refractive index. It should be noted that the present discussion of the Mie solutions only considers elastic scattering, wherein the total number of photons (power) may change after partial absorption by the particle; however, the energy (and therefore wavelength) of the individual photons of scattered light is maintained; fluorescence events, in which photons of a new energy (wavelength) are emitted, have been ignored here. Although several other analytical approximations of light scattering from particles exist, these approximations are valid exclusively under specific conditions, such as when the size of the particle is significantly greater or less than the wavelength of incident light. Conversely, the Mie solution is valid across any combination of particle size and wavelength, including cases when the size of the particle is comparable to the wavelength of incident light, and can also be derived for numerous particle geometries. This is particularly relevant in

biomedical optics, in which tissue microstructures of interest, including cells, nuclei, and fibers, span a large size range (10 nm to 100 μm), which overlaps with the wavelengths of visible light (400 to 700 μm). Due to its versatility, Mie scattering has significantly impacted a wide range of fields, including astronomy, biomedical optics, and atmospheric sciences.

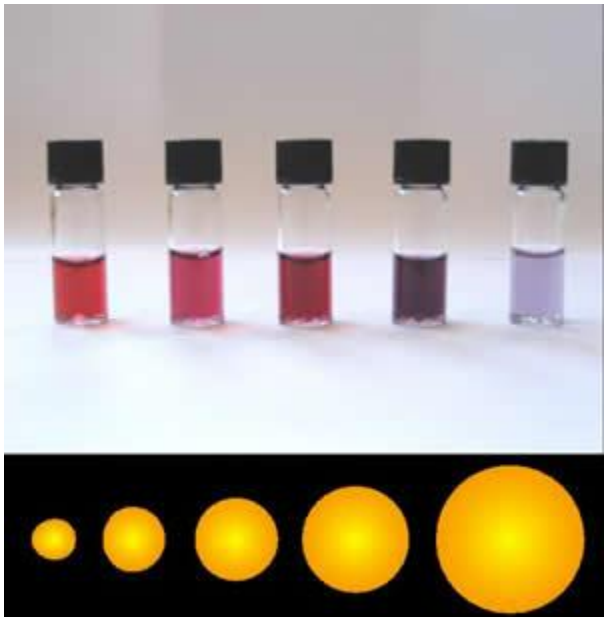

Figure 2.2: Solutions of gold nanoparticles with increasing sizes; changes in color demonstrate that scattering and absorption of light depend upon particle size (Kondinski 2010).

In the simplest form, the Mie solution to Maxwell's equations for planar electromagnetic wave propagation is derived by enforcing a geometric surface as the boundary condition. The Mie solution offers a complete mathematical description of the resulting electromagnetic wave propagation after interaction with the particle. Subsequently, the solution can be used to calculate the scattering efficiency of a particle of any size and the scattering phase function for the particle (Hulst and Van De Hulst 1957, Bohren and Huffman 2008). The scattering phase function describes the far-field amplitude

of light scattered in every direction from the particle relative to the original direction of the propagation of the incident light. Although this dissertation primarily focuses on light scattering, light absorption of the particle can also be quantified based on the Mie coefficients if the complex relative refractive index of the particle is known.

Due to their geometric simplicity and symmetry, the Mie solutions for spheres are most commonly used to represent disperse scattering particles, unless another regular geometry is known. Additionally, spheres are symmetrical; therefore, the degrees of freedom concerning the particle orientation can be omitted from calculations. Other geometrically symmetrical shapes, such as ellipses and cylinders, also have analytical Mie solutions, although they are considerably more involved and are also highly sensitive to the particle orientation relative to the polarization state of incident light (See **Chapter 4**). All such solutions are open-form and must be calculated numerically. Non-geometric shapes typically have no open- or closed-form analytical Mie solution; therefore, it is necessary to assume a geometric shape when modeling real physical particles. In the case of tissues, a sphere is generally assumed as the average shape of the scattering particle, unless a specific geometric organization is known. Although this presumption may result in errors in the calculation of scattering phase functions for single particles, the average of many scattering events from a collection of many particles are typically considered, and these errors are subsequently less impactful.

2.2.1 The Mie Coefficients

The complete derivation of the Mie solution is extensive and has been exhaustively described in many studies. This dissertation instead begins from the direct outputs of the solution, the Mie coefficients $\boldsymbol{a_n}(\boldsymbol{x}, \boldsymbol{m})$ and $\boldsymbol{b_n}(\boldsymbol{x}, \boldsymbol{m})$, solved for the case of a spherical particle. Bohren and Huffman, among others, describe the complete derivation and computationally efficient methods used for calculating the Mie coefficients in this research (Bohren and Huffman 2008). The inputs required to solve the Mie coefficients include the relative index of refraction ($\boldsymbol{m}$) and the size parameter ($\boldsymbol{x}$). The relative index of refraction is a ratio of the index of refraction of the particle ($\boldsymbol{n_{sph}}$) to the index of refraction of the

medium surrounding the particle ($\boldsymbol{n_{med}}$); it has both real and complex components. High values for the real part of m typically indicate "optical hardness" of particles, which means that reflections from the surface of the particle account for most of the total scattering. High values of the imaginary relative refractive index indicate high absorption of light by the particle. The size parameter, $\boldsymbol{x}$, is an important term that describes the size of the particle relative to the wavelength of incident light:

$$x = \frac{2\pi n_{med} r}{\lambda} \quad \textbf{(2.15)}$$

In the equation above, $\boldsymbol{r}$ is the radius of the (assumed spherical) particle, and $\boldsymbol{\lambda}$ is the wavelength of light in the medium (scaled by $\boldsymbol{n_{med}}$). Scattering involving a small-size parameter, in which the particle is significantly smaller than the wavelength of light and the particle is optically "soft," is accurately modeled by Rayleigh's scattering theory, in which the directional scattering of light is isotropic (i.e., light is scattered equally in all directions from the particle). Conversely, scattering from optically soft particles with relatively large size parameters is described effectively by the van de Hulst approximation. However, at size parameters close to unity, when the size of the particle and wavelength of light are comparable, the directional scattering of light from these particles is more chaotic, and the Mie solution is required to accurately calculate light scattering. In the case of cells and nuclei, which are comparable in size to the wavelengths of visible light used to investigate them, this dissertation applies Mie theory to calculate scattering for our modeled particles.

2.2.2 Calculating Scattering Efficiency of Spheres

The total scattering efficiency $\boldsymbol{Q_{sca}}$ describes the total amplitude of light scattered in all directions from a particle and is used to calculate the total scattering cross-section, as discussed in **Chapter 2.1**. The scattering efficiency can be calculated for a particle with a known size parameter and relative refractive index using the Mie coefficients:

$$Q_{sca} = \frac{2}{x^2}\sum_{n=1}^{\infty}(2n+1)(|a_n(x,m)|^2 + |b_n(x,m)|^2) \quad \textbf{(2.16)}$$

While the exact form of the equation calls for an infinite sum, numerical computations converge to a solution significantly before this value. An appropriate number of summations has been suggested by Bohren and Huffman, such that $\boldsymbol{n_{stop} = x + 4x^{1/3} + 2}$ (Bohren and Huffman 2008). Since $\boldsymbol{n_{stop}}$ is entirely dependent upon the size parameter, particles that are large relative to the wavelength of light are more computationally expensive to compute. However, the largest particles typically considered when modeling tissue are approximately $100\ \mu m$, which results in a manageable maximum $\boldsymbol{n_{stop}}$ of around 5,000 for visible light. This suggested $\boldsymbol{n_{stop}}$ value was used as the number of summations for all numerical solutions in this research.

2.2.3 Calculating Extinction and Absorption Efficiency of Spheres

The extinction efficiency, Q_{ext}, describes the amount of light that is either absorbed or scattered by the particle. Therefore, Q_{ext} contains contributions from both the scattering efficiency (Q_{sca}) and the absorption efficiency (Q_{abs}) of a particle, such that $Q_{ext} = Q_{abs} + Q_{sca}$. The extinction efficiency is also calculated using the Mie coefficients as follows:

$$Q_{ext} = \frac{2}{x^2}\sum_{n=1}^{\infty}(2n+1)Re\{a_n(x,m) + b_n(x,m)\} \quad \textbf{(2.17)}$$

The absorption efficiency can then be determined by subtracting the scattering efficiency from the extinction efficiency.

2.2.4 Calculating the Scattering Phase Function

The angular representation of the phase function $\boldsymbol{p(\theta)}$ is a complete description of the far-field amplitude of light scattered in all directions ($\boldsymbol{\theta}$) relative to the initial direction of incident light. Notably, this is mathematically equivalent to the phase function in **Chapter 2.1**, although here, it is represented in a truncated angular form. The phase function is calculated from the Mie coefficients as follows:

$$p(\theta) = \frac{1}{x^2}(|S_1|^2 + |S_2|^2) \tag{2.18}$$

Above, $\boldsymbol{S_1}$ and $\boldsymbol{S_2}$ are the amplitudes of the transverse components of the scattered electric field, yielded by the following:

$$S_1(\theta) = \sum_{n=1}^{\infty} \frac{2n+1}{n(n+1)}\left(a_n(x,m)\pi_n(\Omega) + b_n(x,m)\tau_n(\Omega)\right) \tag{2.19}$$

$$S_2(\theta) = \sum_{n=1}^{\infty} \frac{2n+1}{n(n+1)}\left(b_n(x,m)\pi_n(\Omega) + a_n(x,m)\tau_n(\Omega)\right) \tag{2.20}$$

Above, $\boldsymbol{\pi_n}$ and $\boldsymbol{\tau_n}$ are recursive functions containing the Legendre polynomials, which describe the shape of the angular scattering. These Legendre polynomials indicate scattering across solid angles $\boldsymbol{\Omega}$. However, this shape is symmetrical over the azimuthal components of the solid angles in the case of unpolarized light incidents on spheres, and integrating over these angles results in a phase function that solely depends upon the polar angle ($\boldsymbol{\theta}$) relative to the incident angle of light. Furthermore, the resulting phase function is normalized such that its integral over the polar angles equals 1:

$$\int_0^{\pi} p(\theta) 2\pi \sin\theta \, d\theta = 1 \tag{2.21}$$

Figure 2.3 illustrates the log-normalized phase functions calculated for the scattering of green light ($\lambda = 530nm$) from particles with a range of physiologically-relevant sizes ($\boldsymbol{r_{sph}} = 100\,nm\ to\ 10\,\mu m$) and relative refractive index ($\boldsymbol{m} = 1.03$). Firstly, smaller size parameters tend to exhibit highly isotropic scattering, while larger size parameters exhibit highly anisotropic scattering in the forward direction. Secondly, there are highly distinctive changes to the phase functions within this physiological range of size parameters. Both of these observations indicate that sensitivity to angular scattering provides insight into the relative sizes of the scattering particles.

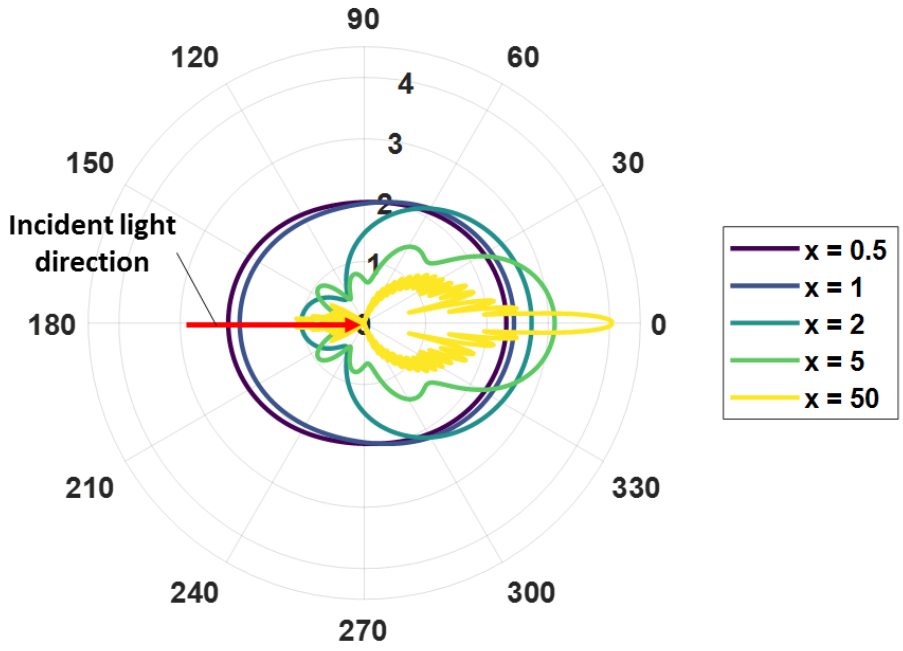

Figure 2.3: Log-normalized scattering phase functions for different size parameters, calculated from Mie theory. This demonstrates a transition from isotropic scattering to anisotropic forward-scattering as the size parameter increases.

2.2.5 Scattering Phase Function Parameters

While the phase function fully defines directional light scattering from particles, the degree of angular accuracy computed by the Mie solution is often excessive for modeling light propagation in turbid media and is also difficult to measure with high angular resolution from many particles. In tissues and other samples, fluctuations in actual particle shapes (which are not invariably perfectly spherical) and distributions of particle sizes and relative refractive indices cause these phase functions to "blur." Instead, it is useful to utilize summary parameters to describe the general characteristics of the phase functions, which remain relatively constant despite the "blurring" of the phase function by distributions of particle shape, size, and refractive index. These summary parameters are typically based on mathematical moments described using Legendre polynomials, $\boldsymbol{P_n(cos\theta)}$. The number of Legendre moments necessary to accurately estimate the exact phase function is the $\boldsymbol{n_{stop}}$ value, as discussed in **Chapter 2.2.2**. In practice, only the first several Legendre moments are necessary to characterize the anisotropic scattering of particles, primarily due to "blurring" by particle populations, as discussed previously.

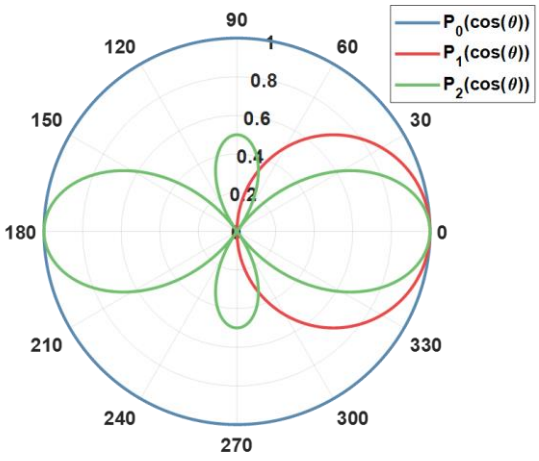

Figure 2.4: This illustrates the first several Legendre polynomials, the moments of which are used to define diffuse ($\boldsymbol{g}$) and sub-diffuse ($\boldsymbol{\gamma}$) optical anisotropy parameters.

2.2.5.1 The diffuse scattering anisotropy parameter g

The moment of the first Legendre polynomial, $\boldsymbol{g_1}$ (commonly referred to simply as $\boldsymbol{g}$), describes the proportion of scattered light which maintains its propagation in the same direction as the incident light. Referred to as the scattering anisotropy, $\boldsymbol{g}$ can be defined mathematically as follows:

$$g = g_1 = \langle cos(\theta) \rangle = \int_0^{\pi} p(\theta)\, cos(\theta)\, 2\pi\, sin(\theta)\, d\theta \qquad \textbf{(2.22)}$$

A $\boldsymbol{g}$ value of 0 indicates completely isotropic scattering, which typically applies to particles where $\boldsymbol{x} < 1$. A $\boldsymbol{g}$ value of 1 indicates that all light is scattered in the forward direction (the same direction as the incident light). As indicated in **Figure 2.5**, tissues have high-bulk anisotropy values, typically between $0.85\ and\ 0.95$, which suggests that the light scattering is primarily in the forward direction (Cheong, Prahl et al. 1990, Jacques 2013).

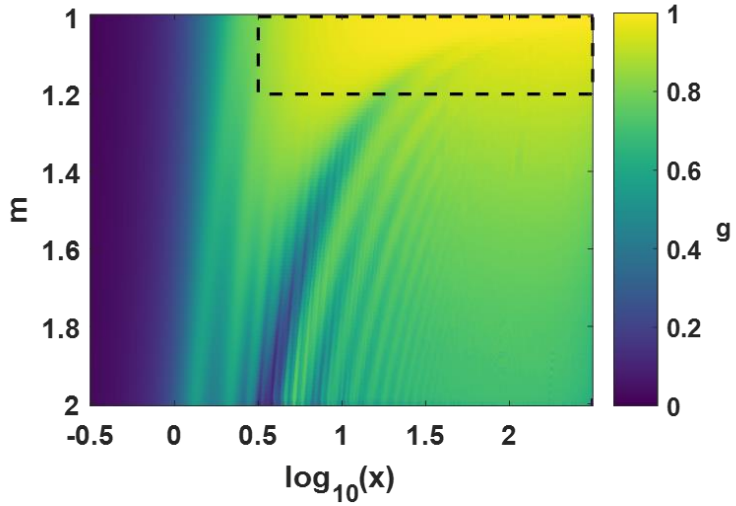

Figure 2.5: Mie calculations of the diffuse anisotropy parameter $\boldsymbol{g}$,as a function of size parameter $\boldsymbol{x}$ and relative refractive index $\boldsymbol{m}$. Within the tissue range of $\boldsymbol{x}$ and $\boldsymbol{m}$ (dashed box), $\boldsymbol{g}$ is relatively stable.

In diffusion theory, the $\boldsymbol{P_1}$ approximation refers to the ability to use only the moment ($\boldsymbol{g}$) of the first Legendre polynomial ($\boldsymbol{P_1}$) to predict bulk diffusion of light in turbid media. **Chapter 2.1.3** presents a more detailed discussion of $\boldsymbol{g}$ in the diffusion regime.

2.2.5.2 The sub-diffuse scattering anisotropy parameter $\boldsymbol{\gamma}$

The $\boldsymbol{g}$ parameter was introduced as a correction factor for the transport length of anisotropy scattering in diffuse light propagation. However, it is more challenging to decouple anisotropy from the reduced scattering coefficient in reflectance measurements within the confines of the diffusion regime; even if it is decoupled, $\boldsymbol{g}$ alone does not provide significant information about the structure of the scattering particle, as illustrated in **Figure 2.5**. A second phase function term $\boldsymbol{\gamma}$ has been suggested to achieve additional sensitivity to changes in particle size (Bevilacqua and Depeursinge 1999, Chamot, Migacheva et al. 2010). Chamot et al. present a physical interpretation the second order phase function term and directly relate it to the fractal dimension of the particle size distribution (Chamot, Migacheva et al. 2010, McClatchy, Rizzo et al. 2016). As average particle size decreases relative to the wavelength of incident light, the $\boldsymbol{\gamma}$ parameter also decreases (**Figure 2.6**). The $\boldsymbol{\gamma}$ parameter is calculated as a ratio of the first two Legendre moments of the phase function as follows:

$$\gamma = \frac{1 - g_2}{1 - g_1} \tag{2.23}$$

However, the $\boldsymbol{\gamma}$ parameter cannot be incorporated into the current model for light diffusion because its impact is primarily in ballistic scattering events in which high-angle scattering (backscattering) occurs. To measure the $\boldsymbol{\gamma}$ parameter, light propagation in the sub-diffuse regime must be considered, which requires measurements of light transport beyond the diffusion regime.

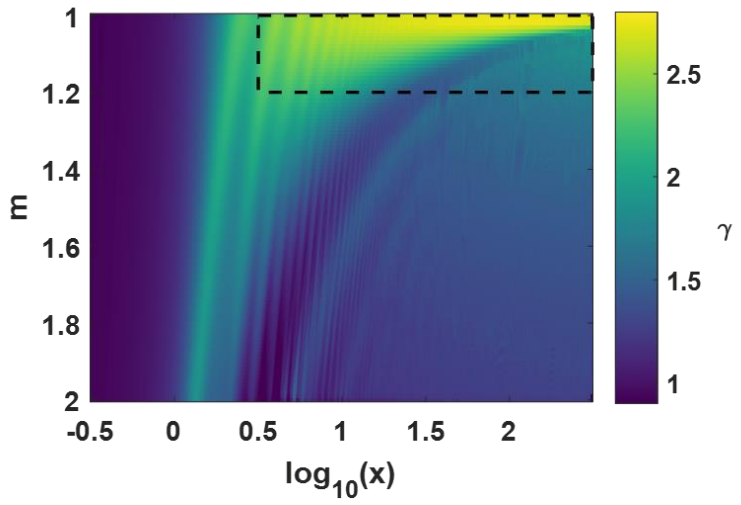

Figure 2.6: Mie calculations illustrate the sub-diffuse anisotropy parameter $\boldsymbol{\gamma}$ as a function of size parameter $\boldsymbol{x}$ and relative refractive index $\boldsymbol{m}$; this indicates that sub-diffuse scattering can be used to probe tissue ranges of $\boldsymbol{x}$ and $\boldsymbol{m}$.

2.2.5.3 Higher-order Parameters

Any number of higher-order Legendre moments can be used to describe the phase function with increasing degrees of accuracy, but there are diminishing returns in terms of both calculating and measuring these descriptors in practice. However, notable improvements in characterizing phase functions have been described by increasing the number of high-order Legendre moments (Bevilacqua and Depeursinge 1999, Hull and Foster 2001, Bodenschatz, Krauter et al. 2016). The $\boldsymbol{\sigma}$ parameter is a tractable weighted sum of an infinite number of Legendre moments and has been found to describe a broad range of phase functions models accurately. To date, the use of this parameter to quantify phase functions in real measurements has been minimal and confined to numerical and computational methods (Bodenschatz, Krauter et al. 2016). However, numerical studies suggest that improved accuracy in quantifying the phase function may be achieved by using the $\boldsymbol{\sigma}$ term; this should be considered for future research related to quantifying tissue microstructure.

2.3 SPATIAL FREQUENCY DOMAIN IMAGING (SFDI)

2.3.1 SFDI Background

Spatial frequency domain imaging (**SFDI**) is a wide-field structured illumination technique in which spatial frequency patterns are projected onto a sample and subsequently imaged. The manner in which the spatial frequency patterns are attenuated by the scattering and absorption of the sample allows the optical properties to be probed across spatial dimensions (Dögnitz and Wagnières 1998). This technique was first adopted in practice by Cuccia et al. Since then, it has spawned a substantial body of research concerning fundamental instrumentation and processing improvements and biomedical applications (Cuccia, Bevilacqua et al. 2004, Cuccia, Bevilacqua et al. 2005, Cuccia, Bevilacqua et al. 2009, Angelo, Chen et al. 2018). Wide-field scattering and absorption maps extracted with SFDI enable the non-invasive quantification of tissues at tissue-level scales. Furthermore, scattering and absorption measured at multiple wavelengths can be used to calculate relative and absolute values of crucial biophysical chromophores, including hemoglobin, blood-oxygen saturation, and collagen and lipid content (Cuccia, Bevilacqua et al. 2009, Mazhar, Dell et al. 2010, Gioux, Stockdale et al. 2011).

Spatial frequency domain imaging has been implemented in a variety of pre-clinical studies to monitor the biophysical conditions of live and excised tissues; this has been applied to pressure ulcers from diabetes and prolonged hospital stays (Yafi, Muakkassa et al. 2017), tumor margin assessment in breast and skin tissues (Laughney, Krishnaswamy et al. 2013, Rohrbach, Muffoletto et al. 2014), brain tissues (Lin, Koike et al. 2011), burn assessment (Mazhar, Saggese et al. 2014, Ponticorvo, Burmeister et al. 2014), and skin-flap transplant viability (Yafi, Vetter et al. 2011, Ponticorvo, Taydas et al. 2013); it has been implemented via endoscope as a surgical guidance tool (Angelo, van de Giessen et al. 2017). In fluorescence imaging, **SFDI** can be used to enhance contrast and quantification of fluorophore concentrations (Mazhar, Cuccia et al. 2010, Yang, Sharma et al. 2013, Angelo, Venugopal et al. 2014, Valdes, Angelo et al. 2017). Many of these techniques utilize previous research concerning probe-based diffuse optical tomography

and spectroscopy as a theoretical basis, as both techniques utilize the same models of light transport. Spatial frequency domain imaging possesses the additional benefit of spatial sampling to provide the morphological context of these measurements.

In addition to *in vivo* biological tissue research, **SFDI** offers immense potential for rapid, non-invasive cancer screening and tumor margin assessment (Laughney, Krishnaswamy et al. 2013). In histopathology, the gold standard for diagnosis, physicians search biopsied tissues for signs of abnormal cellular structure, which is often manifested as atypical sizes or grouping of cells and nuclei in the regions of tumors (Elston and Ellis 1991, Madan, Lear et al. 2010). The local microstructure in the context of its global morphological location is crucial to identifying tumor regions (**Chapter 3**). The ability to quantitatively measure this microstructure across large fields of view of intact, non-treated tissues would be extremely beneficial; sectioning and staining is a major time constraint in the diagnostic workflow and may cause physical alterations to the native tissue state.

For increased sensitivity to tissue microstructures, **SFDI** measurements must be considered beyond the diffusion regime in which higher orders of the scattering phase function can be measured. Recent research concerning **SFDI** for use in tumor margin assessment have used high spatial frequencies to probe the sub-diffuse optical properties of tissue, often referred to as **sd-SFDI** (Kanick, McClatchy et al. 2014, Bodenschatz, Krauter et al. 2015, Bodenschatz, Krauter et al. 2015, Bodenschatz, Krauter et al. 2016). McClatchy et al. were among the first to demonstrate the ability to match maps of sub-diffuse optical properties with histopathological morphology in breast tumors (McClatchy, Rizzo et al. 2016, McClatchy III, Hoopes et al. 2017) and recently extended this research to differentiate between stromal, epithelial, and fatty tissue regions and perform automated segmentation of tumor margins (McClatchy, Rizzo et al. 2018). Lin et al. demonstrated similar results in their ability to differentiate between normal, inflamed, and cancerous regions in cervical tissues using high spatial frequency **SFDI** (Lin, Zeng et al. 2018). While sensitivity to absorption is lost in **sd-SFDI** imaging (Bodenschatz, Krauter et al. 2015), Laughney et al. note that chromophore identification does not meaningfully improve the

diagnostic power of **SFDI** systems in differentiating breast tissue pathology relative to the scattering properties (Laughney, Krishnaswamy et al. 2013).

2.3.2 Basic SFDI Theory

Figure 2.7a illustrates the geometry of a typical **SFDI** system. The angle of the projector with respect to the optical axis is entirely confined to the $\boldsymbol{YZ}$-plane; therefore, the spatial frequency pattern, oriented in the $\boldsymbol{x}$-direction, is uniform across the imaging plane. This contrasts with **Figure 2.7b**, in which the spatial frequency pattern is oriented in the $\boldsymbol{y}$-direction.

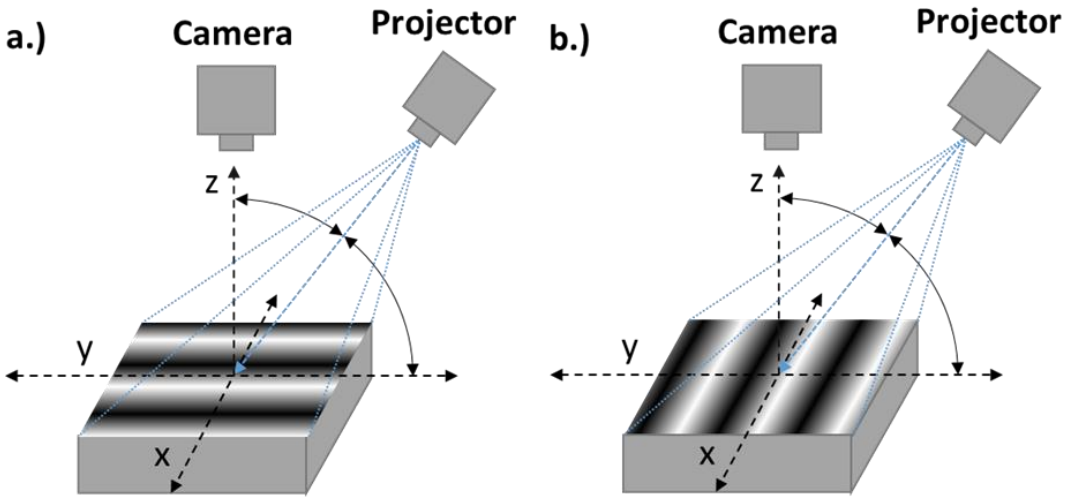

Figure 2.7: Spatial Frequency Domain Imaging (**SFDI**) system geometries in **(a)** typical orientation and **(b)** atypical orientation. The typical orientation ensures that the spatial frequency and phase do not change as a function of sample height, while the atypical orientation can be used to measure surface topography.

Linear sinusoidal spatial frequency patterns are most commonly used, and these patterns are characterized as classical waveforms by their **DC** amplitude ($\boldsymbol{I_{DC}}$), **AC** amplitude ($\boldsymbol{I_{AC}}$), spatial frequency ($\boldsymbol{f_x}$), and phase ($\boldsymbol{\phi}$). The amplitude of the pattern at any

point in the imaging plane for a sinusoidal spatial frequency pattern oriented in the x-direction is yielded by the following equation:

$$I(x,y) = I_{DC}(x,y) + I_{AC}(x,y)\cos(2\pi f_x x + \phi) \quad \textbf{(2.24)}$$

The geometry of most **SFDI** systems (**Figure 2.7a**) ensures that the spatial frequency and phase of the pattern remain effectively constant throughout the imaging plane. However, in turbid samples, the scattering and absorption of light attenuates the amplitude of the **DC** and **AC** amplitude components. Images of the sample under patterned illumination represent the modulated (attenuated) reflectance components of the initial spatial frequency pattern. Attenuation of the $\boldsymbol{I_{DC}}$ component is related to the optical properties of the sample and primarily depends upon the reduced scattering and absorption of the sample. Attenuation of the $\boldsymbol{I_{AC}}$ component depends upon both the optical properties of the sample and the frequency of the spatial pattern that is projected onto the sample. Therefore, the modulated intensity detected by the camera is as follows:

$$M(x,y,f_x,\varphi) = M_{DC}(x,y) + M_{AC}(x,y,f_x)\cos(2\pi f_x x + \phi) \quad \textbf{(2.25)}$$

By measuring the modulated reflectance at several spatial frequencies, optical properties of the sample can be determined using analytical fitting models or lookup tables (See **Figure 2.8** and **Chapter 2.3.3**). The curve of the modulated **AC** reflectance illustrates that turbid samples act similarly to low-pass frequency-dependent reflectance filters; this frequency-dependence is determined by the optical properties of the sample.

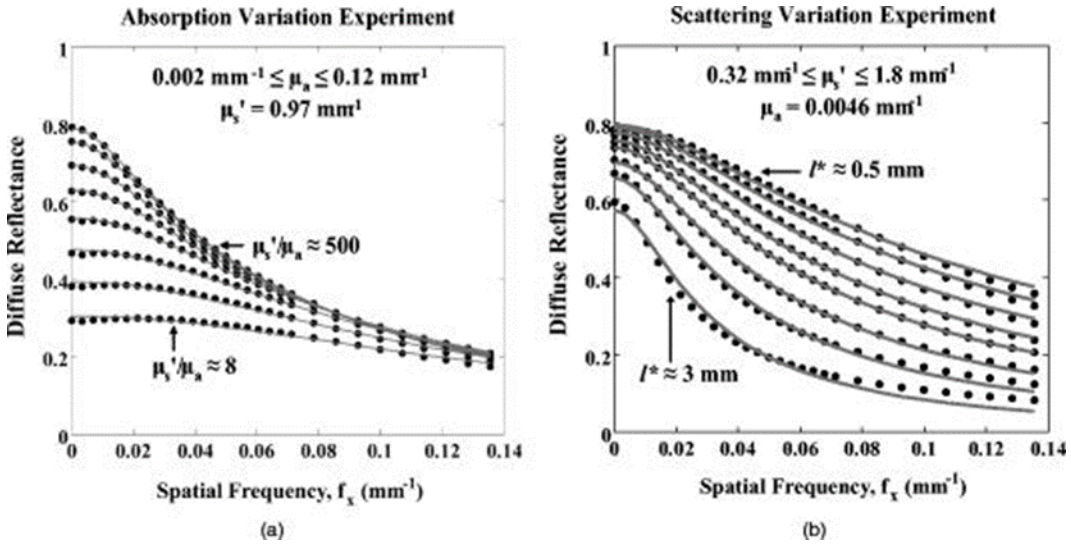

Figure 2.8: Above, modulated diffuse reflectance as a function of spatial frequency has been measured experimentally (dots) and calculated using the diffusion approximation (lines) for a physiologically relevant range of bulk absorption and scattering coefficients; this demonstrates the ability to sample optical properties with diffuse reflectance in the spatial frequency domain (Cuccia, Bevilacqua et al. 2009).

Demodulation refers to extracting the modulated reflectance components from spatial frequency images. Several strategies borrowed from signal processing have been used to demodulate the images, but this dissertation exclusively discusses the most commonly used technique: three-phase demodulation (Cuccia, Bevilacqua et al. 2004). For this technique, a sinusoidal pattern with a known spatial frequency is projected onto a sample, and the sample is imaged. This spatial frequency pattern is shifted in phase twice by 120°, and the sample is imaged at each phase, yielding three total images:

$$I_1 = I_{0^\circ}(x,y),\ \ I_2 = I_{120^\circ}(x,y),\ \ I_3 = I_{240^\circ}(x,y) \qquad \textbf{(2.26)}$$

The modulated **AC** and **DC** reflectance components can be recovered from the three phase images at each point through the following demodulation formulae:

$$M_{DC}(x,y) = \frac{I_1 + I_2 + I_3}{3} \quad \textbf{(2.27)}$$

$$M_{AC}(x,y) = \frac{\sqrt{2[(I_1 - I_2)^2 + (I_2 - I_3)^2 + (I_3 - I_1)^2]}}{3} \quad \textbf{(2.28)}$$

Additionally, the phase at each image location can be demodulated by the following:

$$\phi(x,y) = atan2\left[\frac{\sum_{n=0}^{N-1} I_{n+1}\, sin\left(\frac{2\pi n}{N}\right)}{\sum_{n=0}^{N-1} I_{n+1}\, cos\left(\frac{2\pi n}{N}\right)}\right], \; N = 3 \quad \textbf{(2.29)}$$

In most configurations of SFDI systems, the phase term should be constant and is therefore not often calculated; however, this does not indicate that the phase is unimportant. If the atypical system configuration in **Figure 2.7b** is used, then the phase will directly correlate with sample height and can therefore be used to reconstruct surface topology of the sample, as **Chapter 5** demonstrates (Srinivasan, Liu et al. 1984, Zhou and Su 1994, Gioux, Mazhar et al. 2009). Additionally, the phase information is vital to accurately reconstruct the demodulated images through other demodulation techniques. Several advanced demodulation techniques which require only one or two images (rather than three) are useful for decreasing the imaging time and data storage requirements and allowing for video-rate imaging and real-time display of **SFDI** images. These techniques include single-snapshot **SFDI** (Vervandier and Gioux 2013), multi-frequency synthesis and extraction (Nadeau, Rice et al. 2015), Gram-Schmidt orthonormalization (Vargas, Quiroga et al. 2012, Lu, Li et al. 2016), and Hilbert-transform or spiral-phase demodulation (Nadeau, Durkin et al. 2014, Lu, Li et al. 2016). However, the primary tradeoffs in these techniques include the increased processing complexity and introduction of image artifacts

that result from Fourier domain processing. In particular, "banding" artifacts from demodulation at low signal levels and "ripple" artifacts from discrete 2D Fourier transforms are common in many single- and two-image SFDI demodulation techniques and diminish the final image quality (Vervandier and Gioux 2013, Nadeau, Durkin et al. 2014, Nadeau, Rice et al. 2015). Since most of the imaging experiments and applications outlined in this dissertation are early-stage and do not require rapid acquisition, these reduced-frame SFDI techniques are merely considered for future research.

2.3.3 Volumetric Sampling in the Spatial Frequency Domain

The sampling resolution of **SFDI** systems depends upon both the optical properties of the sample and the spatial frequencies used. The effective transport length ($\boldsymbol{\delta_{eff}}$) for wide-field imaging under planar illumination is inversely proportional to the effective transport coefficient, which was derived in **Chapter 2.2**:

$$\delta_{eff} = \frac{1}{\mu_{eff}} = \frac{1}{\sqrt{\left(3\mu_a(\mu_a + \mu_s')\right)}} \tag{2.30}$$

This value represents the average distance over which scattering and absorption events are sampled. In the spatial frequency domain, a modified effective transport length which is sampled, $\boldsymbol{\delta'_{eff}}$, can be determined by incorporating spatially-varying sinusoidal illumination (**EQ 2.24**) as the source term in the diffusion approximation of the radiative transport equation (**EQ 2.13**) (Cuccia, Bevilacqua et al. 2009, Konecky, Mazhar et al. 2009). The spatial frequency-dependent effective transport length is as follows:

$$\delta'_{eff} = \frac{1}{\mu'_{eff}} = \frac{1}{\sqrt{\left(\mu_{eff}^2 + (2\pi f_x)^2\right)}} \tag{2.31}$$

This modified effective transport length defines the sampling length of an **SFDI** system for a given set of sample optical properties and spatial frequencies used. Several important implications relate to these effective transport lengths. First, for reflectance measured under planar illumination, where spatial frequency $\boldsymbol{f_x = 0}$, the effective sampling length of the reflectance only depends upon the diffuse optical properties of the sample ($\boldsymbol{\delta'_{eff} = \delta_{eff}}$). As spatial frequency increases, the effective sampling length decreases, and the spatial frequency pattern is attenuated more rapidly by the turbidity of the sample (**Figure 2.9**). This was initially used as a form of rough tomography by Cuccia et al.; however, in samples with similar turbidity and thickness relative to biological tissues, the tomographic reconstruction capabilities are limited (Cuccia, Bevilacqua et al. 2004, Cuccia, Bevilacqua et al. 2005, Konecky, Mazhar et al. 2009, O'Sullivan, Cerussi et al. 2012). However, high spatial frequency imaging can be applied to decrease the sampling depths of measurements and limit the reflectance measurements to fewer scattering events which occur near the surface of the sample.

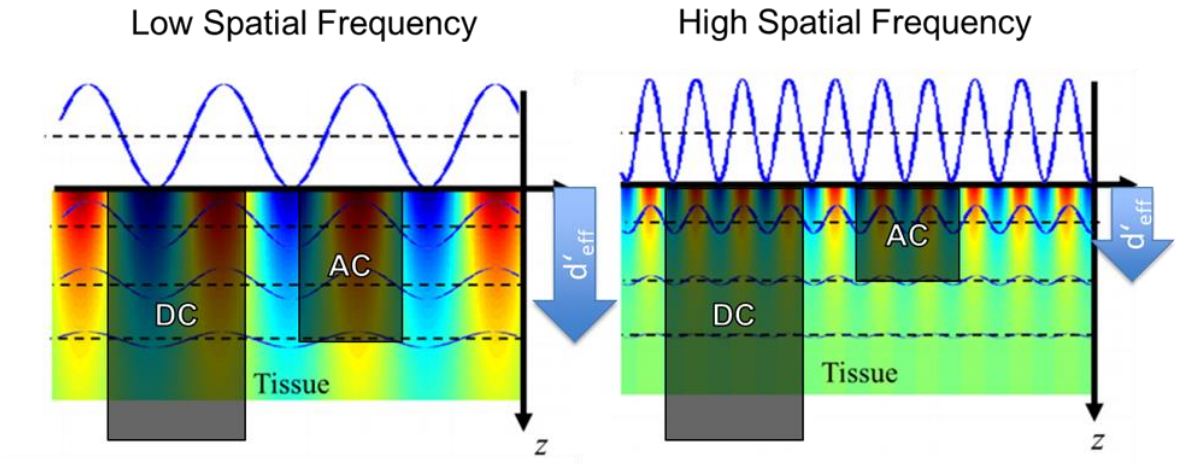

Figure 2.9: High spatial frequency patterns diffuse more rapidly in turbid media, such as tissue, relative to low spatial frequency patterns. Therefore, higher spatial frequency patterns sample shallower volumes near the surface of the sample Modified from (O'Sullivan, Cerussi et al. 2012).

This is particularly useful in relation to depth gating of fluorescence (Mazhar, Cuccia et al. 2010, Yang, Sharma et al. 2013) and polarization measurements (Yang, Lesicko et al. 2014, Goth, Yang et al. 2015, Yang, Lesicko et al. 2015, Goth, Yang et al. 2016), the latter of which are used in **Chapter 4**.

As multiple spatial frequencies are often utilized to construct optical property maps of samples, the lowest spatial frequency should be used when considering the sampling volume. Additionally, **EQ 2.31** is only valid for spatial frequencies within the diffusion regime, in which $\boldsymbol{f_x < \mu_{eff}/3}$ (**Chapter 2.2.4**). For tissues, this limits the maximum spatial frequency to around $0.25\ to\ 0.33\ mm^{-1}$, which results in an effective transport length of around $0.7\ to\ 1.0\ mm$. At higher spatial frequencies, the effective sampling length continues to decrease but is also dependent upon the higher-order phase function parameters. Bodenschatz et al. provide numerical estimations of $\boldsymbol{\delta'_{eff}}$ for high spatial frequencies by recording the maximum depth achieved by 50% of the photons (**Figure 2.10**), based on the optical properties of the sample (Bodenschatz, Krauter et al. 2015). Hayakawa et al. performed a similar study that demonstrated substantial agreement and also estimated sampling depths for a variety of common tissue types (Hayakawa, Karrobi et al. 2018).

A second important observation is that it is difficult to define an exact sampling resolution because the modified effective transport length represents a mean distance of photon transport. Some reflectance will represent scattering and absorption events that occurred over a smaller distance, and some reflectance will correspond with larger distances between events. As a result, defining the resolution based on the transport length will only provide average resolution, while actual resolution will be slightly inferior.

Third, the shape of the sampling volume is not simply a half-sphere with a radius of the modified effective transport length with the center at the pixel center. If the physical size of a pixel in a wide-field image is less than the effective transport length of the sample in that area, then the reflectance sampled from that pixel will also include scattering and absorption information from a volume surrounding the pixel. As a result, the true effective

sampling length of a pixel will extend up to one effective transport length from the edge of the pixel.

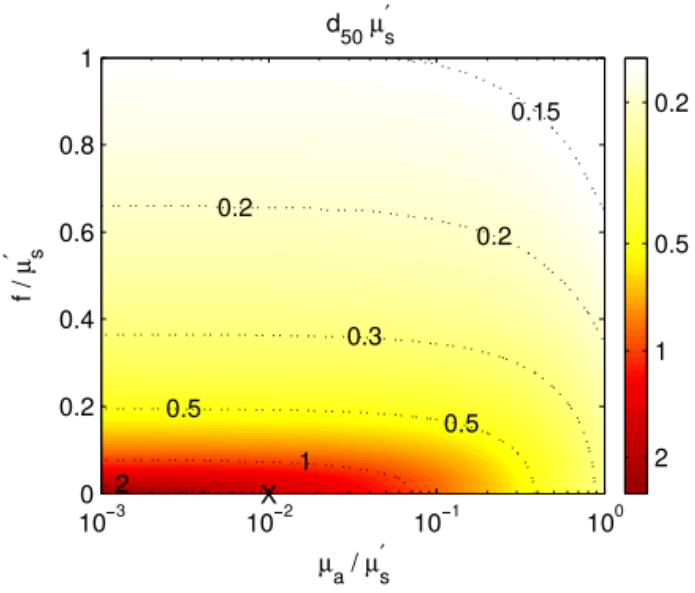

Figure 2.10: Effective mean sampling depth as a function of spatial frequency and bulk sample absorption, both normalized by bulk sample reduced scattering. Monte Carlo numerical computation by Bodenschatz et al. (Bodenschatz, Krauter et al. 2015).

Finally, only homogeneous samples have been considered thus far. In the case of the spatial heterogeneity of optical properties, the sampling length is complicated further. A study of SFDI by Laughney et al. investigated axial and lateral resolution depending upon the contrast level between an inclusion and the surrounding media (Laughney, Krishnaswamy et al. 2013); their results demonstrated that within the limits of the diffusion regime, inclusions with around 30% contrast in reflectance as small as $1.25\,mm$ in diameter embedded up to $1.5\,mm$ deep in the phantom could be distinguished.

2.3.4 Models of Reflectance in the Spatial Frequency Domain

To extract optical properties from modulated reflectance, the modulated reflectance data is fit to a model or lookup table that describes normalized reflectance ($\boldsymbol{R_d}$) as a function of the optical properties of interest and spatial frequency. Before fitting, the modulated reflectance curve for an unknown sample is normalized through measurements and model curves of a known sample:

$$R_d^{sample}(x, y, f_x) = \left[\frac{M_{AC}^{sample}(x, y, f_x)}{M_{AC}^{reference}(x, y, f_x)}\right] R_d^{reference}(f_x) \quad \textbf{(2.32)}$$

This step ensures that measurements and model spaces are both normalized to the same order of magnitude and that the system-specific modulation transfer function (**MTF**) of the system is eliminated from the measurements (Konecky, Mazhar et al. 2009).

Reflectance models based on analytical derivations from light diffusion theory are ideal, although empirical and numerical models can also be used. Cuccia et al. originally derived an analytical model for normalized steady-state reflectance in the diffusion regime based on the radiative transport equation (Cuccia, Bevilacqua et al. 2009).

$$R_d(\mu_a, \mu_s', f_x) = \frac{3A\mu_s'/\mu_{tr}}{\left(\frac{\mu_{eff}'}{\mu_{tr}} + 1\right)\left(\frac{\mu_{eff}'}{\mu_{tr}} + 3A\right)} \quad \textbf{(2.33)}$$

$\boldsymbol{A}$ is a proportionality constant which accounts for boundary conditions at the sample surface and is dependent upon the approximate bulk sample refractive index (Haskell, Svaasand et al. 1994). However, this model is limited to the diffusion regime; therefore, the higher-order moments of the scattering phase function are not accounted for. For modulated reflectance to be sensitive to higher-order moments of the scattering phase function, reflectance must be measured in the sub-diffuse regime, in which only scattering events within the first mean-free-path of the sample are considered. This can be achieved

using high spatial frequencies, as discussed in the previous section. A reflectance model which incorporates higher-order scattering phase function moments is necessary to appropriately fit reflectance data and extract optical properties at sub-diffuse spatial frequencies. One additional benefit is that in tissue, in which the mean-free-path of scattering is significantly less than the mean-free path of absorption, reflectance in the sub-diffuse regime becomes primarily dependent upon scattering, and absorption can typically be ignored (Bevilacqua and Depeursinge 1999, Bodenschatz, Krauter et al. 2015).

Kanick et al. developed a semi-empirical/semi-analytical model for reflectance in the sub-diffuse regime, derived in part from light transport theory for fiber probes with close source-detector separations (Kanick, McClatchy et al. 2014). This model incorporates $\boldsymbol{\mu_s'}$ and the sub-diffuse scattering parameter $\boldsymbol{\gamma}$:

$$R_d(\mu_s', \gamma, f_x) = \eta\left(1 + (\zeta_4\gamma^{-2})(\mu_s' f_x^{-1})^{(-\zeta_3\gamma)}\right)\left[\frac{(\mu_s' f_x^{-1})^{(\zeta_2\gamma)}}{\zeta_1\gamma^2 + (\mu_s' f_x^{-1})^{(\zeta_2\gamma)}}\right] \quad \textbf{(2.34)}$$

In the equation above, $\boldsymbol{\eta}$ and $\boldsymbol{\zeta_{1-4}}$ are system-specific parameters which must first be measured for a given SFDI system empirically. Notably, this empirical model is limited to typical scattering and absorption properties of tissues, with a reduced scattering range of $\boldsymbol{\mu_s'} = 0.1 - 10\ mm^{-1}$, a high amount of forward scattering anisotropies ($\boldsymbol{g} > 0.4$), and $\boldsymbol{\gamma} > 1.4$. These constraints limit measurements to particle sizes above the Rayleigh regime of scattering, which is appropriate for most tissues.

Lookup tables **(LUT**s) for normalized reflectance can also be generated by experimentally measuring and recording modulated reflectance for a broad range of optical properties (Erickson, Mazhar et al. 2010) or by applying Monte Carlo methods to statistically simulate light reflectance (Angelo, Vargas et al. 2016, Naglič, Pernuš et al. 2017). While empirically-derived **LUT**s may suffer from experimental errors, Monte Carlo model accuracy is primarily only limited by the model complexity of the phase function which is sampled and computational requirements. Several reports of improved Monte Carlo models consider spatial frequency reflectance in the sub-diffuse regime (Kanick,

McClatchy et al. 2014, Bodenschatz, Krauter et al. 2015, Bodenschatz, Krauter et al. 2016, Naglič, Pernuš et al. 2017); some also include polarized light propagation (Wiest, Bodenschatz et al. 2015).

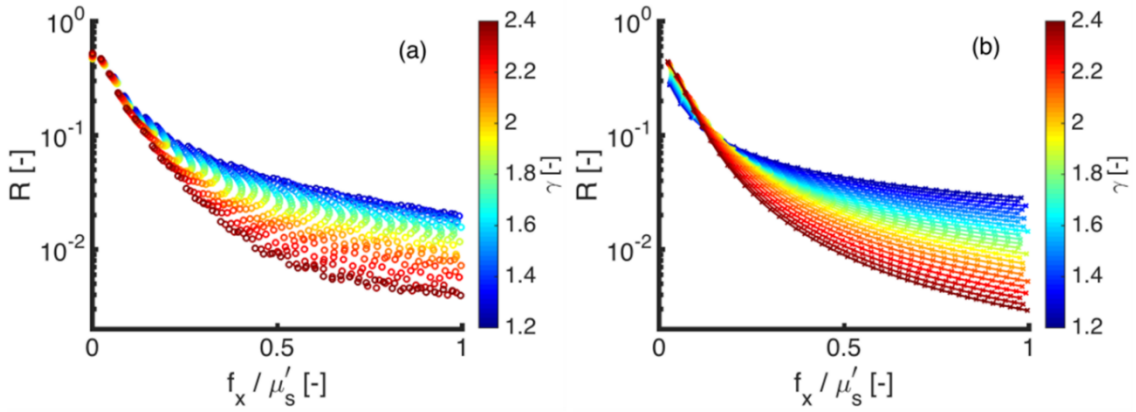

Figure 2.11: The graphs above illustrate modulated reflectance using sub-diffuse reflectance models, demonstrating the impact of the sub-diffuse scattering anisotropy parameter $\boldsymbol{\gamma}$ on reflectance at high spatial frequencies (McClatchy, Rizzo et al. 2016).

2.4 Novel Sub-diffuse SFDI Empirical Model

2.4.1 Motivation

While the time necessary for collecting **sd-SFDI** images greatly improves in terms of the sample preparation times required for traditional histopathology, the processing times required to extract the scattering parameters that are sensitive to microstructures for large images remain a limiting factor. McClatchy et al. report a processing time of 1 hour for a 3000 pixel image (McClatchy, Rizzo et al. 2016), or around 1 second per image pixel. This introduces a tradeoff in processing speed and image resolution which is non-linear: Processing more data points simultaneously requires additional computational time

(Angelo, Vargas et al. 2016). For a high-resolution ($> 1\,megapixel$) image, the processing time using the Kanick semi-empirical model is around several hours. To improve upon existing gold standard histology workflows, the processing time of **sd-SFDI techniques** must be improved.

Several strategies can be employed to improve the processing speed. In addition to parallelized-graphics processing units (**GPU**s), pre-calculated **LUT**s may be incorporated to allow ultra-fast, real-time processing of image data ($\sim 10^{-5}$ second per pixel) (Angelo, Vargas et al. 2016). However, these models have thus far only been used to extract diffuse optical properties and do not account for the sub-diffuse parameter $\boldsymbol{\gamma}$, which is pivotal in quantifying tissue structure. Lookup tables, neural networks, and other forms of artificial intelligence-based processing algorithms have been used to extract sub-diffuse optical properties rapidly ($10^{-3} - 10^{-6}$ seconds per pixel); however, they have thus far only been considered for single-point measurements (rather than being applied to images) (Naglič, Pernuš et al. 2017, Ivančič, Naglič et al. 2018). Additionally, these methods have implemented scattering and absorption measurements across the entire optical spectrum with high spectral resolution, which confines their relevancy to wide-field imaging in which multiple-wavelength imaging requires not only exponentially increased system complexity and imaging times but also large data storage requirements. There is a need for a data processing technique to rapidly extract sub-diffuse optical properties from high-spatial-frequency **sd-SFDI** data sets.

2.4.2 Empirical Power-law sd-SFDI Model

Current models of **sd-SFDI** require long fitting times due to their high degree of complexity and non-linearity. However, we observed a simplified power-law relationship between reflectance and spatial frequency when only considering reflectance in the sub-diffuse regime.

$$R_d(f_x) = \alpha f_x^{-\beta} \tag{2.35}$$

Extremely good agreement ($\boldsymbol{r^2} > 0.999$) was observed when fitting this empirical power-law model with reflectance data points generated by the Kanick model at validated spatial frequencies greater than or equal to half of the reduced scattering coefficient (i.e., beyond the limits of the diffusion regime). This prompted the hypothesis that within a physiologically-relevant range, sub-diffuse reflectance adheres to a simplified power law model, which provides a significantly less computationally-taxing method for accessing the sub-diffuse scattering parameter $\boldsymbol{\gamma}$.

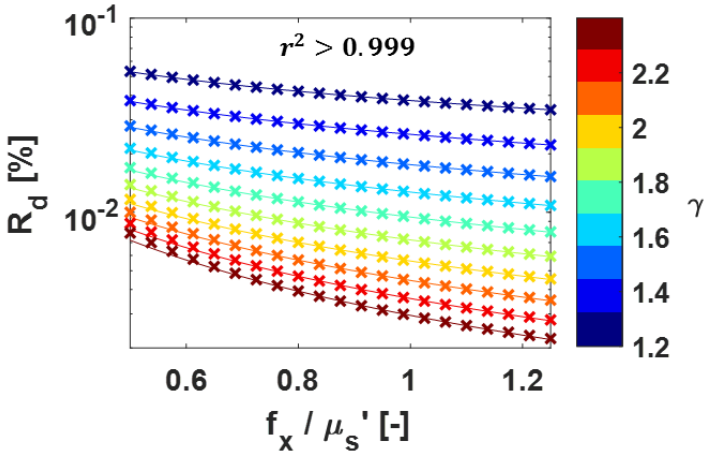

Figure 2.12: The fit of the empirical power law model with points generated by the Kanick model demonstrated substantial agreement within the sub-diffuse range of spatial frequencies.

In the simplified power-law model, $\boldsymbol{\alpha}$ and $\boldsymbol{\beta}$ are fitting coefficients related to the scattering properties of the sample in the sub-diffuse regime. Initial fits of this model with reflectance from scattering bead phantoms of different sizes demonstrated a high degree of fitting accuracy and an ability to distinguish between the sizes of the scattering beads in each phantom with the extracted fitting terms $\boldsymbol{\alpha}$ and $\boldsymbol{\beta}$. Importantly, the power law model can be linearized. The log-normalized reflectance curve for spatial frequencies is prepared as a vector and set equal to the log-normal of the empirical model:

$$\log\left(R_d(f_x)\right) = \log\left(\alpha {f_x}^{-\beta}\right) = \log(\alpha) - \beta * \log(f_x) \quad \textbf{(2.36)}$$

This relationship which contains the fitting coefficients is now in the form of a system of linear equations, which can be solved if measurements of reflectance are available for at least two different spatial frequencies. In the case of a fully-determined or over-determined system, the least-squares fit is determined through Gaussian elimination. This results in a substantially improved processing time for model fitting of less than 1 second for a 5-megapixel image.

2.4.3 Instrumentation, Calibration, and Data Processing

A typical **SFDI** system configuration (**Figure 2.7(a)**) was applied for all **sd-SFDI** experiments in this research. A DLP Lightcrafter Evaluation Module digital micro-mirror device (Texas Instruments, Dallas TX) was used to project the patterns. Bandpass filters centered at $450\ nm$, $530\ nm$, and $620\ nm$ were utilized to achieve a set of three narrow spectral bandwidths (full-width half-max values $< 15\ nm$). A plano-convex singlet lens ($\boldsymbol{f} = 15cm$) was placed in front of the stock projection lens to achieve spatial frequencies of $\boldsymbol{f_x} = 0 - 1.25\ mm^{-1}$ in $0.05\ mm^{-1}$ increments. A 5-megapixel monochrome CCD camera was used to collect images with an $80\ ms$ exposure (piA2400-17gm Basler, Ahrensburg, Germany). No polarizers were implemented in this setup to avoid gating ballistic photons (Wiest, Bodenschatz et al. 2015). Images were normalized for spatial and spectral variations in illumination, using reference images of a calibrated titanium dioxide reference standard (**Appendix A**). Prior to normalization, images of the reference standard were subjected to median and Gaussian filters to diminish salt and pepper noise. Individual pixels were then fit to the linearized empirical model.

2.4.4 Microbead Phantom Experiment

2.4.4.1 Methods

Though substantial numerical agreement has been observed between the proposed power-law model and the semi-empirical model formulated by Kanick et al., the objective of this research was to experimentally test the relationships between sub-diffuse scattering parameters ($\boldsymbol{\mu_s', \gamma}$) and the power-law model coefficients ($\boldsymbol{\alpha, \beta}$). A set of six scattering phantoms were constructed using three different sizes of polystyrene microspheres (Polysciences Inc., Warrington PA). Absorption was not used because it has been demonstrated that tissue-level absorption exerts minimal impact on spatially-resolved reflectance within the sub-diffuse regime (Bodenschatz, Krauter et al. 2015). The scattering cross-section $\boldsymbol{\sigma_{sca}}$, the anisotropy parameter $\boldsymbol{g}$, and the sub-diffuse parameter $\boldsymbol{\gamma}$ were then calculated using each of the bead mean diameters and diameter variances based on Mie theory. The necessary concentrations of each bead to achieve reduced scattering coefficients of $\boldsymbol{\mu_s'(\lambda = 530\ nm) - [2.0 mm^{-1}, 3.0\ mm^{-1}]}$ were then determined. The phantoms were each placed into a $2\ cm$ diameter well and imaged at each wavelength described in the instrumentation section; this resulted in a set of 18 unique optical property pairs. **Table 2.1** and **Table 2.2** indicate the final calculated $\boldsymbol{\mu_s'}$ and $\boldsymbol{\gamma}$ for each bead at $\boldsymbol{\lambda =}$ $530\ nm$ (a full description of the Mie calculations is presented in **Appendix B**).

Table 2.1: Mie-calculated $\boldsymbol{\mu_s'}$ for each phantom at each wavelength.

$\boldsymbol{Well}$	$\boldsymbol{\mu_s'(\lambda = 450\ nm)}$	$\boldsymbol{\mu_s'(\lambda = 530\ nm)}$	$\boldsymbol{\mu_s'(\lambda = 620\ nm)}$
1	3.60	2.00	1.11
2	5.39	3.00	1.67
3	2.26	2.00	1.54
4	3.40	3.00	2.31
5	2.16	2.00	1.87
6	3.25	3.00	2.80

Table 2.2: Mie-calculated $\boldsymbol{\gamma}$ for each phantom at each wavelength.

$\boldsymbol{Well}$	$\boldsymbol{\gamma(\lambda = 450\ nm)}$	$\boldsymbol{\gamma(\lambda = 530\ nm)}$	$\boldsymbol{\gamma(\lambda = 620\ nm)}$
1	1.03	0.99	0.97
2	1.03	0.99	0.97
3	1.80	1.44	1.24
4	1.80	1.44	1.24
5	2.08	2.14	2.17
6	2.08	2.14	2.17

2.4.4.2 Results

Figure 2.13. displays the raw images and extracted $\boldsymbol{\alpha}$ and $\boldsymbol{\beta}$ model coefficients. These results qualitatively confirmed the strong relationship between $\boldsymbol{\gamma}$ and $\boldsymbol{\beta}$. The $\boldsymbol{\alpha}$ term additionally appeared to depend upon both $\boldsymbol{\gamma}$ and $\boldsymbol{\mu_s'}$. To further characterize these relationships, small $100x100$-pixel regions-of-interest (**ROI**) from each well were selected for statistical processing at each wavelength to ensure that the **ROI** did not overlap with any areas with specular reflection apparent in the picture. A linear regression was performed to determine the relationship between the $\boldsymbol{\alpha}$ and $\boldsymbol{\beta}$ measured across the entire **ROI** and the known $\boldsymbol{\gamma}$ and $\boldsymbol{\mu_s'}$ values for each **ROI** (**Figure 2.13**).

Despite the variance in wells three and four due to specular reflections and small banding errors at high spatial frequencies, the overall trends of the model coefficients as a function of γ and μ_s' appeared to be consistent (**Figure 2.14**). The regression analysis indicated that $\boldsymbol{\alpha}$ has a weak positive correlation with $\boldsymbol{\mu_s'}$ ($r^2 = 0.27$) and a moderate negative correlation with $\boldsymbol{\gamma}$ ($r^2 = 0.71$). The β-fit coefficient has a strong positive correlation with $\boldsymbol{\gamma}$ ($r^2 = 0.95$) but nearly no correlation with $\boldsymbol{\mu_s'}$ ($r^2 = 0.004$).

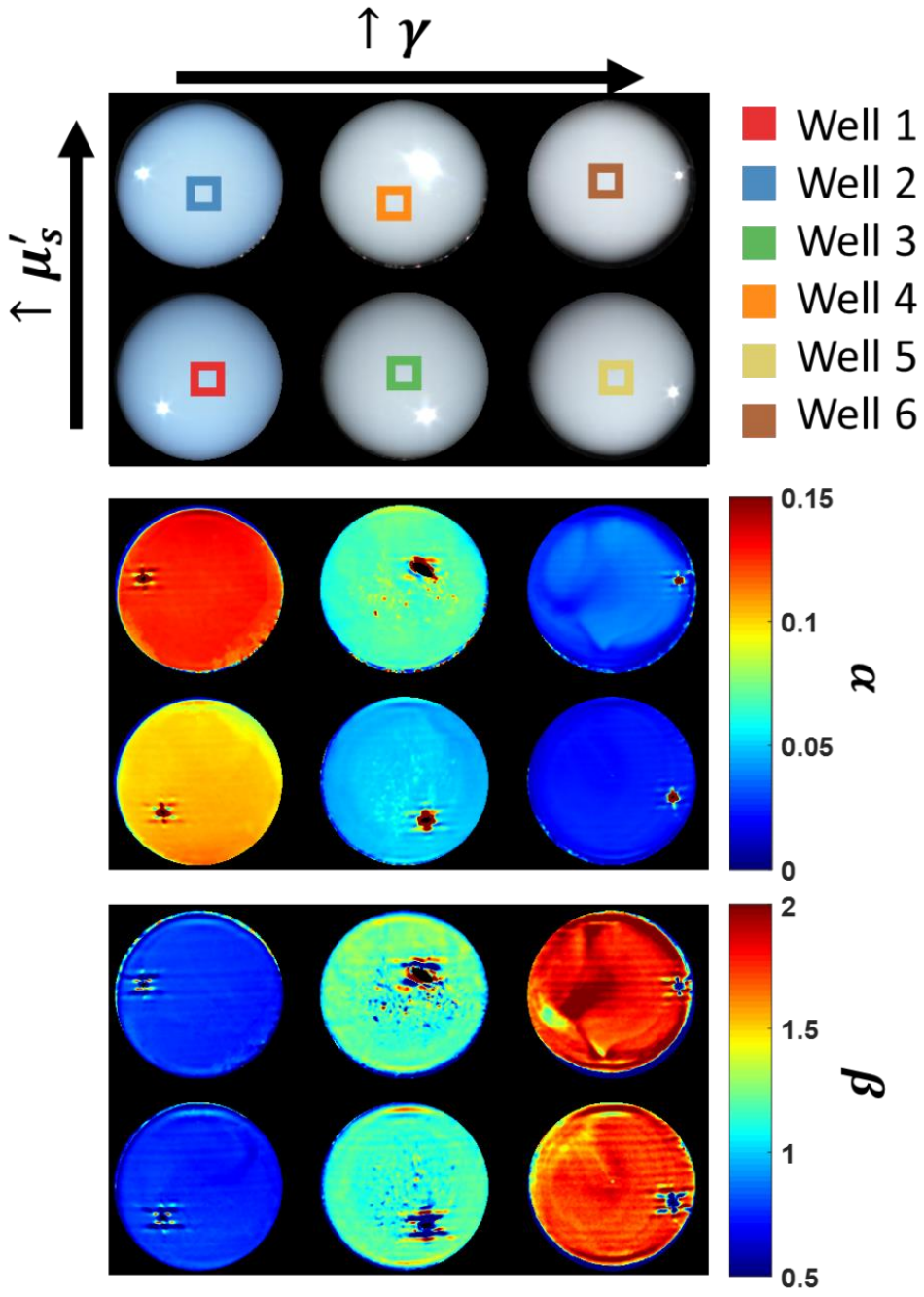

Figure 2.13: Above are raw images of the phantoms and extracted $\boldsymbol{\alpha}$ and $\boldsymbol{\beta}$ values from the power law model at $\boldsymbol{\lambda} = 530\ nm$. Although $\boldsymbol{\alpha}$ appeared to depend upon both $\boldsymbol{\mu_s}'$and $\boldsymbol{\gamma}$, the $\boldsymbol{\beta}$ term appeared to be primarily dependent upon $\boldsymbol{\gamma}$.

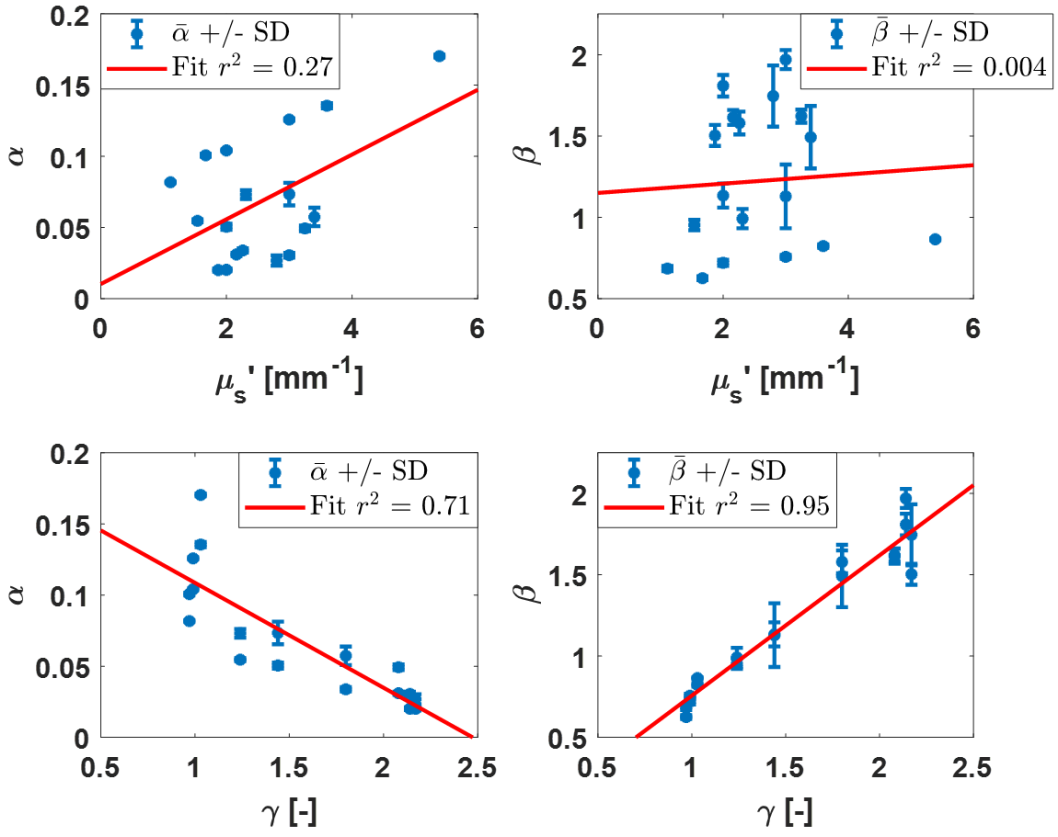

Figure 2.14: Regression trends for $\boldsymbol{\alpha}$ and $\boldsymbol{\beta}$ as a function of known $\boldsymbol{\mu_s'}$ and $\boldsymbol{\gamma}$ values indicated a strong linear correlation between $\boldsymbol{\beta}$ and $\boldsymbol{\gamma}$.

2.4.4.3 Discussion

Although the empirical power-law model had a strong linear correlation with the sub-diffuse anisotropy term, further research is necessary to reliably extract absolute measures of sub-diffuse scattering. Firstly, it was not immediately clear that reduced scattering coefficients could be recovered from the empirical power-law model coefficients. This does not preclude rapid mapping of optical properties, since methods for ultra-fast LUT have previously been discussed (Angelo, Vargas et al. 2016). However, additional modeling determined that as the reduced scattering coefficient approaches the

diffuse-regime of spatial frequencies, the power-law model begins to also depend upon reduced scattering (**Figure 2.15**). Reflectance curves were constructed from the range of the validated Kanick semi-empirical model ($\boldsymbol{\mu_s'} = [0.3 - 10\ mm^{-1}], \boldsymbol{\gamma} = [1.2 - 2.4]$) input into the semi-empirical model itself (**EQ 2.34**), and coefficients of the power law model were extracted using sampling frequencies of $\boldsymbol{f_x} = [0.5 - 1.0\ mm^{-1}]$.

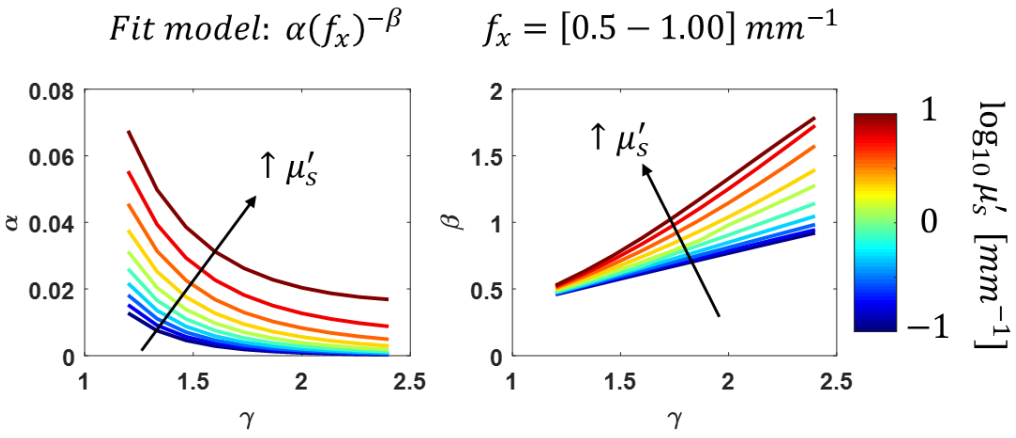

Figure 2.15: This figure indicates the theoretical dependence of empirical model terms $\boldsymbol{\alpha}$ and $\boldsymbol{\beta}$ on $\boldsymbol{\gamma}$ and $\boldsymbol{\mu_s'}$ using the Kanick semi-empirical model to produce reflectance curves. The observation of the limited experimental dependence of $\boldsymbol{\beta}$ upon $\boldsymbol{\mu_s'}$ was likely caused by the minimal variation of $\boldsymbol{\mu_s'}$ that was considered in the experiment.

The extracted $\boldsymbol{\alpha}$ values adhered to the experimental measurements in **Chapter 2**, since they were dependent upon both $\boldsymbol{\mu_s'}$ and $\boldsymbol{\gamma}$. However, the $\boldsymbol{\beta}$ value also appeared to increasingly depend upon $\boldsymbol{\mu_s'}$ because it became large relative to the spatial frequency used. Since the scattering phantoms had relatively low variance in $\boldsymbol{\mu_s'}$, this relationship was not observed. However, the relationship between $\boldsymbol{\beta}$ and $\boldsymbol{\gamma}$ was nevertheless relatively well-behaved, despite the additional apparent influence of $\boldsymbol{\mu_s'}$. Future research, as discussed in **Chapter 3**, will explore the use of reflectance curves at lower spatial frequencies to extract

$\boldsymbol{\mu_s'}$ and the use of increasingly high spatial frequencies above 1 mm^{-1} so that the empirical power-law model coefficients are only dependent upon $\boldsymbol{\gamma}$.

2.5 SUMMARY

Chapter 2 outlined the mechanisms and models describing diffuse, sub-diffuse, and ballistic light scattering in turbid media. It also introduced spatial frequency domain imaging (**SFDI**) as a means of quantifying light transport across large sample fields of view. It then demonstrated the behavior of reflectance measurements with **SFDI** within the sub-diffuse scattering regime and demonstrated that single, high-angle scattering events become increasingly important as higher spatial frequencies are used for imaging. Finally, it introduced a simplified empirical model of sub-diffuse reflectance, whose coefficients were demonstrated mathematically and experimentally to be highly sensitive to sub-diffuse scattering properties. **Chapter 3**'s objective involves applying this empirical model to detect microstructure in diseased tissues and demonstrate the feasibility of **sd-SFDI** as a rapid, wide-field screening and tumor boundary assessment tool.

Chapter 3: Analysis of tissue microstructure in skin cancers

Many sources were used for reference when writing this chapter (Gloster, Harris et al. 1996, Shriner, McCoy et al. 1998, Smeets, Kuijpers et al. 2004, Marieb and Hoehn 2007, McGuire, Norman et al. 2009, Madan, Lear et al. 2010, Kolarsick, Kolarsick et al. 2011, Leiter, Eigentler et al. 2014, Patton and Thibodeau 2014).

3.1 Motivation: Expediting Mohs Micrographic Surgery

Chapter 2 outlined methods of detecting sub-diffuse scattering properties of samples with **sd-SFDI** and described the relationship between the model coefficients and the size and concentration of scattering particles. This chapter demonstrates the application of **sd-SFDI** to mapping tissue microstructure. Microstructures, in the context of this chapter, are distilled into structures common to epithelial, stromal, and adipose tissues. Epithelium is composed of a variety of cell shapes and sizes depending upon the region; however, it can typically be characterized by a substantial number of closely-packed cells relative to stromal and adipose tissues. Stroma is characterized primarily by densely-packed, irregular connective fibers with random alignment; different support cells are found more sparsely throughout. Adipose tissues are composed mostly of adipocytes, which have large storage areas for lipids and are typically significantly larger than epithelial cells and connective fibers; they are approximately $70\ to\ 120\ \mu m$ or larger.

Histology is the study of the spatial morphology of these tissue structures in various tissue regions, such as the epidermis, dermis, and dermal appendages, such as hair follicles and sebaceous glands in the skin. Most commonly, histology involves preparing thin slices of tissue samples, applying various stains, and using bright-field microscopy to examine the morphology and organization of tissue structure. The stains provide contrast to cytoplasm, nuclei, or specific fibers and can subsequently be used to identify the type and physiological state of different tissues through trained visual examination.

Histopathology is a specific branch of histology which concerns atypical tissue structure and morphology that arises from tissue damage or disease. Although cancer

screening methodologies vary immensely between cancer types, histopathology is the universal gold standard for clinical diagnosis. Suspected tumors are biopsied and examined by specialized histopathologists who determine the presence of atypical tissue structures and morphologies (dysplasia) that indicate malignancy and pathogenesis. Both the specific tissue structure and its spatial morphology are crucial for determining a diagnosis. For example, densely-packed cells in the dermal layers of skin can signify either carcinoma or normally occurring dermal appendages (**Figure 3.1**).

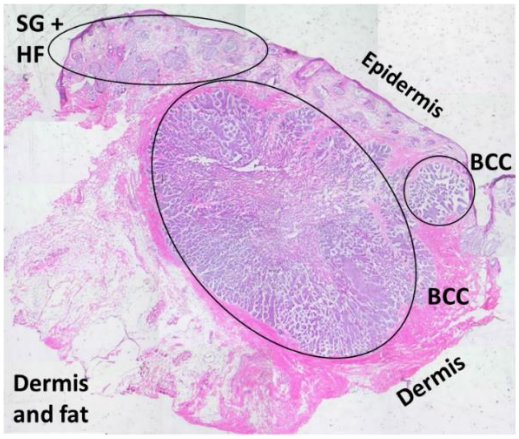

Figure 3.1: Histopathology of facial tissue presenting nodular basal cell carcinoma (**BCC**) tumor among different tissue regions. The **BCC** regions share similar cellular structure to sebaceous glands and hair follicles (**SH + HF**).

The large nodules of basal cell carcinoma (**BCC**) display similar proliferation of cells relative to the dermal appendages; therefore, other factors, including spatial morphology and local context of these structures, must also be considered for accurate diagnoses. Extensive training is necessary for dermatologists and other histopathologists to determine these diagnostic decisions.

In many instances, histopathological diagnoses do not have rigid temporal constraints; therefore, the time between resection, examination, and treatment is not invariably crucial to patient outcomes if it is limited to within a week. However, during

surgical tumor resections, in which the objective is to physically remove the entirety of a malignant tumor from the patient, histopathology introduces a significant bottleneck into a surgical workflow. In radical tumor resection techniques, histopathology is not considered during the procedure; instead, the boundary of the tumor is intentionally over-estimated. While this may provide some confidence that all malignant tumor cells are removed from the patient, it nevertheless does not achieve 100% sensitivity until after the surgery has been concluded, and the resected tumor is examined. Additionally, many tumors are found in locations where even minimal resection is problematic, such as the brain, breast, and skin of the face and head. In these cases, poor sensitivity to tumor boundaries leads to excess tissue resection that can have severe implications for patient outcomes. Although more radical resections are sometimes necessary if a cancer has metastasized, conservative tissue removal is practiced when possible. Contemporary surgical resections of tumors aim to conserve as much healthy tissue as possible while completely removing malignant tumor cells. However, tissue-conserving surgeries necessitate precise knowledge of tumor boundaries. As the gold standard for determining these boundaries, histopathology is not always well-suited to these types of surgical settings in which temporal constraints are more severe. In these cases, a more rapid method for determining tissue boundaries is necessary.

Mohs micrographic surgery (**MMS**) is a highly effective tissue-conserving surgery for resecting skin cancer lesions, particularly those on the head and face, where excessive tissue resection can produce unwanted scarring and poor overall patient outcomes. In the **MMS** workflow, a suspicious lesion is identified by a trained dermatologist based on established risk criteria. Mohs micrographic surgery is an outpatient surgical procedure that begins with topical application of an anesthetic to the suspicious lesion. The dermatologist then removes tissue from a conservative estimate of the tumor boundary based on their training and experience. The sample is delivered directly to a histopathology lab, where it is mounted and frozen in tissue-freezing media. The frozen sample can then be sectioned into thin slices of approximately $5\ to\ 20\ \mu m$ and stained, typically with hematoxylin and eosin (**H&E**), which provides contrast to cell nuclei, cytoplasm, and

connective fibers. The sample is then examined under a microscope, typically by the same dermatologist performing the procedure, to determine whether any dysplasia is present near the boundary. This entire cycle of resecting, preparing, and examining a biopsy sample is commonly referred to as an **MMS** stage. If the tumor overlaps with the boundary of the initial resection, the physician returns to the patient and resects another conservative biopsy volume. This procedure is repeated until the dysplasia is reliably contained within the resection boundary, at which point the procedure is concluded, and the wound is closed and dressed.

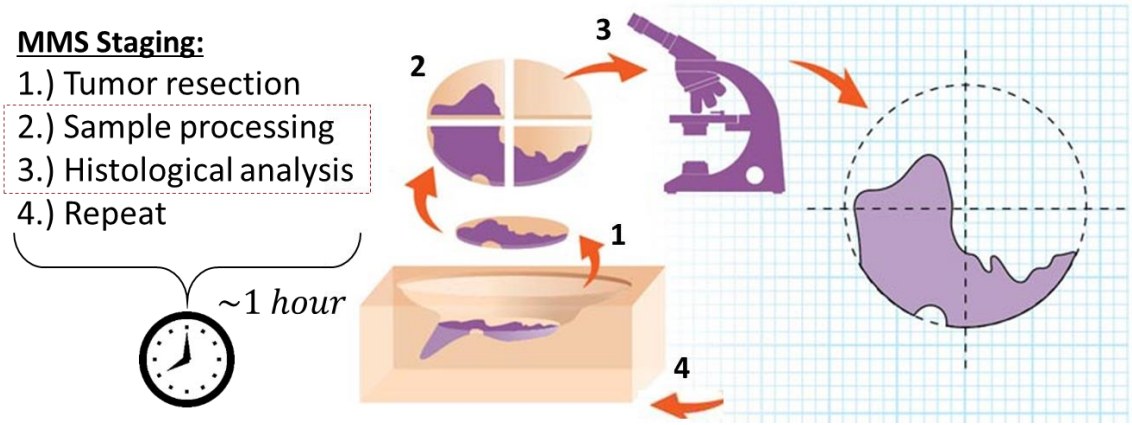

Figure 3.2: A typical MMS staging cycle, which requires about one hour for each stage, is repeated until no more tumor cells are found on the boundary of the resected tissue. Adapted from (2018).

The **MMS** workflow has yielded significant improvements in terms of long-term patient outcomes, boasting the highest cure rates for basal cell and squamous cell carcinomas; it is increasingly considered for the removal of melanoma skin cancers (Smeets, Kuijpers et al. 2004). However, the current workflow has significant room for improvement. Each **MMS** stage requires 30 to 60 minutes to perform, primarily because of the time required for physically preparing (mounting, freezing, sectioning, and staining) the resected sample. During this time, the patient remains in the surgical suite with only topical anesthetic. One study discovered that over 30% of **MMS** procedures required more

than one stage to entirely resect the tumor and noted that as many as seven passes might need to be performed (Cook and Zitelli 1998).

Overall, there is a clear necessity for mapping tissue microstructure and morphology rapidly across large ($\sim 5\ cm^2$) tumor samples to determine tumor boundaries in a surgical setting. Several existing techniques, such as confocal-scanning Raman microscopy, are highly sensitive to discriminating dysplastic tissue but are slow to image even small areas (1 hour for $1\ mm^2$); therefore, these do not improve upon the speed of histopathology in determining tumor boundaries. **Chapter 2** illustrated the ability to quantify changes in tissue microstructure rapidly over relatively large fields of view with **sd-SFDI**. Additionally, the demonstrated sensitivity of **sd-SFDI** to changes in scattering particle size distribution is highly relevant to the types of tissue structures discovered in regions of epithelium, stroma, adipose tissue, and tumors. The densely-packed structure of the stroma results in largely isotropic scattering, while the large lipid voids in adipose tissues result in diminished overall scattering. The scattering particles in epithelial cells, tumor regions, and dermal appendages tend to experience both increased scattering and increased scattering anisotropy. **sd-SFDI** provides sensitivity to these changes in scattering related to the microstructural content across relatively large fields of view; therefore, it is well-suited to complimenting the gold standard histopathological assessments of tumor boundaries.

However, current constraints on processing times limits the adequacy of existing **sd-SFDI** reflectance models to enhance **MMS** workflows in practice. This demonstration of a novel **sd-SFDI** empirical power-law model to provide sensitivity to microstructures via sub-diffuse scattering at rapid imaging (< 1 minute) and processing (< 2 minutes total) rates provides significant potential to improve the **MMS** workflow. This chapter extracts the empirical power-law model coefficients from several discarded **MMS** samples with nodular basal cell carcinoma, along with adjacent normal tissue. Histology slides were prepared for the same samples, and the average values and variations in model coefficients in regions of tumor, dermis, fat, and other tissue types were compared. Finally, the model data was used for a proof-of-concept method of segmenting potential tumor regions.

3.2 METHODS

3.2.1 MMS Samples

The samples collected for this study were approved by the IRB at The University of Texas at Austin and Seton Medical Center (Feng, Moy et al. 2018). Discarded samples from routine **MMS** procedures at the Austin Dermatologic Surgery Center were frozen and stored at $-80℃$. The top layer of the samples was sectioned and stained with **H&E**, and the remaining bulk tissue was thawed and imaged on the side adjacent to the sectioning using the **sd-SFDI** system described in **Chapter 2.4.3**. A board-certified dermatologist assisted in delineating regions of each sample and used the histology images as a guide; they delineated the primary tumor regions, dermis, sebaceous glands and hair follicles, epidermis, and fat. Two cancerous samples were examined in this study; each presented nodular basal cell carcinoma (**BCC**) tumors, along with one additional "clear" sample of normal tissue. One nodular **BCC** sample was resected from a patient's cheek, one adjacent normal sample was resected from the check of the same patient, and one nodular **BCC** sample was resected from the nose of a separate patient.

3.2.2 sd-SFDI Imaging and Processing

The samples were placed in baths of phosphate-buffered saline (PBS) at room temperature for thirty minutes prior to imaging. They were then secured between glass slides and mounted for sd-SFDI imaging at $\boldsymbol{f_x} = [0.0 - 1.2\, mm^{-1}]$ in $0.05\, mm^{-1}$ increments and at wavelengths of $\boldsymbol{\lambda} = [450\, nm, 530\, nm, 620\, nm]$. Only the spatial frequencies $\boldsymbol{f_x} = [0.5 - 1.0\, mm^{-1}]$ were considered for processing. The sample reflectance was normalized to the previously-described titanium dioxide reflectance standard (**Appendix A**); no other filtering was applied to the reflectance maps prior to or after fitting them to the empirical power-law model. Small **ROI** ($25x25\ pixels$) in areas demarcated by the expert dermatologist were used to compare distributions of model coefficients between known tissue regions. For this assessment, only the $\boldsymbol{\lambda} = 450\, nm$

wavelength was considered in both the coefficient mapping in **Figure 3.3** and the regional coefficient comparisons in **Figure 3.4**.

3.3 RESULTS

3.3.1 Sub-diffuse Empirical Model Coefficient Maps and Histology Comparison

Figure 3.3 indicates the results for three representative samples. The raw RGB images also display the color-coded **ROI** used for distribution comparisons. Maps of the $\boldsymbol{\alpha}$ model coefficient appeared to be sensitive to extracellular matrix constituents, as demonstrated by the fibrous structures that were highlighted across each sample. Regions demarcated by histopathology as dermis had higher values of $\boldsymbol{\alpha}$. The $\boldsymbol{\beta}$ model coefficient correlated significantly with the regions demarcated by histopathology as either tumor regions or sebaceous glands and hair follicles. This is consistent with the expected microstructural changes in these regions, which typically present higher nuclei-to-cytoplasm ratios along with more densely-packed nuclei (Sexton, Jones et al. 1990, Wax, Yang et al. 2002). As **Chapter 2** demonstrated, $\boldsymbol{\beta}$ is positively correlated with the sub-diffuse scattering parameter $\boldsymbol{\gamma}$, which indicates a decrease in the average size of the scattering particles (Bevilacqua and Depeursinge 1999, Chamot, Migacheva et al. 2010). Additionally, this associated increase in the $\boldsymbol{\gamma}$ parameter in tumor regions is consistent with previous research (McClatchy III, Hoopes et al. 2017, McClatchy, Rizzo et al. 2018). Demarcated regions of fatty-dermis had low values of both $\boldsymbol{\alpha}$ and $\boldsymbol{\beta}$. This result was also consistent with expectations, since subcutaneous adipose regions have previously been proven to exhibit more limited overall scattering (Boas, Pitris et al. 2016). The epidermal regions had $\boldsymbol{\alpha}$ values comparable to the epidermal and sebaceous gland and hair follicle regions; however, they had significantly lower $\boldsymbol{\beta}$ values, which was unexpected for areas of epidermis that are typically composed of more densely-packed cells and less stroma (Boas, Pitris et al. 2016). However, this can potentially be explained by the low overall signal at the thin edges of the tissue.

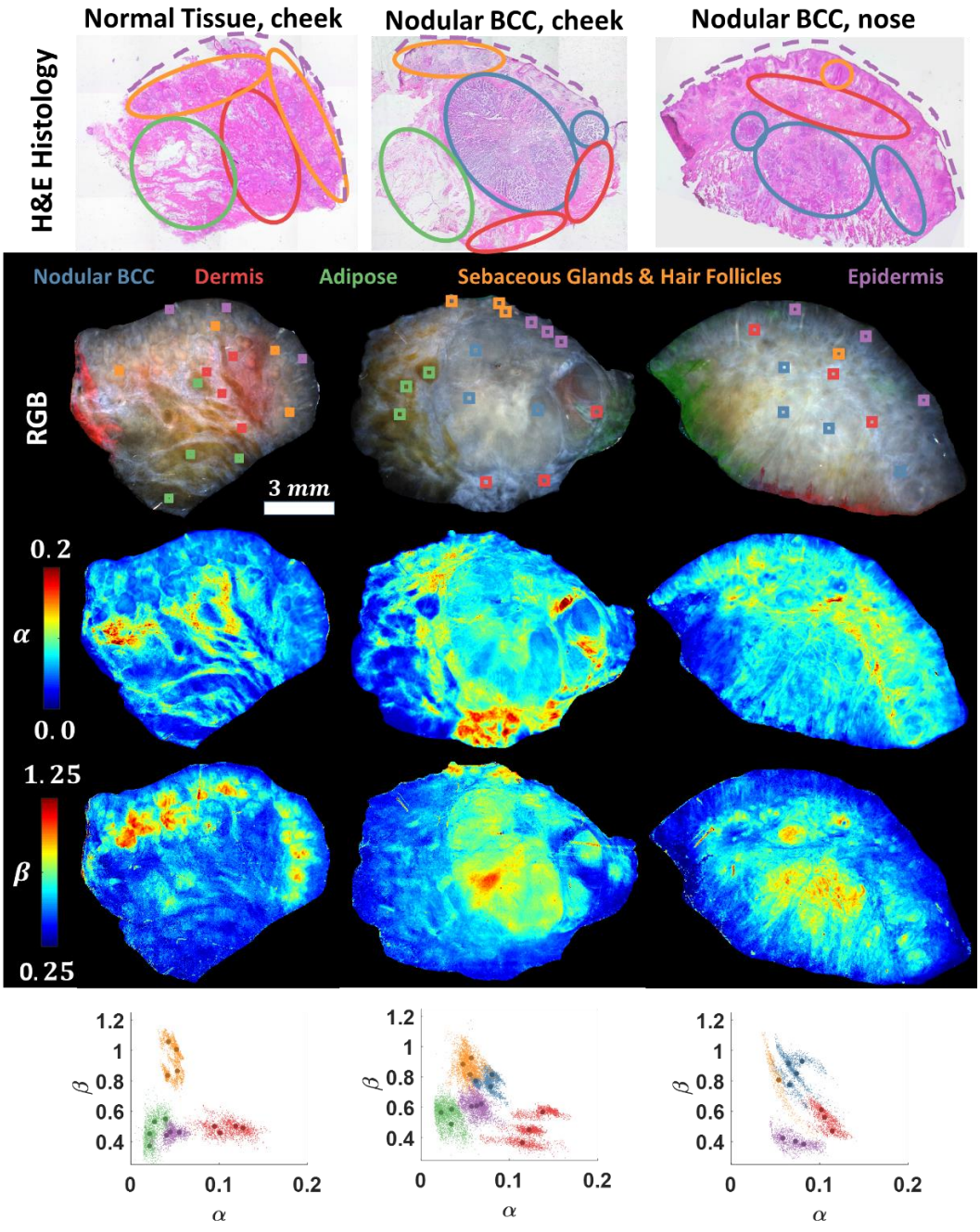

Figure 3.3: Above are representative samples of nodular BCC tumors and adjacent normal tissue from the facial regions of two different patients. Extracted empirical model coefficients demonstrated repeatable sensitivity to tissue regions that aligned well with those demarcated by expert histopathologists.

3.3.2 Morphological Feature Comparison

Figure 3.4 presents additional comparisons between all samples from the study. The trends between the samples appeared to be highly consistent: Dermis tissue had high $\boldsymbol{\alpha}$ values associated qualitatively with connective tissue components; BCC tumor regions and sebaceous glands and hair follicles had markedly increased $\boldsymbol{\beta}$ values associated with small, densely-packed scatterers; fatty regions had reduced $\boldsymbol{\alpha}$ and $\boldsymbol{\beta}$ coefficients that were indicative of lipids. Epidermal tissue was more difficult to discriminate from the individual model components, since it had moderate levels of both $\boldsymbol{\alpha}$ and $\boldsymbol{\beta}$; however, when both of the coefficients were considered together, it appeared to also have a unique cluster region.

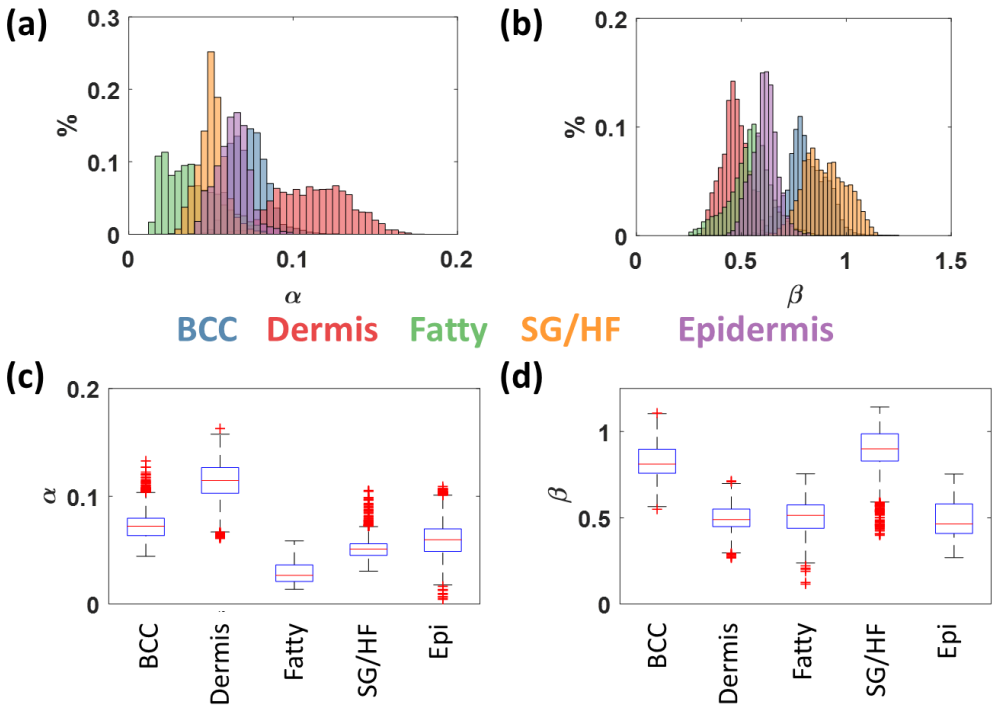

Figure 3.4: These graphs illustrate coefficient variations across different tissue regions compiled for all five nodular BCC tumor samples and the adjacent normal tissue sample; this demonstrates clear trends in different tissue regions.

3.4 DISCUSSION

3.4.1 Proof-of-concept: Tumor boundary guidance

The **sd-SFDI** techniques outlined in **Chapter 2** demonstrated the wide-field sensitivity of the empirical power-law model to map tissue microstructures that correlated well with histopathological examinations of nodular basal cell carcinoma samples. Regions of high cell-proliferation, including tumor regions and dermal appendages, were demonstrated to be identifiable based on their sub-diffuse scattering properties; they provided the first demonstration of **sd-SFDI** to image skin cancer tissues. However, rather than an absolute diagnostic tool, **sd-SFDI** maps of tissue microstructure would most likely be relevant as a tool for more rapid assessment of tumor boundaries. Wirth et al. outline the use of fluorescent **SFDI** for intraoperative tumor margin assessment during surgical resections and note that uncertain volumetric sampling (and therefore, spatial frequency selection) of the system may impact the interpretation of results when the sample is not homogeneous (Wirth, Sibai et al. 2018). Additionally, the context of the local morphology of the microstructure is crucial even for the histopathological assessment of tumor regions. As demonstrated in the results, dermal appendages displayed similar sub-diffuse scattering properties relative to the tumor regions; differentiating between them requires additional morphological context. Therefore, **sd-SFDI** will likely find its most relevant use as a guidance tool to limit the areas to search for potential cancers in large tissue samples. One proposed use involves pairing **sd-SFDI** with a technique which has higher discriminatory capability (such as Raman confocal microscopy) but poor imaging speeds over large fields of view.

To demonstrate this potential use, a proof-of-concept image segmentation was performed based on the statistical clustering regions extracted from the regional distributions of $\boldsymbol{\alpha}$ and $\boldsymbol{\beta}$ coefficients. A quadratic discriminant analysis model was generated using two groups; one contained measures of $\boldsymbol{\alpha}$ and $\boldsymbol{\beta}$ coefficients in the nodular BCC and sebaceous gland and hair follicle regions, and one group contained the measures for the dermis, epidermis, and fatty-dermis regions. **Figure 3.5** displays the clustering

model applied to the spatial $\boldsymbol{\alpha}$ and $\boldsymbol{\beta}$ values overlaid on the RGB images of the samples. The highlighted areas appeared to correspond with the histology images for the samples. This segmentation provides a significant reduction in risk areas ($69 - 84\%$) relative to the total sample area, which potentially permit the use of complimentary techniques with slower imaging speeds but higher discriminatory power within the Mohs workflow. These areas could be further reduced by dermatologists who can visually reject features that are clearly non-malignant morphological features.

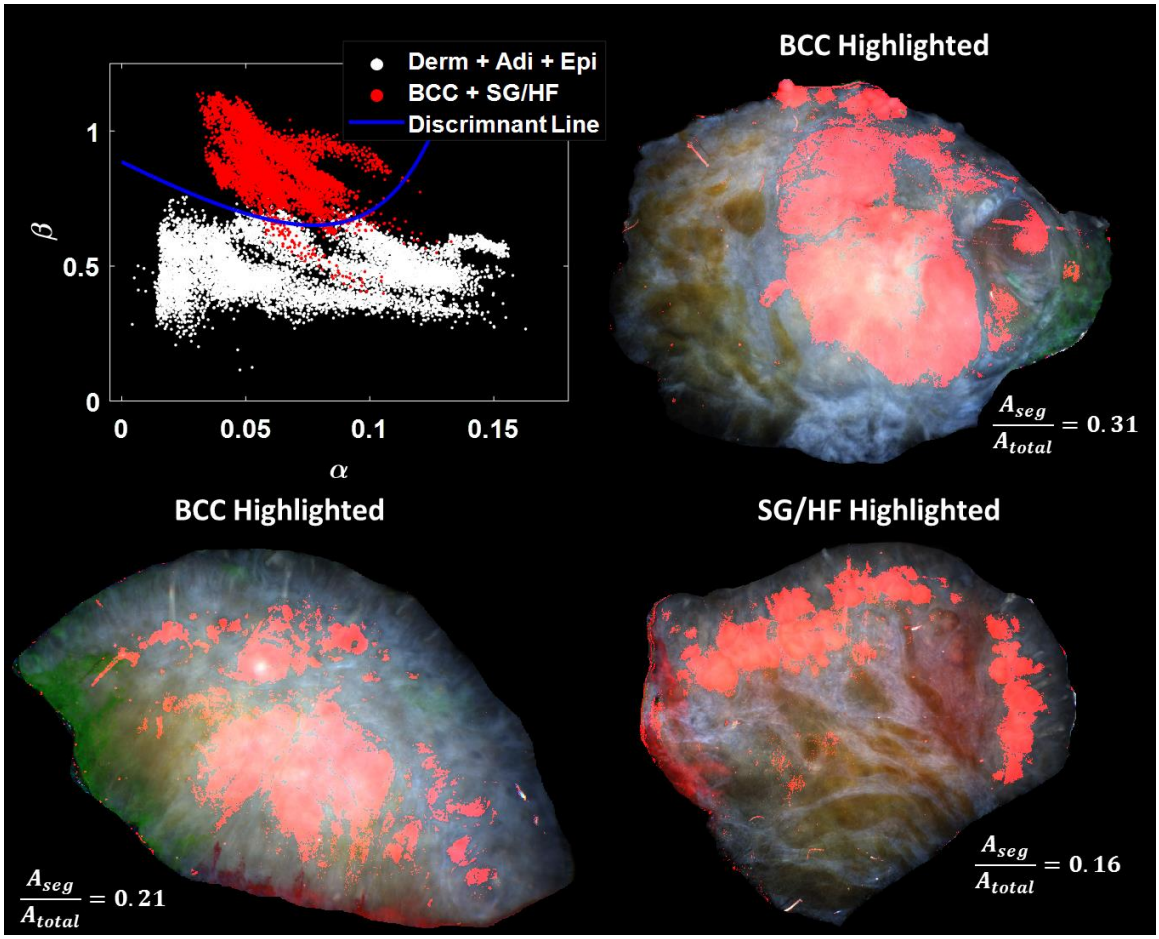

Figure 3.5: The discriminant analysis model uses clustering groups of $\boldsymbol{\alpha}$ and $\boldsymbol{\beta}$ to highlight regions that correlate with increased cell proliferation (BCC tumor and sebaceous glands and hair follicles).

Further research with a larger total sample size of tissues should be conducted to provide statistical confidence of variations in optical properties from similar tissue types discovered between different patients. A second set of 20 total samples from a related study displaying nodular BCC, superficial BCC, and normal tissue with and without inflammation has been reserved for imaging with **sd-SFDI**.

3.4.2 Improvements to the empirical model

Several improvements can be made in terms of studying sub-diffuse light scattering using our proposed empirical model. First, the existing semi-empirical model from Kanick et al. could not be applied due to issues in finding reliable system model coefficients. Additionally, the titanium dioxide reference phantom (**Appendix A**) was not appropriate for use as a reference phantom with this model, since the higher-order scattering properties of the highly dispersed size distribution were beyond the semi-empirical model range. Therefore, due to limitations in terms of the range and system variabilities, future research should utilize Monte Carlo modeling and incorporate sub-diffuse scattering as a reference technique for extracting the sub-diffuse properties of samples. This would allow for a more thorough comparison and testing of limitations of the proposed empirical model, particularly in terms of determining whether it is equivalent to the Kanick semi-empirical model under certain conditions.

Additionally, the results in **Chapter 2** indicate that while coefficients that were related to $\boldsymbol{\mu_s'}$ and the $\boldsymbol{\gamma}$ parameter could empirically be extracted, the contributions from each were not entirely decoupled. Subsequently, it was determined that $\boldsymbol{\mu_s'}$ could be extracted rapidly from measurements within the diffuse ranges of spatial frequencies; two strategies were developed to diminish the dependence of the model coefficients upon $\boldsymbol{\mu_s'}$. The first involved normalizing the spatial frequency to the extracted reduced scattering coefficient prior to fitting to the empirical model. While this inherently requires a model to extract reduced scattering coefficients, this additional processing requirement can nevertheless fulfill the goal of improving MMS worktimes, since maps of diffuse scattering

properties have previously been extracted rapidly over large fields of view (Angelo, Vargas et al. 2016). When this normalization was performed prior to fitting the power law model to the Kanick semi-empirical model, the impact on the relationship between the $\boldsymbol{\beta}$ model coefficient and the $\boldsymbol{\gamma}$ parameter was relatively minimal (**Figure 3.7**). Surprisingly, the $\boldsymbol{\alpha}$ model coefficient became almost entirely dependent upon $\boldsymbol{\gamma}$, except at high $\boldsymbol{\mu_s'}$ values relative to the spatial frequency.

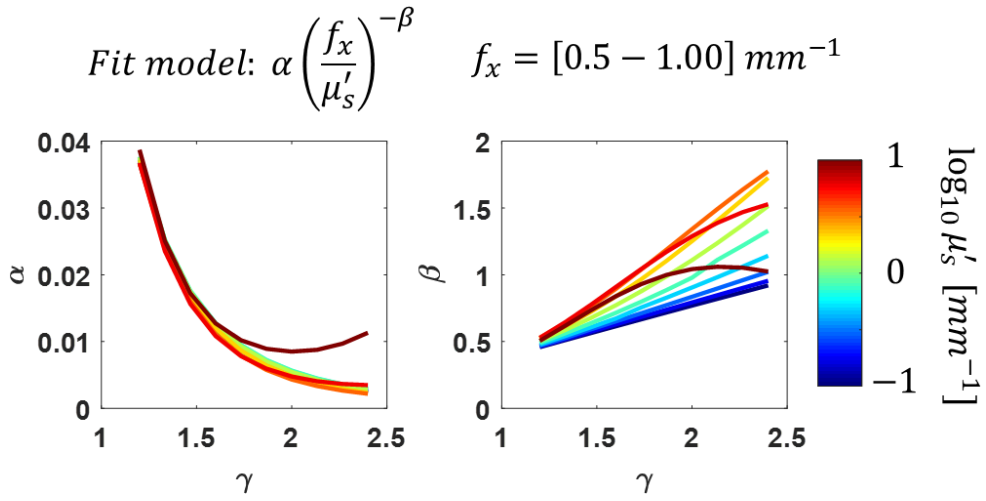

Figure 3.6: By normalizing the spatial frequency ($\boldsymbol{f_x}$) to the reduced scattering ($\boldsymbol{\mu_s'}$) in the empirical model before fitting, the $\boldsymbol{\beta}$ coefficient dependence upon $\boldsymbol{\mu_s'}$ remained relatively unchanged, but the $\boldsymbol{\alpha}$ coefficient became nearly entirely described by $\boldsymbol{\gamma}$ alone.

The second strategy to mitigate the reduced scattering impact on the relationship between the model coefficients and the $\boldsymbol{\gamma}$ parameter involved increasing the relative spatial frequency. By increasing the spatial frequency range to $\boldsymbol{f_x} = [1.0 - 2.0\ mm^{-1}]$, the variation in the $\boldsymbol{\alpha}$ model coefficient entirely disappeared, and the relationship with the $\boldsymbol{\gamma}$ parameter appeared to be defined by a power law itself (**Figure 3.8**).

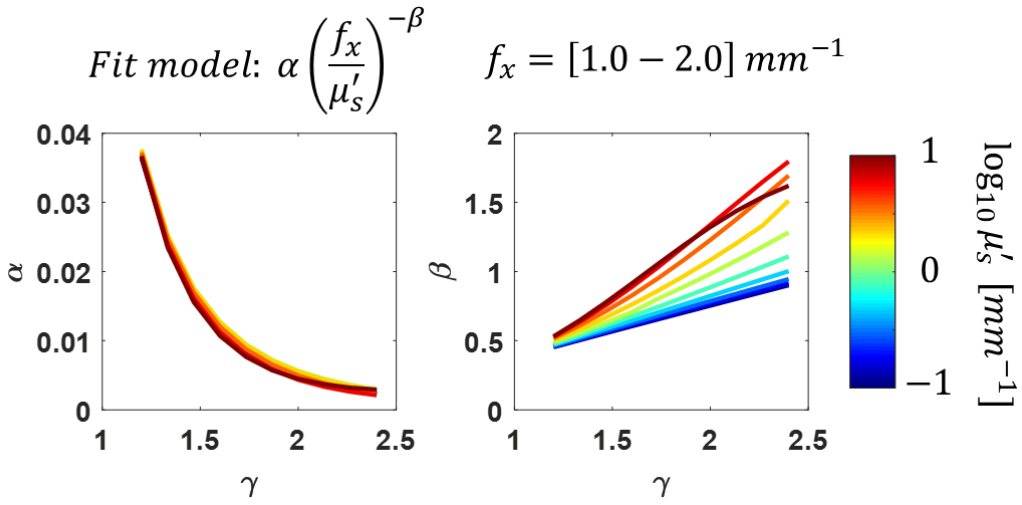

Figure 3.7: Increasing the spatial frequency range ($\boldsymbol{f_x}$) considered and normalizing $\boldsymbol{f_x}$ to reduced scattering ($\boldsymbol{\mu_s'}$) prior to fitting caused $\boldsymbol{\alpha}$ to display a power-law dependence on $\boldsymbol{\gamma}$.

This result suggests that when the spatial frequency used for imaging is high relative to the reduced scattering coefficient, the Kanick semi-empirical model in **EQ 2.34** diminishes to a simplified power-law model. Although this must be validated to produce more precise results (preferably applying a sub-diffuse Monte Carlo model), this potentially increases the robustness for the method used to rapidly extract sub-diffuse optical properties by utilizing higher spatial frequencies. Two primary considerations are important in relation to imaging at high spatial frequencies. The first is decreased signal level and increased sensitivity to imaging artifacts, which may be mitigated by using dynamic imaging exposures that increase along with spatial frequency. Additionally, the necessity for increased spatial frequency decreases the imaging field of view of SFDI systems using digital micromirror devices for pattern projection. However, since these devices have steadily improved in terms of pixel-mirror density in recent years, this requirement for super-high spatial frequency ($\boldsymbol{f_x} > 1\, mm^{-1}$) pattern projection has become more tractable.

Chapter 4: Modeling and measuring polarized light scattering from tissues

4.1 Polarized Light

Polarization describes the orientation of the electric field component of an electromagnetic wave. The electric and magnetic fields of light oscillate perpendicularly to one another and are both perpendicular in relation to the direction of propagation. **Figure 4.1** illustrates a polarized light wave propagating in the Z-direction. In this example, the electric field amplitude (red) is confined to the YZ-plane, which indicates linearly polarized light with a vertical orientation. The magnetic field can be largely ignored, since Maxwell's equations dictate that it will invariably be perpendicular to the electric field.

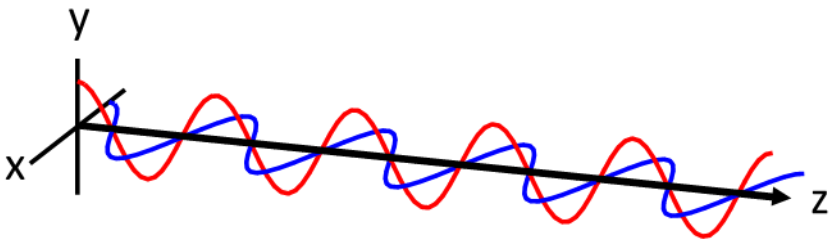

Figure 4.1: A diagram of an electromagnetic wave traveling in the Z-direction with the magnetic field (blue) oscillating in the XZ-plane and the electric field (red) oscillating in the YZ-plane, which indicates vertical linear polarization.

The Mie solution to light scattering from spheres (**Chapter 2**) demonstrates that polarization is largely irrelevant to the orientation of spherical particles due to the symmetry of the particle geometry. However, if the particle geometry is non-symmetrical, such as in the case of cylindrical particles such as collagen fibers, the relative orientations of the light polarization and the scattering particle will exert a significantly greater influence on the scattering response. This chapter discusses the formalism used to

mathematically describe polarized light, the systems used to generate and detect polarized light, and the Mie solutions to polarized light-scattering from single cylindrical particles. This model is extended to describe populations of tissue fibers with varying degrees of alignment; the model is then validated through experimental measurements of fiber phantoms. The ultimate objective of this chapter is to establish and experimentally validate the relationship between polarization-dependent light-scattering and absolute measures of fiber alignment.

4.2 POLARIMETRY

Polarimetry generally refers to the study of relationships between polarized light and an optically-active medium. Optically active media cause the polarization of light to change as light propagates through it. These interactions can polarize, depolarize, or otherwise disturb the initial polarization of light. The following sources were used as reference in this section: (Goldstein 2003, DiMarzio 2011).

4.2.1 Stokes Vectors

The Stokes vector is a set of four parameters which fully describe the polarization state of an electromagnetic wave:

$$\vec{S}_{in} = \begin{pmatrix} \mathrm{I} \\ Q \\ U \\ \mathrm{V} \end{pmatrix} \tag{4.1}$$

The parameter $\boldsymbol{I}$ describes the total intensity of light, and the entire vector is often normalized so that $\boldsymbol{I} = 1$. $\boldsymbol{Q}$ describes the amount of linearly polarized light in the horizontal and vertical vectors which are orthogonal to the direction of propagation; $\boldsymbol{U}$ describes the linearly-polarized light in the $+/-45°$ vectors. Circularly-polarized light is described by $\boldsymbol{V}$; positive values indicate "right-handed" (counter-clockwise) circularly-polarized light, and negative values indicate "left-handed" (clockwise) circularly-polarized

light. The $\boldsymbol{Q}$, $\boldsymbol{U}$, and $\boldsymbol{V}$ Stokes parameters each have a range of $[-1, 1]$ but, when combined. cannot exceed the total amplitude of light, such that $\boldsymbol{I}^2 \geq \boldsymbol{Q}^2 + \boldsymbol{U}^2 + \boldsymbol{V}^2$. **Figure 4.2** presents several examples of the orientation of the electric field for different Stokes vectors. These use the same coordinate system displayed for a polarized electromagnetic wave in **Figure 4.1**.

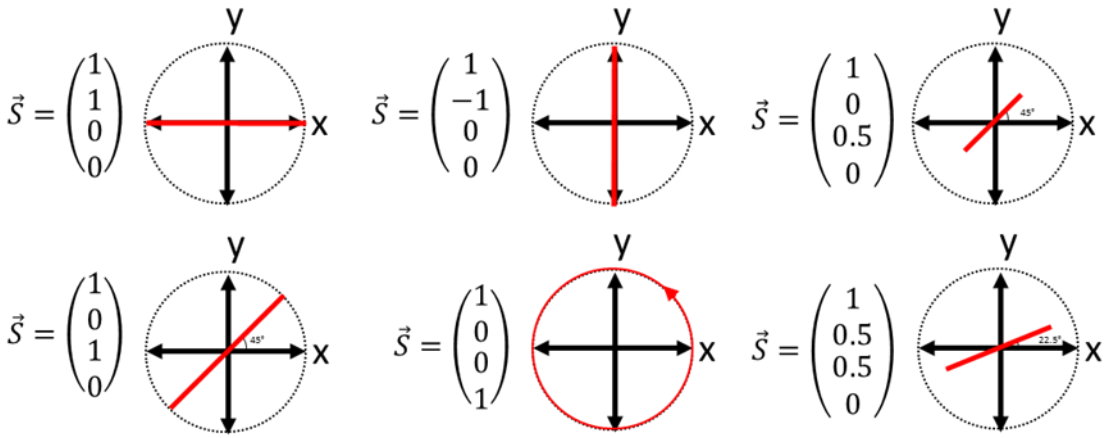

Figure 4.2: This figure depicts polarization states for different Stokes vectors, including horizontal-linear polarization **(a)**, 45˚-linear polarization **(b)**, vertical-linear polarization **(c)**, right-hand-circular polarization **(d)**, 45˚-linear partial-polarization **(e)**, and mixed-linear partial-polarization **(f)**.

Every individual photon possesses a distinct polarization state. Groups of many photons, however, can also be partially polarized or randomly polarized if the orientations of the individual photons are not identical. The degree of polarization ($\boldsymbol{DoP}$) describes the proportion of photons with coherent polarization:

$$DoP = \frac{Q^2 + U^2 + V^2}{I^2} \tag{4.2}$$

A $\boldsymbol{DoP}$ of 1 indicates that the orientation of the electric fields of all individual photons are synchronized (coherent). Conversely, a $\boldsymbol{DoP}$ of 0 describes entirely random (incoherent) polarization, in which the vector sum of the electric field orientations for each photon cancels out. Notably, $\boldsymbol{DoP} = 0$ does not imply that the amplitude of the electromagnetic wave experiences destructive interference; rather, it merely indicates that the orientation of the light is random.

4.2.2 Mueller Matrices

As an electromagnetic wave propagates through free space, its polarization state remains constant; therefore the Stokes vector does not change. Mueller matrices mathematically describe changes to the Stokes parameters that result from light propagating through an optically-active medium. A Mueller matrix consists of 16 total elements:

$$M = \begin{bmatrix} M_{11} & M_{12} & M_{13} & M_{14} \\ M_{21} & M_{22} & M_{23} & M_{24} \\ M_{31} & M_{32} & M_{33} & M_{34} \\ M_{41} & M_{42} & M_{43} & M_{44} \end{bmatrix} \quad \textbf{(4.3)}$$

A Mueller matrix can be used to represent any physical medium that is optically-active, including both optical components in an imaging system (such as polarizers or mirrors) and unknown samples. To determine the resultant polarization of light, the Mueller matrix is multiplied by the initial Stokes vector, as follows:

$$\vec{S}_{out} = M\vec{S}_{in} \quad \textbf{(4.4)}$$

This operation is associative (though not commutative) for any number of media which the light encounters. For example, in the system depicted in **Figure 4.3**, the resultant Stokes vector $\boldsymbol{S}_{out}$ can be calculated by multiplying the Mueller matrices ($\boldsymbol{M_n}$) and initial Stokes vector$\boldsymbol{S}_{in}$, in reverse order in relation to how the light encounters each object. This

formalism is used to describe the polarized light-imaging system and to derive the idealized Mueller matrices for fibrous samples using the Mie solution.

Figure 4.3: The diagram above depicts polarized light propagating through three distinct media, each described by their own Mueller matrix. The output polarization state of light can be calculated if the input polarization state and Mueller matrices for each element are known (**EQ 4.5**):

$$\vec{S}_{out} = M_3 M_2 M_1 \vec{S}_{in} \tag{4.5}$$

4.2.3 Common Polarimetric Optical Properties

Although the Mueller matrix elements can each be considered individually to characterize optically active media, it is common to quantify them in terms of diattenuation, retardance, and depolarization. Diattenuation indicates the polarization-dependent transmittance of light within media, and retardance resembles polarization-dependent phase change in a medium. In diattenuation, total ***DoP*** remains constant or increases, while in retardance, total ***DoP*** is preserved. Decreasing ***DoP*** is characterized by depolarization. The Lu-Chipman decomposition method allows a Mueller matrix to be separated into these three distinct components. These metrics can be further refined into measures of biattenuance and birefringence, which describe optical activity in bulk media for a given differential unit depth. However, although these relative measures of polarimetric properties often arise from underlying sample structures, the measurements alone do not imply the origin or absolute value of the structural anisotropy. For example, similar

measures of birefringence may be discovered from ordered crystalline structures and anisotropic light scattering by microscopic fibers. To infer relative structural anisotropy from absolute optical anisotropy measurements, some degree of *a priori* knowledge of the structure is necessary.

4.2.4 Polarized Light Imaging of Biological Tissues

A substantial volume of research concerns polarized light imaging and Mueller matrix polarimetry of biological tissues (Jacques, Roman et al. 2000, Jacques, Ramella-Roman et al. 2002, Jacques and Ramella-Roman 2004, Ramella-Roman, Lee et al. 2004, Kemp, Zaatari et al. 2005, Jacques and Pogue 2008, Ghosh and Vitkin 2011, Qi and Elson 2017). These techniques allow for the characterization of the polarimetric properties of tissues and have been applied to relate polarization-dependent optical properties to various underlying structural and physiological features. In particular, collagen fibers are a significant source of optical anisotropy in tissue, and are also pivotal in terms of mechanical tissue function. Tendons (Whittaker and Canham 1991), heart valve leaflets (Tower, Neidert et al. 2002, Yang, Lesicko et al. 2015), the cervix (Chue-Sang, Holness et al. 2018), the cornea (Pircher, Götzinger et al. 2004, Mega, Robitaille et al. 2012), skin (De Boer, Srinivas et al. 1999), and tumor lesions (He, Sun et al. 2014) are among the biological tissues imaged with polarized light to investigate collagen fiber anisotropy in relation to physiological conditions.

Notably, polarized light imaging can be performed in wide-field with readily adjustable fields-of-view; this enables both small and large sample areas to be imaged rapidly near or above video-rate (Jacques, Ramella-Roman et al. 2002, Kuhn and Poenie 2002). Additionally, it can be readily paired with many coherent and incoherent imaging techniques, such as bright-field microscopy, optical coherence tomography, harmonic generation imaging, and spatial frequency domain imaging, among others (De Boer, Milner et al. 1997, Kuhn and Poenie 2002, Stoller, Reiser et al. 2002, Yang, Lesicko et al. 2015).

4.2.5 Current Needs: Depth Gating and Absolute Measurements of Fiber Structure

Polarization imaging systems impose two inherent challenges. Firstly, these techniques primarily provide polarimetric properties, such as those described in **Chapter 4.2.3**, as measures of tissue structure (Chenault and Chipman 1993, Lu and Chipman 1996, Ghosh, Vitkin et al. 2008, Ghosh, Wood et al. 2009, Wood, Ghosh et al. 2009, Liao, Jiang et al. 2010, Sun, He et al. 2014). While these metrics are useful for relative comparisons of structural anisotropy, absolute measures of fiber orientation distributions are necessary to improve the accuracy of modeling soft-tissue mechanical behavior (Tower, Neidert et al. 2002, Sacks 2003). Extracting absolute measures of fiber alignment using these techniques typically requires precise *a priori* knowledge of fiber size and optical properties at each image point. As a result, small changes in the fiber size may influence the interpretation of fiber alignment.

Secondly, these systems do not distinguish distinct tissue layers within samples and are instead bulk measurements through the thickness of the sample. Transmissive polarization systems measure average optical anisotropy through the entire sample thickness, while reflective polarization systems average it through a sampling depth up to several millimeters deep in biological tissues (Guo, Wood et al. 2007, Guo, Wood et al. 2008). In both cases, the multiple-scattering of the light through thick, turbid samples precipitates the overall depolarization of the optical signal, which results in changes in measured optical anisotropy as a function of sampling depth and potential misinterpretations of multi-layered structural anisotropy (Ghosh, Gupta et al. 2006). Serial sectioning and imaging are feasible but also limit measurements of fiber microstructures to experimental endpoints. These issues demonstrate the necessity of limiting optical anisotropy measurements in biological tissues to thin layers ($< 500\mu m$) without physical sectioning. The necessity of gating of imaging depth is particularly relevant to heart valve leaflets, which have distinct layers several hundred microns thick, which each possess unique fiber structures (Misfeld and Sievers 2007, Stella and Sacks 2007).

4.3 POLARIZED SPATIAL FREQUENCY DOMAIN IMAGING

This section first describes the instrumentation for the polarized spatial frequency domain imaging (**pSFDI**) system. Polarized light imaging provides sensitivity to fiber structure, while structured illumination (discussed in **Chapter 2)** enables control of the effective imaging depth to distinguish tissue layers around several hundred microns thick. This section then derives the Mueller matrix formalism used to mathematically describe the idealized polarization system and outlines the calibration and data-processing techniques used to ensure repeatable measurements and rapid image analysis.

4.3.1 Instrumentation

The **pSFDI** system (**Figure 4.4**) is composed of three primary components, including pattern projection, polarization modulation, and image detection. Spatial frequency patterns were projected using a DLP Lightcrafter Evaluation Module digital micro-mirror device (Texas Instruments, Dallas TX). The projected pattern was delivered through a bandpass filter to produce light with a center wavelength of $529\,nm$ and a measured spectral full-width half-maximum of less than $15\,nm$. The spectrally-filtered pattern was folded with a right-angle mirror and projected onto the sample through a linear polarizer mounted on a Zaber high-speed rotational stage with a $2''$ aperture (Zaber Technologies Inc., Vancouver, BC, Canada). The stage rotated the linear polarizer through $180°$, and imaging was conducted at $9°$ increments for a total of 20 measurements. A CMOS camera (acA1300-60gm, Basler AG, Ahrensburg, Germany) captured an image of each projected spatial pattern using the same rotating linear polarizer aperture at each polarizer orientation. The image resolution was $1280x1024$ pixels, and the field of view was approximately $24\,mm\,x\,18\,mm$, although this could be increased or decreased for desired applications by changing the working distance of the sample. The imaging system used a $f/1.4$ variable focus imaging lens (calculated collection half-angle of $\boldsymbol{\psi} = 15°$), and the camera had an exposure time of $20\,ms$. The entire system was controlled through

a custom LabVIEW VI (National Instruments, Austin TX), and it acquired the entire wide-field image set in under 5 seconds.

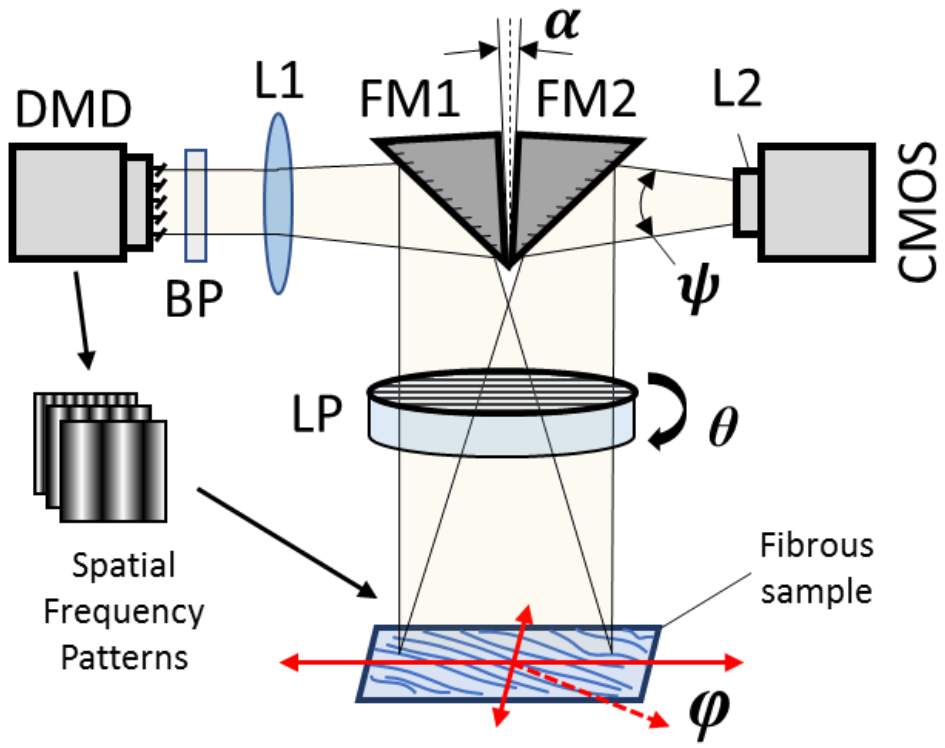

Figure 4.4: Above is a schematic of a combined polarized light spatial frequency domain (**pSFDI**) system, which consists of a digital micromirror device (**DMD**), fold mirrors (**FM1** and **FM2**), linear polarizer (**LP**), projection and imaging lenses (**L1** and **L2**), bandpass filter (**BP**), and **CMOS** camera. The fibers in the sample are primarily distributed angularly in the XY-plane along an angle of $\boldsymbol{\varphi}$, and the **LP** rotates in the same plane at angle $\boldsymbol{\theta}$. A small angle of $\boldsymbol{\alpha} \approx 10°$ between the fold mirrors allows the projection and imaging fields of view to align. The working distance from the sample is adjustable from $1\ to\ 20\ cm$ from the **LP** and can be adjusted to alter the system field-of-view.

4.3.2 Chenault and Chipman Model Derivation

The basic mathematical form for this system has been derived from an existing model developed by Chenault and Chipman, who described the Mueller matrix representation of the rotating linear polarizer system, as outlined in the instrumentation section (Chenault and Chipman 1993). This model is useful because of the relative simplicity of the required instrumentation, the limited number of polarization states necessary to satisfy the sampling criteria, and the ability to linearize the model for rapid fitting. The basic Mueller matrix representation of the system in is expressed in **EQ 4.6**:

$$\vec{S}_{out} = \tau_{sys} M_p R_p\big(-(\theta \pm \varphi)\big) M_s R_p\big((\theta \pm \varphi)\big) M_p \vec{S}_{in} \qquad \textbf{(4.6)}$$

$\boldsymbol{M_p}$ and $\boldsymbol{R_p}$ represent the Mueller matrix and rotational matrix for a linear polarizer, and $\boldsymbol{M_s}$ is the sample Mueller matrix. **Appendix C** presents an extended description of these Mueller matrices. Non-polarization dependent system efficiencies are indicated by $\boldsymbol{\tau_{sys}}$, which is omitted from this point forward, since it only contributes to linear scaling of the final signal that is accounted for through calibration. The angle $\boldsymbol{\theta}$ describes the orientation of the rotating polarizer in the system, and the sample orientation $\boldsymbol{\varphi}$ is the major axis of optical anisotropy in the sample (i.e., the orientation in which the reflected light intensity is maximized). This arrangement requires a minimum of eight polarizer orientations to adequately sample the signal, and the response is symmetrical over a period of $[-90°, 90°]$. Solving this system results in **EQ 4.7**:

$$I(\theta) = a_0 + a_2 \cos\big(2(\theta \pm \varphi)\big) + a_4 \cos\big(4(\theta \pm \varphi)\big) \qquad \textbf{(4.7)}$$

The coefficients $\boldsymbol{a_0}$, $\boldsymbol{a_2}$, and $\boldsymbol{a_4}$ describe the amplitude of the signal response as a function of the polarizer angle. These are related to the Mueller matrix elements of the sample through the following equations:

$$a_0 = (3M_{11} + M_{33})/8 \quad \textbf{(4.8)}$$

$$a_2 = M_{12}/2 \quad \textbf{(4.9)}$$

$$a_4 = (M_{11} - M_{33})/8 \quad \textbf{(4.10)}$$

The first term, $\boldsymbol{a_0}$, represents the mean value of the response, which is non-polarization-dependent, while the $\boldsymbol{a_2}$ and $\boldsymbol{a_4}$ terms represent the polarization-dependent changes in intensity. Subsequently, the degree of optical anisotropy metric ($\boldsymbol{DOA}$) is defined as the ratio of the polarization-dependent terms to the non-polarization dependent reflectance:

$$DOA \equiv (a_2 + a_4)/a_0 \quad \textbf{(4.11)}$$

4.3.3 Calibration and Processing

The image data sets were processed using both custom and pre-built functions in Matlab. Each polarization image was first normalized to images of a Spectralon diffuse reference target (Labsphere, North Sutton NH) captured at each polarization state under planar illumination and a dark image with the illumination turned off.

$$I_{ref}(x, y, \theta, f_x) = \frac{I_{smp}^{AC}(x, y, \theta, f_x) - I_{dark}(x, y, \theta)}{I_{std}^{DC}(x, y, \theta) - I_{dark}(x, y, \theta)} \times ref\% \quad \textbf{(4.12)}$$

Above, $\boldsymbol{I_{smp}^{AC}}$ represents the demodulated spatial frequency image of the sample, $\boldsymbol{I_{std}^{DC}}$ indicates the planar reflectance image of the calibration standard, $\boldsymbol{I_{dark}}$ signifies a system image with no illumination, and $\boldsymbol{ref}\%$ is the known diffuse reflectance percentage of the calibration standard. This normalization was performed on a per-pixel basis at each

polarization angle. The $\boldsymbol{I_{std}^{DC}}$ and $\boldsymbol{I_{dark}}$ images were also median-filtered with a $10\ x\ 10$ pixel window to reduce noise imparted by the reference measurements.

This pre-processing routine is necessary to eliminate light pollution and inherent system polarization from the polarized light image set. During primary processing, each polarization image set for a single spatial frequency was fit on a per-pixel basis to a modified form of **EQ 4.7**. This modified form was used to allow linear fitting (**Appendix D**) and resulted in fitting speeds of over 10^6 pixels per second. The total processing duration, including loading images into memory and pre-processing steps, was merely two minutes for a single data set.

4.4 Mie Solution to Light Scattering from Single Cylindrical Particles

The model described in **EQ 4.7** is valid for any sample with polarization-dependent optical anisotropy. This section considers a special case in which the optical anisotropy of the sample originates from infinitely long cylindrical scatterers, which are used here to represent collagen fibers (Hulst and Van De Hulst 1957, Bohren and Huffman 2008). The "infinitely long" assumption is valid when the cylinder length is large relative to its diameter; it is therefore appropriate for the tissue fibers being modelled**. Figure 4.5 (a**) indicates the geometry of this type of scattering model. Linearly polarized light is normally incident onto a cylinder with a fixed direction ($\boldsymbol{\varphi}$) defined by the cylinder's longitudinal axis. As the orientation of the incident linearly polarized light ($\boldsymbol{\theta}$) is rotated with respect to the longitude axis of the cylinder, the intensity of back-scattered light can be calculated using **EQ 4.7**, as demonstrated in an example intensity response in **Figure 4.5 (b).** The general form of the scattering matrix for light normally incident onto an infinitely long cylinder is indicated in **EQ 4.13**:

$$M_{cyl} = \begin{pmatrix} M_{11} & M_{12} & 0 & 0 \\ M_{12} & M_{11} & 0 & 0 \\ 0 & 0 & M_{33} & M_{34} \\ 0 & 0 & -M_{34} & M_{33} \end{pmatrix} \qquad \textbf{(4.13)}$$

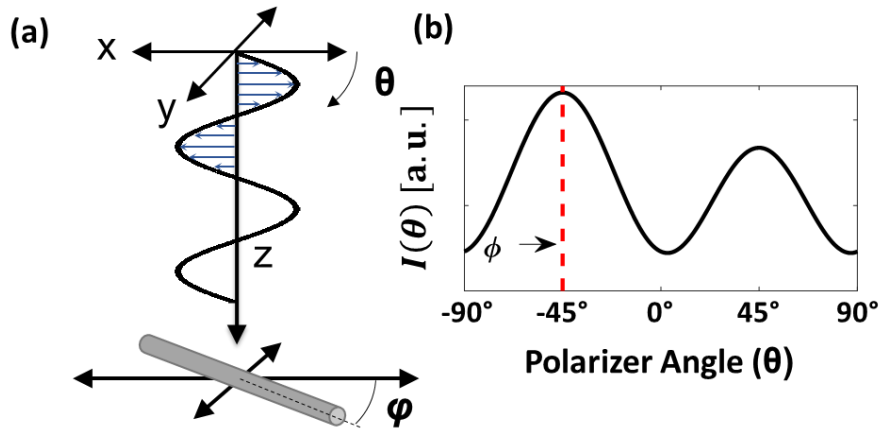

Figure 4.5: **(a)** Geometry of light with polarization angle $\boldsymbol{\theta}$ in the $\boldsymbol{XY}$-plane normally incident to a cylindrical scatterer with long-axis orientation $\boldsymbol{\varphi}$, also in the $\boldsymbol{XY}$-plane. **(b)** Intensity response of back-scattered light as a function of the relative angle between the fiber and light polarization.

$\boldsymbol{M_{11}}$, $\boldsymbol{M_{12}}$, $\boldsymbol{M_{33}}$, and $\boldsymbol{M_{34}}$ are derived from the Mie scattering solution to the special case of light incident on an infinite cylindrical particle (Hulst and Van De Hulst 1957, Bohren and Huffman 2008). The null matrix elements and the matrix symmetry result from the assumption of a system geometry in which the incident light is normal relative to the long axis of the cylinders (i.e., the fibers are in the lateral imaging plane of the system). This geometry is appropriate for representing collagen fibers in membranous tissues such as heart valve leaflets, in which the long axis of the collagen fibers exist primarily in the same $2D$ plane being imaged. The $\boldsymbol{M_{cyl}}$ elements are a result of the scattering amplitude components $\boldsymbol{T_1}$ and $\boldsymbol{T_2}$:

$$M_{11} = \frac{1}{2}(|T_1|^2 + |T_2|^2) \tag{4.14}$$

$$M_{12} = \frac{1}{2}(|T_1|^2 - |T_2|^2) \tag{4.15}$$

$$T_{33} = \mathrm{Re}\{T_1 T_2^*\} \tag{4.16}$$

$$T_{34} = \mathrm{Im}\{T_1 T_2^*\} \tag{4.17}$$

Notably, due to the configuration of the imaging system, the $\boldsymbol{T_{34}}$ matrix element does not factor into the final detected signal. Finally, these scattering amplitude components can be determined from the Mie coefficients:

$$T_1 = b_{0I} + 2\sum_{n=1}^{\infty} b_{nI}(x,m)\cos(n\Theta) \tag{4.18}$$

$$T_2 = a_{0II} + 2\sum_{n=1}^{\infty} a_{nII}(x,m)\cos(n\Theta) \tag{4.19}$$

The subscripts of these Mie coefficients $\boldsymbol{a_{nII}}$ and $\boldsymbol{b_{nI}}$ denote the special-case Mie solution for normally-incident light-scattering from infinite cylinders (Hulst and Van De Hulst 1957, Bohren and Huffman 2008). The inputs required to solve the cylindrical scattering Mueller matrix are identical to those in **Chapter 2**; they include the relative index of refraction of the particle and the surrounding media $\boldsymbol{m}$ and the size parameter for the particle $\boldsymbol{x}$, calculated here using the radius of the cylinder. In this case, however, the symmetry that was apparent in the sphere no longer holds. Rather than integrating over all azimuthal angles, only the azimuthal angles that represent the collection angle of the system, $\boldsymbol{\psi}$, have been integrated. The method for determining the number of summations ($\boldsymbol{n_{stop}}$) required for accurate approximation of the infinite summation is not identical to that described in **Chapter 2**; it is proportional to the size parameter of the simulated particle (Bohren and Huffman 2008).

4.5 EXTENSION TO FIBER POPULATIONS

In any real physical sample, a fiber orientation distribution function (***ODF***) describes the occurrence of fibers in a specific direction. The optical signal from fiber populations is therefore a weighted sum of the scattering contributions from each of the individual fibers in a specific orientation. Mathematically, this can be represented as summing the scattering function for a single fiber multiplied by the weights defined by the fiber ***ODF***:

$$I_{dist}(\theta) = \int_0^{\pi} I_{cyl}(\theta) ODF(\theta) d\theta \tag{4.20}$$

Gaussian normal distributions are often used for describing sample populations, but they are not well-suited to fiber orientation distributions which are circular. Instead, the fiber ***ODF***s are modelled and fitted using a mixed Cauchy probability density function (***PDF_{MC}***), which is described in **EQ 4.21** (Courtney, Sacks et al. 2006).

$$PDF_{MC}(\theta) = \frac{d}{\pi} + (1-d)\left[c\pi\left[1+\left(\frac{\theta-\varphi}{c}\right)^2\right]\right]^{-1} \tag{4.21}$$

In this function, **c** describes the shape of the distribution peak, ***d*** is the ratio of random fibers to non-random fibers, and ***φ*** indicates the mean fiber angle. The c parameter is bound from $[0, \infty]$, and 0 indicates no fiber variance. The ***d*** parameter has bounds from $[0, 1]$, and 1 indicates entirely random fibers. This modified Cauchy ***PDF*** is used due to its robustness in fitting a broad range of ***ODF***s found in real tissue and fiber samples. However, because the ***c*** and ***d*** parameters obfuscate physical meaning about the fiber alignment, the normalized orientation index (***NOI***) is used instead to singularly describe the fiber variance:

$$NOI = 100 \times \frac{90° - \Gamma_{50\%}}{90°} \tag{4.22}$$

Above, $\boldsymbol{\Gamma_{50\%}}$ represents the angular width of the distribution containing 50% of the total $\boldsymbol{ODF}$ (or $\boldsymbol{PDF}$). In a completely random distribution, $\boldsymbol{\Gamma_{50\%}} = 90°$, the NOI has a range of [0, 100]. **Figure 4.6** illustrates the dependence of $\boldsymbol{NOI}$ on a range of physiologically-relevant $\boldsymbol{c}$ and $\boldsymbol{d}$ parameters of the mixed Cauchy probability distribution.

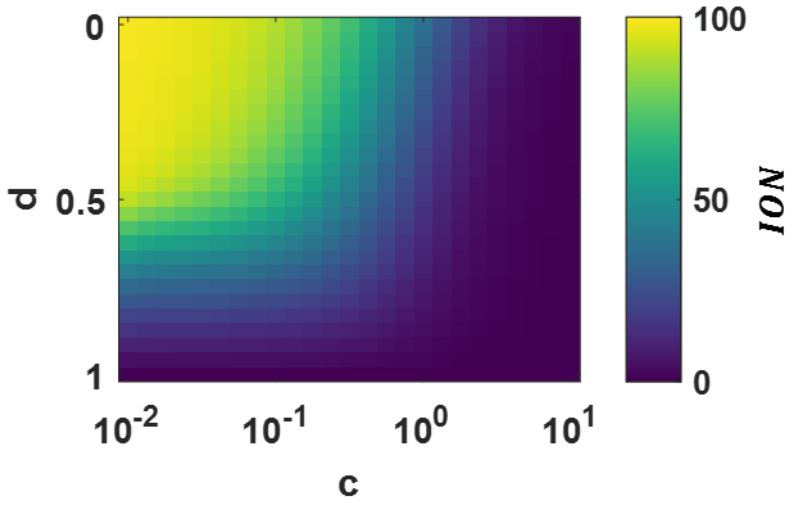

Figure 4.6: Map of $\boldsymbol{NOI}$ as a function of $\boldsymbol{c}$ and $\boldsymbol{d}$ parameters in the mixed Cauchy distribution. In electron microscopy of fiber phantoms similar to tissue, the randomness parameter $\boldsymbol{d}$ was typically over 0.4.

Variations of this orientation distribution metric have been applied in several studies which demonstrate its utility for informing mechanical models that incorporate fiber structure (Courtney, Sacks et al. 2006, Gilbert, Wognum et al. 2008, Joyce, Liao et al. 2009, D'Amore, Stella et al. 2010, Amoroso, D'Amore et al. 2011, Carleton, D'Amore et al. 2015). **Figure 4.7** presents an example simulation of the impact of fiber alignment, as characterized by NOI, on the polarized light signal. The polarization-dependent response

is maximized when the fibers are perfectly aligned in one direction ($\boldsymbol{NOI} = 100$). However, as $\boldsymbol{NOI}$ decreases, the polarization-dependent response is damped, as indicated by the decrease in the amplitude of the response curve. When the fibers are uniformly randomly aligned ($\boldsymbol{NOI} = 0$), the polarization-dependent response disappears entirely. Subsequently, the extracted $\boldsymbol{DOA}$ metric, which is a ratio of the polarization-dependent response to the non-polarization-dependent response, decreases as $\boldsymbol{NOI}$ decreases.

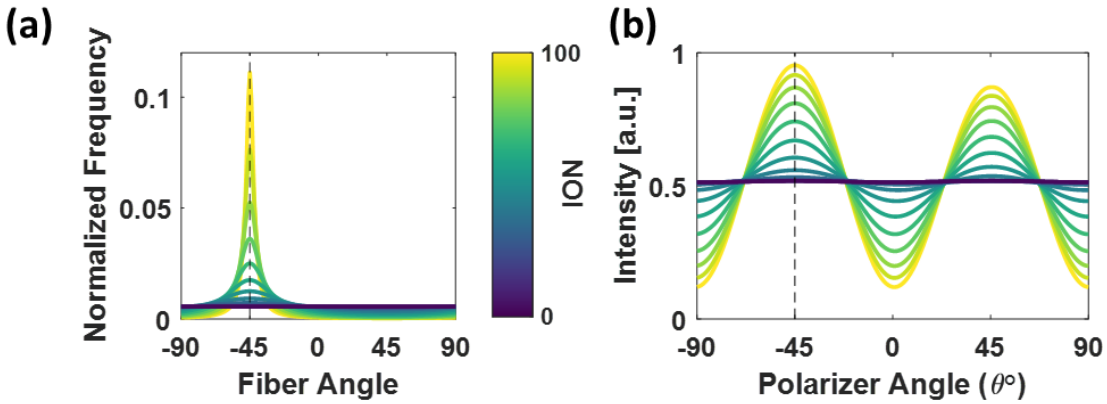

Figure 4.7: **(a)** Example of modified Cauchy fiber **PDF** as a function of normalized orientation index ($\boldsymbol{NOI}$); increasing $\boldsymbol{NOI}$ corresponds with higher alignment of the fibers; **(b)** simulation of polarization-dependent scattering response to changes in fiber anisotropy, demonstrating the amplitude of the polarization-dependent intensity decreasing as a function of decreasing $\boldsymbol{NOI}$.

4.6 ELUCIDATING THE RELATIONSHIP BETWEEN OPTICAL AND STRUCTURAL ANISOTROPY

In the preceding sections, a mathematical model has been developed which explains optical anisotropy that is resultant from underlying structural anisotropy in tissue fibers. This section validates the model to demonstrate its predictive power and then uses the model to establish a relationship between structural and optical anisotropy for a broad range of tissue fiber sizes and relative refractive indices. The latter is crucial, since relying on local measures of fiber size and refractive would severely hinder the utility of the **pSFDI**

measurements. Therefore, the objective here is to demonstrate that the relationship between optical anisotropy (***DOA***) and structural anisotropy (***NOI***) is relatively stable for tissues, such that if general (rather than precise) *a priori* sizes and refractive properties of the fibers are known, the model remains effective.

4.6.1 Methods

4.6.1.1 Electrospun Fiber Phantoms

To validate our model experimentally, electrospun fiber phantoms that varied in degree of fiber alignment were fabricated using a custom-made electrospinning mandrel (**Appendix E**) (Allen, Barone et al. 2017). The electrospinning process was utilized previously to construct tissue scaffolds with a controllable degree of microfiber alignment, mimicking tissue microstructure (Doshi and Reneker 1993, Deitzel, Kleinmeyer et al. 2001, Courtney, Sacks et al. 2006, Allen, Barone et al. 2017). To create these phantoms, a $10\%\ [wt/vol]$ solution of polycaprolactone was dissolved in hexafluoroisopropanol. This solution was ejected from a needle charged to $5\ kV$ onto a grounded, rotating aluminum mandrel. The working distance from the needle to the mandrel was $11\ cm$. Increasing the mandrel rotational velocity ($0 - 2500\ RPM$) resulted in increased fiber alignment. Six phantoms with a range of fiber alignments were collected by varying the rotational velocity of the mandrel. The samples were cut into squares approximately $1\ cm^2$ in size, bathed in dilutions of ethanol and distilled water to diminish hydrophobicity, and then imaged with **pSFDI** in a pure distilled water bath. After pSFDI imaging, the same samples were dried and sputter-coated with $15\ nm$ of platinum/palladium nanoparticles. The samples were each imaged at nine locations evenly spaced across the entire sample surface at $1000X$ magnification with a scanning electron microscope (Super40-**SEM**, Zeiss, Oberkochen Germany). The fiber orientations in the **SEM** images were analyzed and averaged across each sample using a custom image-processing routine based on a Fourier domain fiber orientation analysis technique developed by Mega et al. (**Appendix F**) (Mega, Robitaille et al. 2012). The analysis indicated a range of ***NOI*** similar to that found in tissues

(10 *to* 50) was achieved by changing the rotational speed of the collector (**Figure 4.8**). The distribution of fiber diameters was determined from the same image set, using the DiameterJ plugin for ImageJ (Hotaling, Bharti et al. 2015).

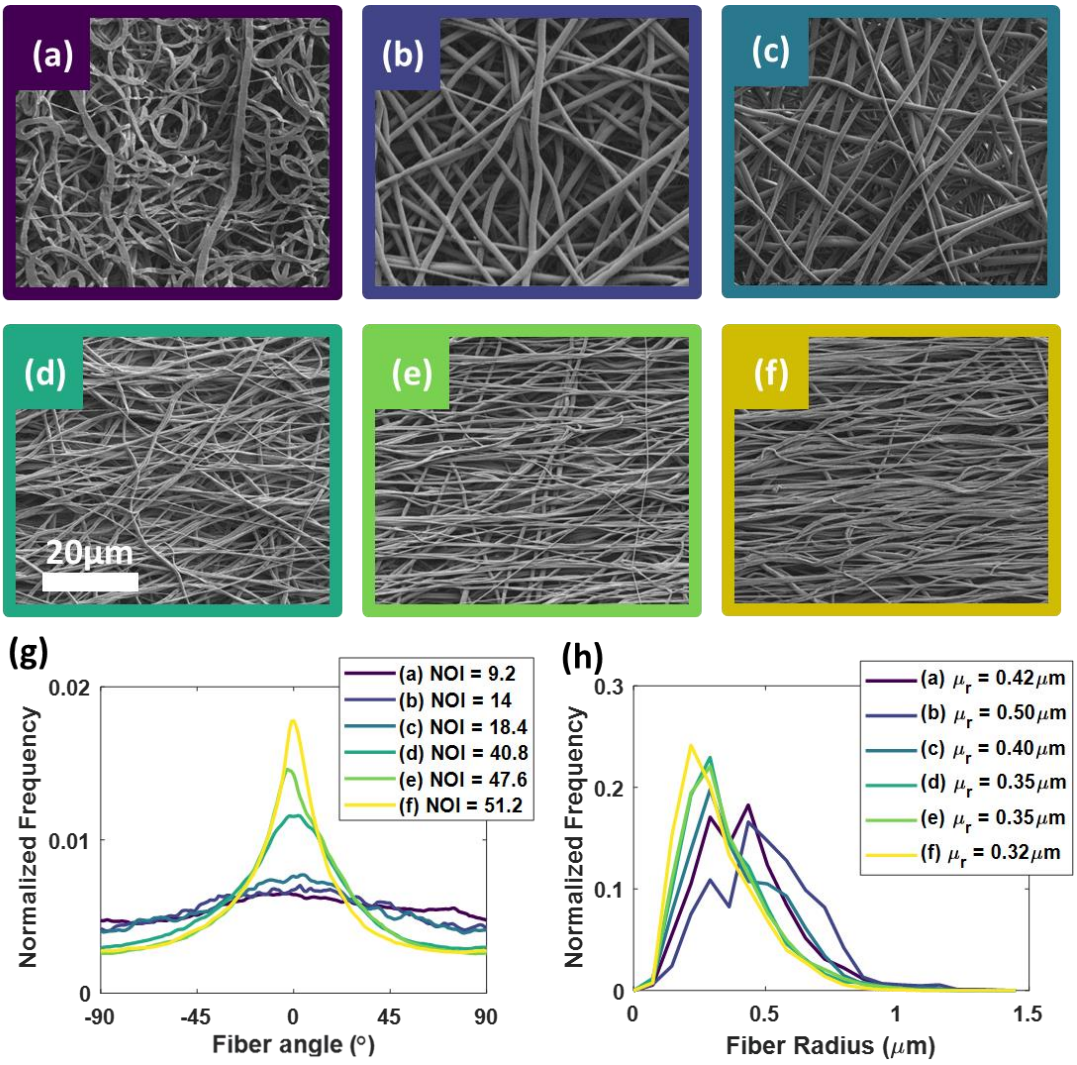

Figure 4.8: **(a-f)** SEM images of electrospun fibers collected at different rotational speeds; **(g)** extracted orientation distribution functions (***ODF***) at each collection speed along with calculated normalized orientation index (***NOI***); (***h***) distributions of fiber radii for each sample.

4.6.1.2 Simulations

Two separate simulations have been performed: The first aimed to confirm the accuracy of the model, and the second intended to examine the relationship between fiber orientation distributions and optical anisotropy measured with **pSFDI**. In the first simulation, the model was used to predict $\boldsymbol{DOA}$ for a set of electrospun fiber samples. The known fiber sizes and orientation distribution functions for each polycaprolactone fiber phantom determined from **SEM** were used as inputs into the simulation, along with the known refractive indices for polycaprolactone and water at a wavelength of $\boldsymbol{\lambda} = 529\,nm$ ($\boldsymbol{n_{fib}} = 1.45 - 1.49$, $\boldsymbol{n_{bgd}} = 1.33$) (Mark 2007). In the second simulation, expected $\boldsymbol{DOA}$ from cylindrical fibers was calculated across a large range of physiologically-relevant size parameters ($\boldsymbol{x}$) and relative refractive indices ($\boldsymbol{m}$). The fiber sizes simulated were based on the expected range of collagen fiber radii discovered in recent studies of heart valve tissue (Ayoub, Tsai et al. 2018). The relative refractive index included a range relevant to hydrated collagen in interstitial fluid ($\boldsymbol{n_{fib}} = 1.38 - 1.42$, $\boldsymbol{n_{bgd}} = 1.33 - 1.35$) (Wang, Milner et al. 1996, Bashkatov, Genina et al. 2000, Jacques 2013). A convolution of the results was then performed with the fiber $\boldsymbol{PDF}$ discussed in the previous section. The $\boldsymbol{PDF}$ parameter ranges were based on those relevant to biological tissue as well as those determined for the electrospun fiber phantoms (Ayoub, Tsai et al. 2018). **Table 4.1** indicates the parameter range for the second simulation.

Table 4.1: Physiological polarized light-scattering model simulation parameter space.

Parameter	***Minimum***	***Maximum***	***#***	***Spacing***
Fiber radii ($\boldsymbol{r_{cyl}}$)	50 µm	1000 µm	1173	Logarithmic
Relative Refractive Index ($\boldsymbol{m}$)	1.005	1.12	21	Linear
Distribution parameter ($\boldsymbol{c}$)	10^{-2}	$10^{0.5}$	25	Logarithmic
Randomness parameter ($\boldsymbol{d}$)	0.4	1	25	Linear
Normalized Orientation Index (***NOI***)	0	100	625	N/A

4.6.2 Results

4.6.2.1 Model Validation

Figure 4.9 (a-f) illustrates the cropped raw images of the electrospun fiber samples**;** the samples correspond with the same labels in **Figure 4.8(a-f)**. A $200x200$ pixel region of interest, indicated by the red boxes, was utilized to compute the mean and variance of measured $\boldsymbol{DOA}$ values for each sample.

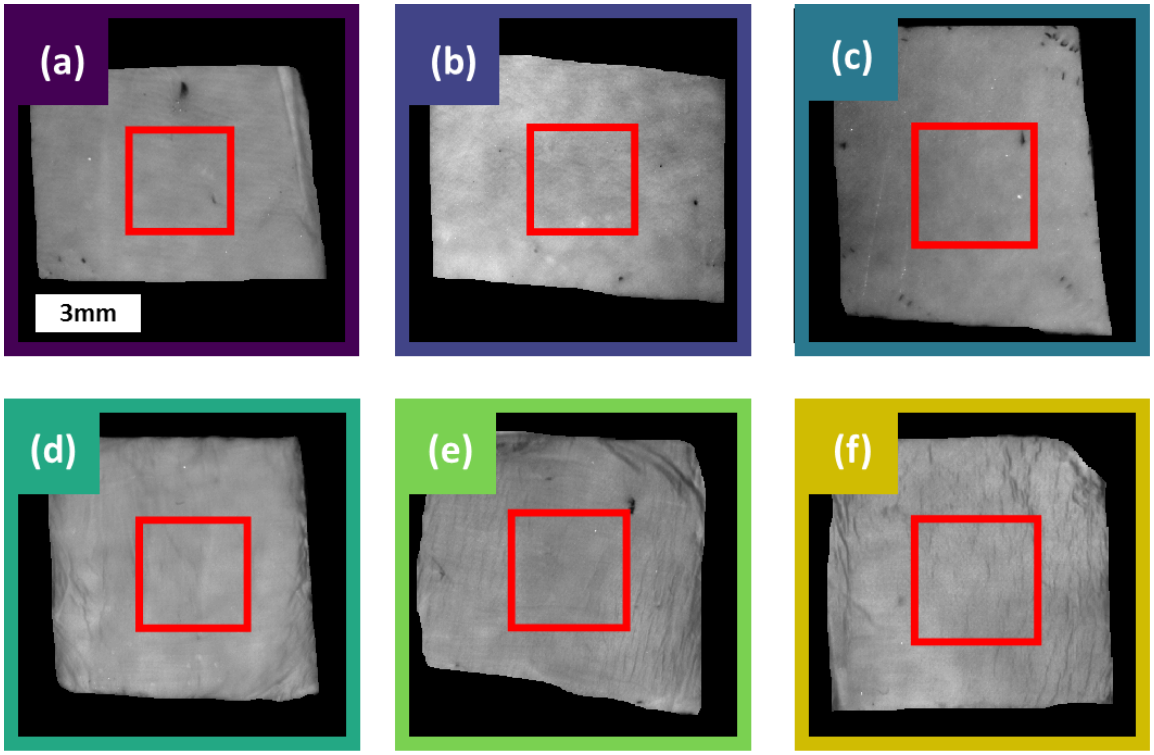

Figure 4.9: Raw images of the six fiber samples, with colors and letters corresponding with the same samples in **Figure 4.8**. The red box indicates the region of interest over which pSFDI measurements were averaged.

The $\boldsymbol{DOA}$ measured for each sample are compared with the corresponding $\boldsymbol{DOA}$ predicted by our model in **Figure 4.10**. Error bars in the y-axis indicate the standard deviations of measured $\boldsymbol{DOA}$ across the region of interest for each sample depicted in

Figure 4.9, and error bars in the x-axis represent the standard deviations of the predicted ***DOA*** for each sample based on the range of fiber diameters used for input into the model (**Figure 4.8**).

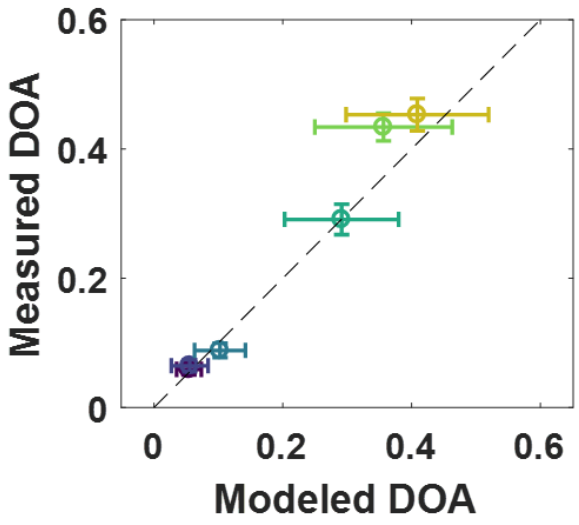

Figure 4.10: Measured ***DOA*** from **pSFDI** data relative to modeled ***DOA*** for the same samples, using known fiber properties as model inputs. Error bars illustrate standard deviations for the model output for the range of fiber properties provided for the input (x-axis) and standard deviation of the measured data within the image region of interest (y-axis).

The modeled values demonstrated a significantly larger variation in the predicted ***DOA*** relative to the measured ***DOA***, which was primarily a result of the oscillatory nature of scattering when the size of the scattering particle is close to the wavelength of incident light. However, the measurements and model suggested overall linear agreement: Experimental measurements of ***DOA*** were all within 16% of the model-predicted values and were all contained within one standard deviation of the model's predicted values.

4.6.2.2 Simulated relationship between DOA and NOI

The simulation of a broad range of fiber properties and distributions demonstrated that $\boldsymbol{DOA}$ has a strong linear dependence upon $\boldsymbol{NOI}$. **Figure 4.11** illustrates the simulated $\boldsymbol{DOA}$ as a function of $\boldsymbol{NOI}$ for the range of fiber parameters in Table 1. The shaded area represents the standard deviation around mean $\boldsymbol{DOA}$ at each evaluated $\boldsymbol{NOI}$, which describes the variation of the model due to the range of fiber sizes and relative refractive indices within the model space. A clear linear trend ($\boldsymbol{DOA} = \boldsymbol{A} \times \boldsymbol{NOI}$) characterizes the model space ($\boldsymbol{r^2} = 0.95$). The linear model fit coefficient $\boldsymbol{A}$ was $6.66x10^{-3}$. This fit model was subsequently inverted to establish a linear conversion of relative $\boldsymbol{DOA}$ from the $\boldsymbol{pSFDI}$ data to absolute $\boldsymbol{NOI}$.

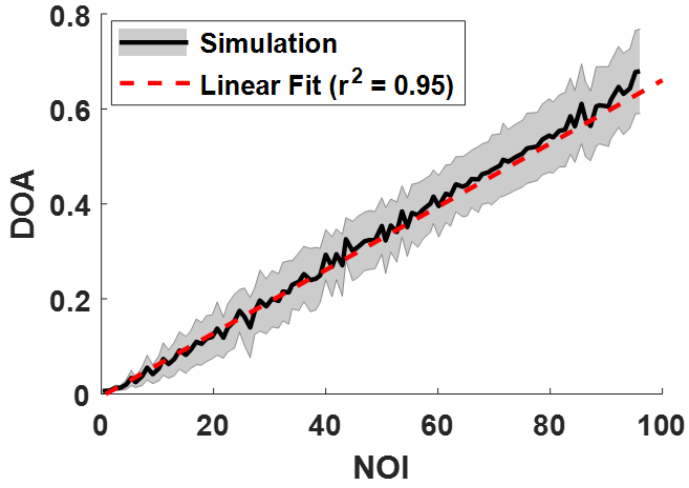

Figure 4.11: Simulated $\boldsymbol{DOA}$ as a function of $\boldsymbol{NOI}$, for a range of physiologically-relevant fiber distributions, sizes, and relative refractive indices. The shaded region is the standard deviation of simulated $\boldsymbol{DOA}$ at each evaluated $\boldsymbol{NOI}$ value. The linear fit was inverted to estimate $\boldsymbol{NOI}$ as a function of $\boldsymbol{DOA}$.

4.7 DISCUSSION

This section presents an extended analysis of polarized light reflectance from cylindrical scatterers that allows extraction of absolute fiber alignment, as quantified by the normalized orientation index (***NOI***). The measurements of electrospun fiber samples with known fiber properties validated the model performance, with good agreement between modeled and measured optical anisotropy for the system. Additionally, the clear linear relationship between optical anisotropy (***DOA***) and structural anisotropy (***NOI***) allowed the extraction of absolute alignment information from the polarized light measurements. This relationship is valid for a substantial range of fiber sizes ($\boldsymbol{r_{cyl}} = 50 - 1000nm$) and relative refractive indices ($\boldsymbol{m_{rel}} = 1.02 - 1.12$) that are relevant to both tissue and biomimetic tissue constructs. Therefore, the limited number of assumptions and only general *a priori* knowledge about the fibers in the sample allows fiber alignment between samples to be compared more accurately.

An important finding of this study relates to the types of ***PDF***s used to model the fiber populations for the simulation and to fit to the fiber populations from **SEM**. This has been iterated through several different types of fiber distributions while developing our computational model space, primarily based on the most appropriate fits of real fiber distributions characterized with **SEM** for the electrospun fiber samples and past experiments. Two circular distributions (wrapped Cauchy and von Mises) were initial candidates, but they did not fit the ***ODF***s from the ***SEM*** data adequately. Additionally, the ***d*** term, which quantifies the proportion of randomly oriented fibers in the modified Cauchy distribution, was demonstrated to be pivotal in the computed ***DOA*** metric, and therefore in the relationship between the **pSFDI** data and extracted ***NOI***. This ***d*** term is crucial for model performance because it accounted for the non-polarization-dependent scattering from both randomly distributed cylindrical scatterers and non-cylindrical scatterers. The n normalization of the measurements is a common issue in extracting absolute measures of fiber orientation. The non-polarization-dependent reflectance component arises both from cylindrical and non-cylindrical scattering, and the contributions from each are nearly

impossible to fully decouple. Combining these terms eliminates the need to distinguish between fiber alignment and fiber volume fraction for a specific sample area when normalizing the data in the $\boldsymbol{DOA}$ metric.

One deficiency of the light scattering model is that it does not account for the polarization response resultant from multiple-scattering from cylinders; this is a potential source of error between the model and experimental data. However, co-polarized imaging and sub-diffuse spatial frequency domain imaging both limit the number of scattering interactions that the system detects, such that the signal response is primarily representative of light undergoing few scattering events (Jacques, Roman et al. 2000, Wiest, Bodenschatz et al. 2015). In addition to constraining the measurements to primarily back-scattering events by using high spatial frequencies, which aligns with the assumptions of the scattering model, the gating of reflectance to a small number of ballistic scattering events results in reduced sampling volumes, which further refines the lateral and axial sampling volumes.

Chapter 5: Analysis of tissue fiber structure in heart valve tissues

5.1 MOTIVATION: QUANTIFICATION OF TISSUE STRUCTURE IN HEART VALVE TISSUES

Heart valve disease is the one of the most common heart diseases in patients from developed countries, with some form affecting more than 12% of the elderly population (Nkomo, Gardin et al. 2006, Iung and Vahanian 2011, Osnabrugge, Mylotte et al. 2013). Over 90,000 moderate to highly invasive valve replacement surgeries are performed annually in the United States alone, and this number is expected to expand alongside increased aging in the population (Clark, Duhay et al. 2012). Although artificial valves can be either mechanical or bio-prosthetic, over 80% of contemporary procedures now use bio-prosthetic heart valves (**BHV**s) derived from animal valves or pericardium because of their superior functional performance (Pibarot and Dumesnil 2009). However, these valves often suffer from premature degeneration and functional failure, thereby necessitating multiple subsequent surgeries to replace valves. This is particularly concerning for patients under 40 who live many decades after their initial replacement but are faced with a 10-year valve failure incidence of 20% to 30% (Pibarot and Dumesnil 2009, Singhal, Luk et al. 2013). Among older patients, surgical intervention is inherently extremely hazardous due to these patients' fragile state of health and the inherent physical strain of the surgery. Transcatheter valve placement as an alternative to surgery is currently reserved exclusively for cases of heart valve disease in which invasive surgeries are impossible, and valve integrity after packing into a small catheter lumen are not yet well known (Smith, Leon et al. 2011). There is an immediate necessity for **BHV**s which are longer-lasting and exhibit more robust in vivo functional performance.

Several mechanisms can contribute to failure in the valves. Inflammatory and immune responses are generally short-term considerations that can result in scar formation and structural deterioration. These rejections typically occur in the first several weeks to months of implantation, with a typical incidence of 1 to 6% (Edmunds, Clark et al. 1996). Long-term failure of BHVs has traditionally been attributed to two primary causes, namely structural degeneration of collagen fibers and valve-stiffening due to calcification (Schoen,

Levy et al. 1985, Vyavahare, Ogle et al. 1999, Sacks, Schoen et al. 2009). Calcification was the primary cause of **BHV** failure until demineralization treatments were incorporated directly into the valves. Some degree of calcification still occurs, but at a much lower rate, similarly to inflammatory and immune responses. In contrast, some studies suggest that the structural degeneration of collagen fibers is the primary mechanism behind long-term valve failure, particularly since inflammation, rejection, and calcification can, in many instances, be mitigated (Vyavahare, Hirsch et al. 1997, Sacks and Schoen 2002, Schoen and Levy 2005).

Microstructural degeneration is a constant threat to the valve due to the physical stresses inherent to its normative function (Lee and Sacks 2016). The valve is alternatively pressurized while closed to restrict the regurgitation (backflow) of blood within the heart chambers; it is then collapsed against the wall to permit unidirectional blood flow through the heart (**Figure 1.1**). Stenosis occurs due to functional failure of the valve when the valve can only partially open or close; this can ultimately result in arrhythmia, heart failure, and death.

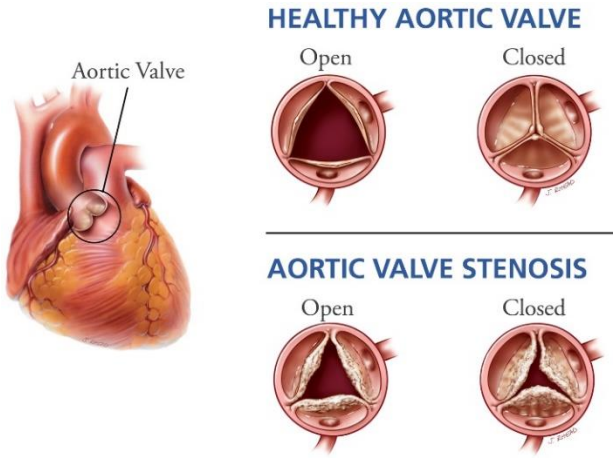

Figure 5.1: Healthy and diseased aortic valves, indicating functional degradation that results from valve stenosis (HealthJade 2018).

Tears around the valve cusp which anchor the leaflet to the stent wall in **BHV**s can occur after approximately five years due to the high stress levels in these areas (Walley,

Keon et al. 1992, Vesely 2003, Singhal, Luk et al. 2013). After seven to eight years of implantation, changes in the tissue material structure and composition can precipitate functional failure. This can result from fraying of collagen fibers over time, macroscopic tears in the valve, and regional changes in the microstructure due to mechanical conditioning of the valve (Singhal, Luk et al. 2013). In any case, the overall failure of the valve results from the degradation of the collagen structure in **BHVs**, which are often homogeneous and regionally constant in collagen structure relative to the native valve, which has a well-organized, heterogeneous, and variably anisotropic collagen fiber structure. Since the prosthetic valves lack this organization, their lifetime expectancy is highly variable, and current valve manufacturing methods do not permit adequate screening for precursors of structural degeneration.

Combating structural failure therefore requires two efforts, including improving the **BHV** microstructure and assessing **BHV** tissue for long-term functional integrity prior to implantation. Pre-conditioning of **BHV** materials through controlled loading cycles or biochemical treatments are common procedures for improving **BHV** robustness, but it is difficult to determine whether areas of structural weakness remain (Billiar and Sacks 2000, Billiar and Sacks 2000, Stella, Liao et al. 2007). To determine the probability of valve failure, individual valve leaflets or entire pericardial sheets are often subjected to mechanical failure testing analyses. These methods, however, are either simplified in such a manner that neglects the effect of tissue heterogeneity and variable anisotropy or are so exhaustive that they require weeks to complete. Additionally, these techniques result in the destruction of the valve material, which means that they can only be used as a random control for batches of valves and cannot be performed on valves which will be implanted (Sacks 2000, Stella and Sacks 2007). Therefore, the macroscopic heterogeneity of microscopic fiber structure in both native and bioprosthetic heart valves is poorly understood. Consequently, bioprosthetic valves with structural imperfections that will produce functional failure are often implanted, which leads to highly variable valve performance and premature valve failure. The most immediately beneficial and achievable solution to the problem of variable performance in **BHV**s is a tool for rapidly and non-

destructively assessing their structural organization. Additionally, this organizational information can aid in the development of computational models which predict heart valve function; once validated experimentally, these can be used as *in silico* long-term fatigue analysis of valve performance (Zhang and Sacks 2017).

Several imaging modalities have been employed as non-contact assessment techniques to map collagen fiber structure in **BHV**s, but these techniques are affected by several disadvantages which limit their utility. Diffusion tensor magnetic resonance imaging (**dt-MRI**) provides 3D macroscopic geometry and microstructural sensitivity but has relatively poor resolution ($> 100\ \mu m$), and extremely lengthy imaging times of over 10 hours precludes dynamic imaging (Teh, McClymont et al. 2016). Micro-computed tomography (**μCT**) has provided improved resolution in dynamic 3D surface geometry of heart valve tissues relative to **dt-MRI** and traditional **CT** methods but does not provide insights into the collagen microstructure (Badea, Fubara et al. 2005).

Optical techniques improve image resolution and sensitivity to fiber alignment immensely, rather than merely enhancing direction. However, many current imaging systems are not well-suited to the demands of non-destructive, rapid imaging of multi-layered tissue over tissue-level fields of view. Small angle light scattering (**SALS**) requires thin, optically-clear samples and must use either a fixation treatment, physical sectioning, or a combination of the two to image the **BHV** tissue (Sacks, Smith et al. 1997). These destructive preparations require the sample to be discarded after assessment. Reflectance techniques, such as second harmonic generation (**SHG**) and optical coherence tomography (**OCT**), can produce striking images of individual fibers distributed within the tissue; however, although these techniques are less destructive and have high resolution, they have minimal fields of view and are not appropriate for imaging appreciable portions of the entire **BHV** (De Boer, Milner et al. 1997, Adams, Roberts et al. 2002, Brown, McKee et al. 2003). Additionally, all of the discussed techniques are point-based, requiring lengthy scan times to acquire full image sets; this severely restricts their capability for dynamic functional imaging of large-scale $2D$ and $3D$ tissue geometries.

This chapter aims to demonstrate the use of the **pSFDI** system described in **Chapter 4** to address the current need for non-destructive, rapid, wide-field mapping of fiber structure in multi-layered tissues. First, it demonstrates **pSFDI** equivalency to static **SALS** imaging of planar heart valve leaflets, along with the ability to detect microstructural differences in the various leaflet layers. Second, the increased imaging rate of the system is used to detect fiber kinematics with **pSFDI** during mechanical deformation of ovine pericardium. Finally, this chapter demonstrates **3D-pSFDI** as a proof-of-concept for imaging leaflet microstructure in an intact **BHV**.

5.2 FIBER MAPPING IN STATIC HEART VALVE LEAFLETS

5.2.1 Objectives

Collagen fiber structure in leaflets of the aortic valve has been well-studied. In addition to regional variations along the surface of the leaflets, there are multiple layers that have been proven to have distinct microstructure and mechanical properties (Stella and Sacks 2007). The fibrosa is an outer layer which is responsible for most of the structural integrity of the valve; a substantial number of regularly-aligned collagen fibers are oriented orthotropically along the circumferential direction of the valve (**Figure 5.2**). The second outer layer is the ventricularis, which also contains a significant amount of collagen but has less overall organization aside from transversely isotropic fiber alignment. The spongiosa is often described as a transition region between the two outer layers and primarily contains water mediated by glycosaminoglycans (**GAG**s). It has been demonstrated that the **GAG**s exert limited impact on the functional mechanical behavior of heart valve leaflets (Eckert, Fan et al. 2013).

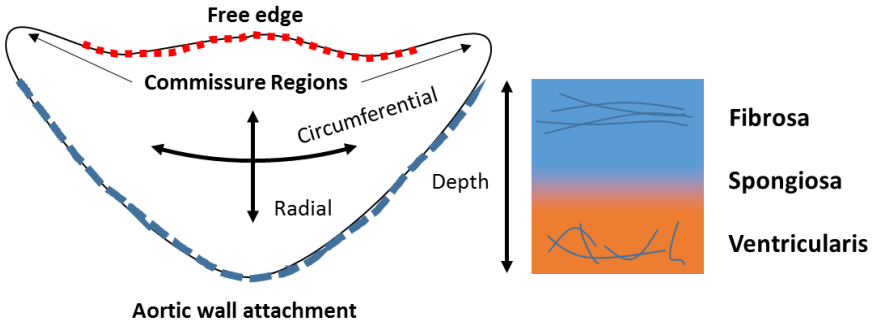

Figure 5.2: Orientation, morphology, and layers of the native aortic valve leaflet.

The existing **SALS** technique, which is transmissive, cannot resolve the differences in terms of fiber structure in these layers. Additionally, the sampling volumes of traditional polarization imaging systems are typically greater than the entire leaflet thickness ($\sim 400\ to\ 800\ \mu m$) This study was intended to demonstrate the similarity in overall fiber orientation measured using **SALS** and **pSFDI**, and the differences in fiber alignment revealed by the volumetric sampling control achieved using the **pSFDI** technique.

5.2.2 Methods

A fresh ovine aortic valve leaflet was excised and fixed with glutaraldehyde for 24 hours while pressed between glass slides. The samples were then washed, placed in a bath of phosphate buffered saline, and imaged with **pSFDI** on both sides; this allowed a comparison of the two outermost layers of the leaflet, namely the fibrosa and the ventricularis. The same sample was subsequently bathed in dilutions of glycerol and water to optically clear the sample and then mounted again between glass slides prior to imaging with **SALS** (Sacks, Smith et al. 1997). The primary fiber orientation angle ($\boldsymbol{\varphi}$) and normalized orientation index ($\boldsymbol{NOI}$) were extracted from the **SALS** data across the sample in 250 μm steps. The images from **pSFDI** and **SALS** were all co-registered by binarizing the raw intensity images for each data set and using the Matlab function *imregtform*, which

limited the transformation to rotation and translation. The **SALS** images were additionally up-sampled to match the **pSFDI** data in pixel resolution; however, this did not result in any genuine increase in resolution. Any rotational transformations applied during registration were subsequently accounted for in the final fiber orientation maps.

Additionally, the glutaraldehyde fixation protocol was not necessary for either imaging technique but was instead performed to ensure the repeatability of fiber alignment measurements between the two techniques. Although this treatment may alter the native microstructure, since the collagen fibers are cross-linked, the objective of this experiment was to allow a comparison between the two imaging techniques; therefore, it was necessary that the microstructure was fixed since the sample was transferred between systems. The optical clearing with glycerol, however, was required for the transmissive **SALS** imaging technique.

5.2.3 Results

The different configurations of **pSFDI** and **SALS** systems are visible in **Figure 5.3:a-c**. The raw intensity images of the ovine aortic valve leaflet samples matched well among the **pSFDI** and **SALS** imaging techniques; this demonstrates effective registration of morphological features between the three data sets (**Figure 5.3:d-f**). For example, the tendon-like tertiary bundles of fibers in the commissure regions (top right and left corners) were visible in all three sets of images, although they were more readily discernable in the **pSFDI** images. The higher sampling resolution of the **pSFDI** images ($19\ \mu m$) illustrated these morphological structures more clearly than the accompanying **SALS** images ($250\ \mu m$). Fiber orientation (**Figure 5.3:g-i**) also matched properly between all image sets and aligned with previous studies concerning heart valve fiber orientation (Sacks, Smith et al. 1997, Yang, Lesicko et al. 2015).

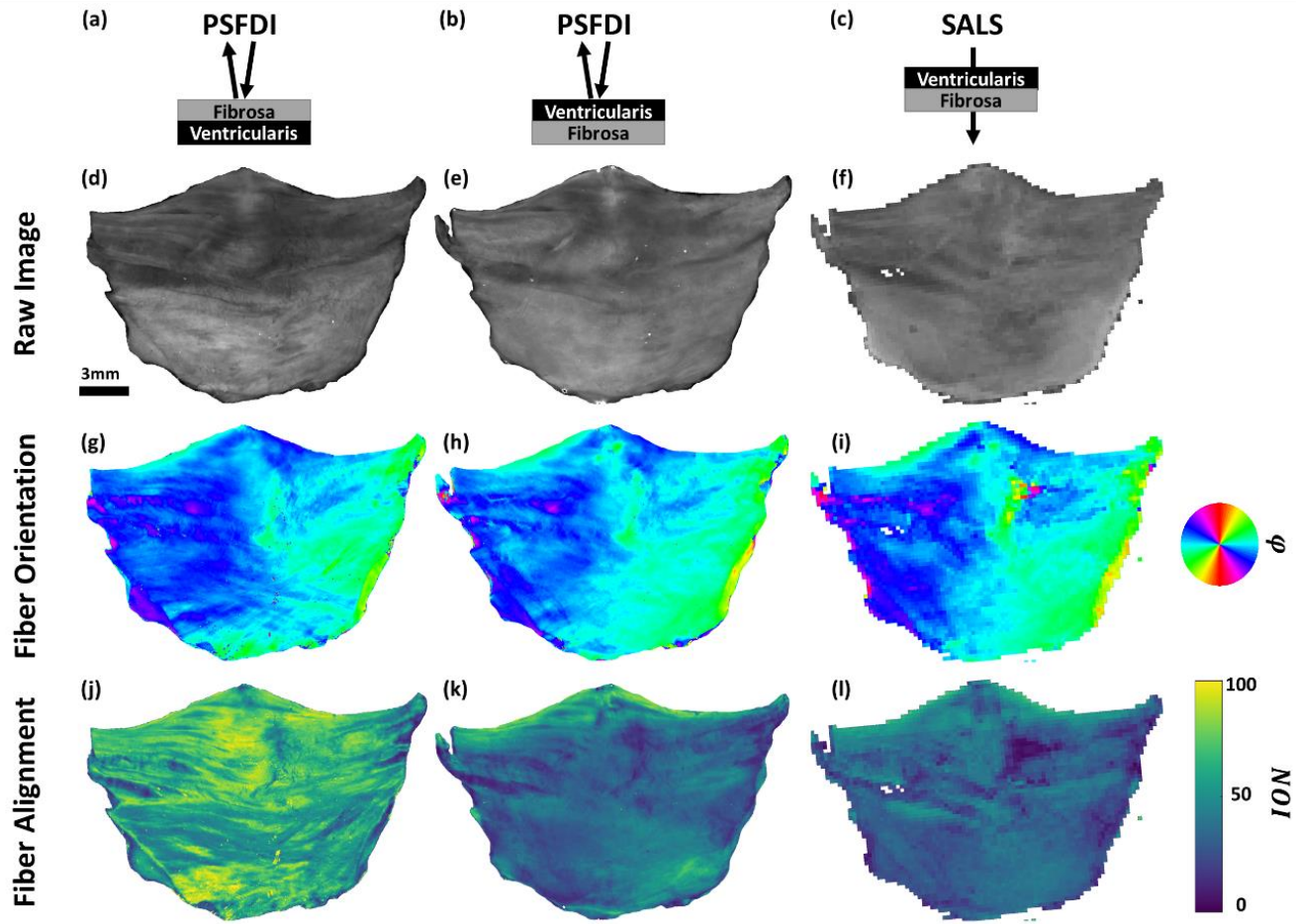

Figure 5.3: Ovine aortic valve leaflet imaging results: **(a-c)** Imaging geometry for the results in each column; **(d-f)** raw-intensity images for each technique; **(g-i)** extracted fiber orientation, demonstrating proper agreement between each technique; **(j-l)** extracted fiber alignment from each technique.

While the fiber orientations were primarily the same, suggesting overall consistency in fiber directionality through the thickness of the sample, the $\boldsymbol{NOI}$ maps indicated markedly different alignment on opposite sides of the sample. The **SALS** data appeared to be approximately a summation of the results from both **pSFDI** data sets. This was expected, since **SALS** is a transmissive technique which is sensitive to all layers through the depth of the tissue, while the **pSFDI** technique exhibited sensitivity to only the outermost layers on each side.

Overall, **pSFDI** demonstrated sensitivity to differences in fiber alignment between the leaflet layers, while the **SALS** system could not. Although similar features were evident in both the **pSFDI** alignment map on the ventricularis side (**Figure 5.3:k**) and the **SALS** transmission alignment map (**Figure 5.3:l**), the **pSFDI** alignment map displayed a marked increase in $\boldsymbol{NOI}$ in the fibrosa.

5.2.4 Discussion

This research has demonstrated the ability to capture high-resolution regional heterogeneity in heart valve leaflet tissue structure without any destructive sample preparation. There were clear differences in the **pSFDI** images of opposite sides of the leaflet, indicating the ability to distinguish distinct layers of fiber structure in aortic heart valve leaflets which could not be captured using transmission-based techniques or techniques that have extended depth sampling equivalent to the sample thickness. Differences in fiber alignment on the fibrosa and ventricularis sides of the leaflet tissue were the most apparent, which confirmed the increased presence of highly-aligned collagen fibers in the fibrosa. This improved **pSFDI** technique provides an effective means for rapid, reflectance-based mapping of collagen fiber alignment, with an adjustable imaging depth

for investigating multi-layered tissues without the need for chemical treatment or physical sectioning.

The **pSFDI**-derived $\boldsymbol{NOI}$ values were determined to be higher than the $\boldsymbol{NOI}$ values extracted with **SALS** in the ovine aortic valve leaflet, which was anticipated. This was because the **SALS**-derived $\boldsymbol{NOI}$ values represented a summation of the different fiber layers throughout the thickness of the sample. This effectively averages the orientation metric across different populations of fibers with varying degrees of alignment and differing primary alignment directions, yielding an overall decrease in measured alignment. The **pSFDI** values are limited to superficial layers, which resulted in measured fiber alignments being confined to fiber populations representing the various layers of the sample. The experimental results demonstrated this, measuring markedly higher fiber alignment on the fibrosa side of the leaflet.

5.3 DYNAMIC FIBER MAPPING DURING BIAXIAL DEFORMATION

5.3.1 OBJECTIVES

In addition to the improved spatial resolution and volumetric sampling capabilities of **pSFDI**, it also achieves a significantly higher imaging rate, requiring merely five seconds to capture a full data set for a single spatial frequency. This relatively fast imaging speed, along with the reflective imaging geometry, renders **pSFDI** readily capable of pseudo-dynamic imaging of fiber kinematics during biaxial planar deformation. The mechanical properties of several planar samples utilized to construct **BHV**s, including native heart valve leaflets, pericardium, and synthetic electrospun fiber mats, have been previously tested using planar biaxial deformation; however, typically, the fiber alignment in the entire sample is only measured before and after mechanical testing is concluded (Billiar and Sacks 2000, Billiar and Sacks 2000, Sacks 2000, Sun, Sacks et al. 2003, Stella,

Liao et al. 2007, Stella and Sacks 2007, Joyce, Liao et al. 2009). Fiduciary markers can be used to detect local strain fields, but the fiber kinematics may not be directly sampled. Some studies have used **SALS** to image the full sample suffering from potential stress-relaxation and mechanical creep during the extensive imaging times (Billiar and Sacks 1997). Additionally, the transmissive imaging geometry of SALS renders strain-control substantially more difficult, since fiduciary markers are present and block fiber content and limit imaging field, and the glycerol clearing necessarily alters the physical properties of the sample. **pSFDI** offers a powerful means for studying fiber kinematics directly during mechanical tissues deformation.

5.3.2 Methods

A 4 cm^2 sample of pre-sorted ovine pericardium was mounted onto a calibrated biaxial stretching device (Billiar and Sacks 2000) and subjected to stress-controlled equibiaxial loading cycles. The sample was oriented so that fibers were aligned primarily in the $y-$axis of the imaging system. The testing protocol consisted of taring the sample to a 1 g load in both axes, followed by 15 preconditioning cycles with a 20 second half-cycle duration and a 225 kPa maximum load in each axis. The sample was then returned to tare loads of 1 g and was subsequently imaged with **pSFDI** in 30 steps from the tare load to the maximum 225 kPa load in each axis. A spatial frequency of $f_x = 0.5\ mm^{-1}$ was used for imaging.

5.3.3 Results

The tare load state, 15% load state, and maximum load state of the pericardial material are illustrated in **Figure 5.4**. Both the fiber orientation and fiber alignment maps demonstrated local changes in fiber alignment across the sample surface.

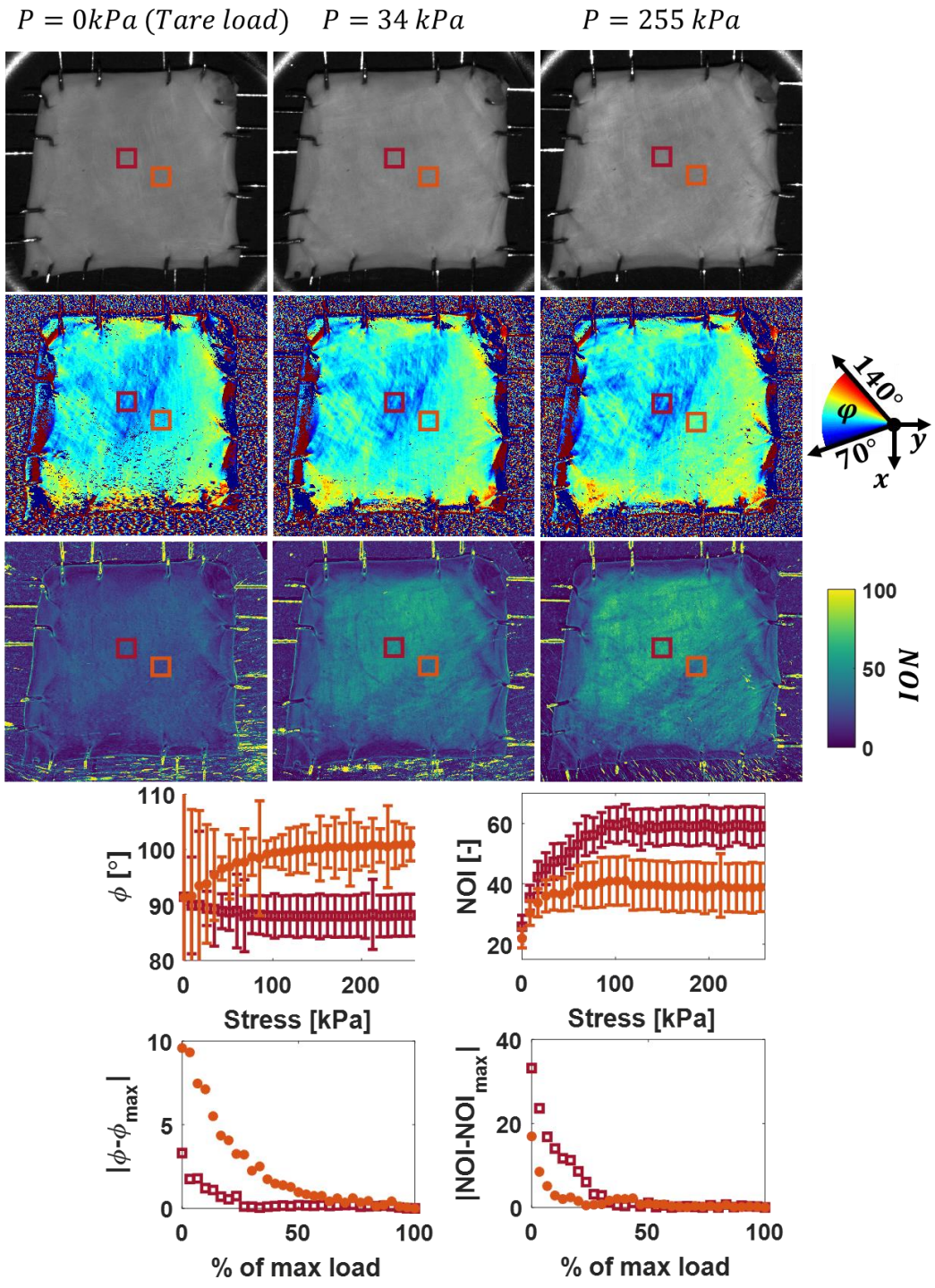

Figure 5.4: Observation of fiber kinematics using **pSFDI** during stress-controlled biaxial deformation of pericardium; this highlights the ability to infer local differences in fiber recruitment and collagen uncrimping.

To highlight this regional heterogeneity, two **ROI** with similar initial orientation and alignment were selected for comparison. In the first **ROI** (maroon inset, square marker), the orientation was relatively constant during the loading cycle ($\Delta\bar{\boldsymbol{\varphi}} = 3°$), while the mean $\boldsymbol{NOI}$ increased significantly ($\Delta\overline{\boldsymbol{NOI}} = 25$). In the second **ROI** (orange inset, circular marker), the sample displayed substantial initial variation in fiber orientation, and the average orientation angle changed over the course of loading by over 9°. Conversely, the mean $\boldsymbol{NOI}$ only increased modestly for the second area ($\Delta\overline{\boldsymbol{NOI}} = 10$). Additionally, the rate of change in terms of both orientation and alignment in the regions differed. In the first **ROI**, the maximum orientation change was achieved at 25% of the maximum stress load, while the second **ROI** continued to increase until about 90% of the maximum stress load. Similarly, the rate of load-dependent change of $\boldsymbol{NOI}$ differed for both samples. In this case, the maximum $\boldsymbol{NOI}$ was achieved for the second **ROI** more rapidly, at about 25% of the maximum load, relative to 40% for the first **ROI**.

5.3.4 Discussion

The local fiber kinematics quantified with **pSFDI** in the pericardium samples may be used to infer two distinct responses of the tissue to loading. The first is fiber recruitment, in which the fibers are re-aligned with the major axis of stress or strain. The second **ROI** appears to highlight this phenomenon: The large variance in initial fiber alignment decreases as a function of increased load state, and the mean fiber alignment changes gradually throughout the loading protocol. Additionally, this region does not experience a significant increase in fiber alignment, which is consistent with fibers being re-aligned from their preferred state.

The second inferred kinematic phenomena is fiber-uncramping, in which collagen fibers are straightened from their crimped, unloaded state as a response to loads. This

allows an initial elastic response of tissues, primarily dictated by elastin stiffness that holds the crimp's shape. After the collagen fibers are straightened, the tissues become significantly stiffer, since the elastic properties are dictated primarily by the relatively stiff collagen fibers. This appears to occur in the first **ROI**, in which the fibers are pre-aligned in the direction of local stress. Limited changes in fiber direction in this region, coupled with drastic changes in alignment, suggest that sensitivity to microscale changes in fiber crimping is induced by the loading.

5.4 FUTURE WORK: 3D-FIBER MAPPING

5.4.1 Objectives

A final potential application of **pSFDI** entrails simultaneous extraction of fiber microstructure and surface topography. Previous studies have reported macroscopic **BHV** geometry during in cyclical flow loop testing to understand the dynamic behavior of the leaflets' geometry. However, in these studies, the fiber alignment data can only be measured before the leaflets are mounted onto the **BHV** scaffold or after they have been removed from the scaffold after testing. These changes in the deformation of the leaflets can result in changes in the microscopic structure across the entirety of the leaflet; therefore, imaging the intact **BHV** is preferred to directly couple fiber microstructure to macroscopic geometry and function.

As discussed in **Chapter 2**, if an atypical orientation of the spatial frequency patterns is used, then the resulting phase shift will directly correspond with the height of the sample surface. However, this compromises the sectioning capability, since the change in phase shift affects the measurement of modulated reflectance. However, in this case, two sets of measurements can still be performed in rapid succession; a first set may use the typical orientation to extract measures of fiber microstructure with volumetric sampling,

and a second set may apply the atypical orientation. Measuring topography requires only three additional images to be collected and does not require measurement at every polarization state, since the data sets are already registered. By combining these two data sets, the fiber alignment data can be mapped to 3D surface profiles describing the BHV geometry.

5.4.2 Methods

Using the atypical configuration of the spatial frequency patterns (**Figure 2.7**), a phase- Using the atypical configuration of the spatial frequency patterns (**Figure 2.7**), a phase-shifting profilometry technique with direct height-mapping described by Zhou and Su was used to reconstruct surface topography (Zhou and Su 1994). The absolute phase of the sample and a reference plane of known relative height were extracted using **EQ 2.29** (**Figure 5.5**). The relative change in phase due to changes in sample height relative to the reference plane was determined by subtracting the absolute phase of the sample from the absolute phase of the reference plane. The relative phase for two additional planes with known heights relative to the original reference plane was also extracted. The coefficients for a proportional relationship between the relative phase and relative height were then established using the relative phase differences of the two reference planes with known relative height difference; this could then be determined for every pixel location on the image:

$$\frac{1}{h(x,y)} = a(x,y) + b(x,y)\frac{1}{\phi(x,y)} \tag{5.1}$$

The coefficients, $\boldsymbol{a}(\boldsymbol{x},\boldsymbol{y})$ and $\boldsymbol{b}(\boldsymbol{x},\boldsymbol{y})$, describe the pixel-specific relationship between height $\boldsymbol{h}(\boldsymbol{x},\boldsymbol{y})$ and phase $\boldsymbol{\phi}(\boldsymbol{x},\boldsymbol{y})$. Subsequently, the height map for the sample was extracted by plugging the phase values of each location into **EQ 5.1**. The 3D-printed mockup-**BHV** was used for determining height resolution and demonstrated that a modest spatial frequency of 0.3 mm^{-1} resulted in a height resolution of $< 100\ \mu m$.

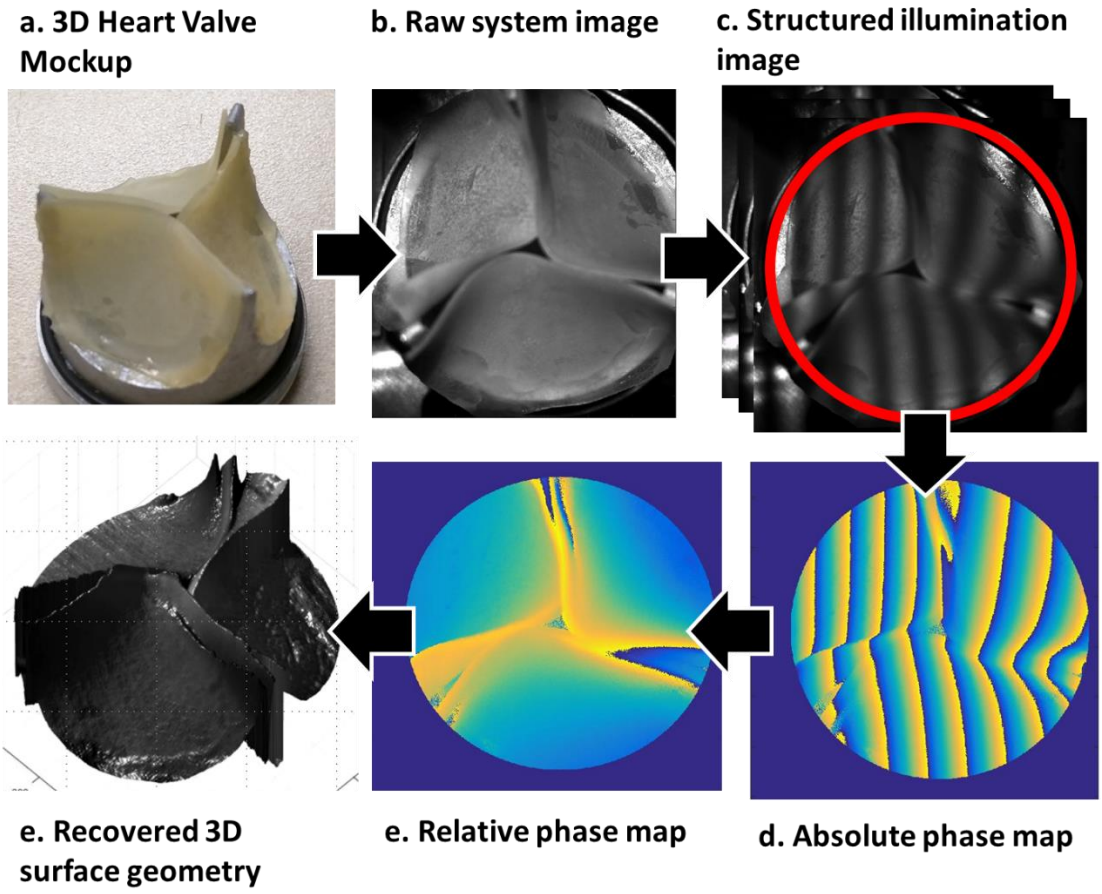

Figure 5.5: Demonstration of 3D-profilometry workflow using a 3D heart-valve mockup, achieving a height resolution of greater than 100 μm.

A surgical-grade mitral **BHV** (Hancock II T510, size 29 mm, Medtronic) was utilized for imaging. Immediately after **pSFDI** imaging and phase-extraction, the

calibration planes were measured with known relative distances from the sample to extract the $\boldsymbol{a}(\boldsymbol{x},\boldsymbol{y})$ and $\boldsymbol{b}(\boldsymbol{x},\boldsymbol{y})$ coefficients for direct height mapping.

5.4.3 Results

Figure 5.6 depicts the raw BHV image from the system perspective and the recovered 3D topology maps. The surface profile of the sample height was rendered as a 3D surface with a Gaussian filter applied to reduce noise. Surface shading described the recovered $\boldsymbol{NOI}$.

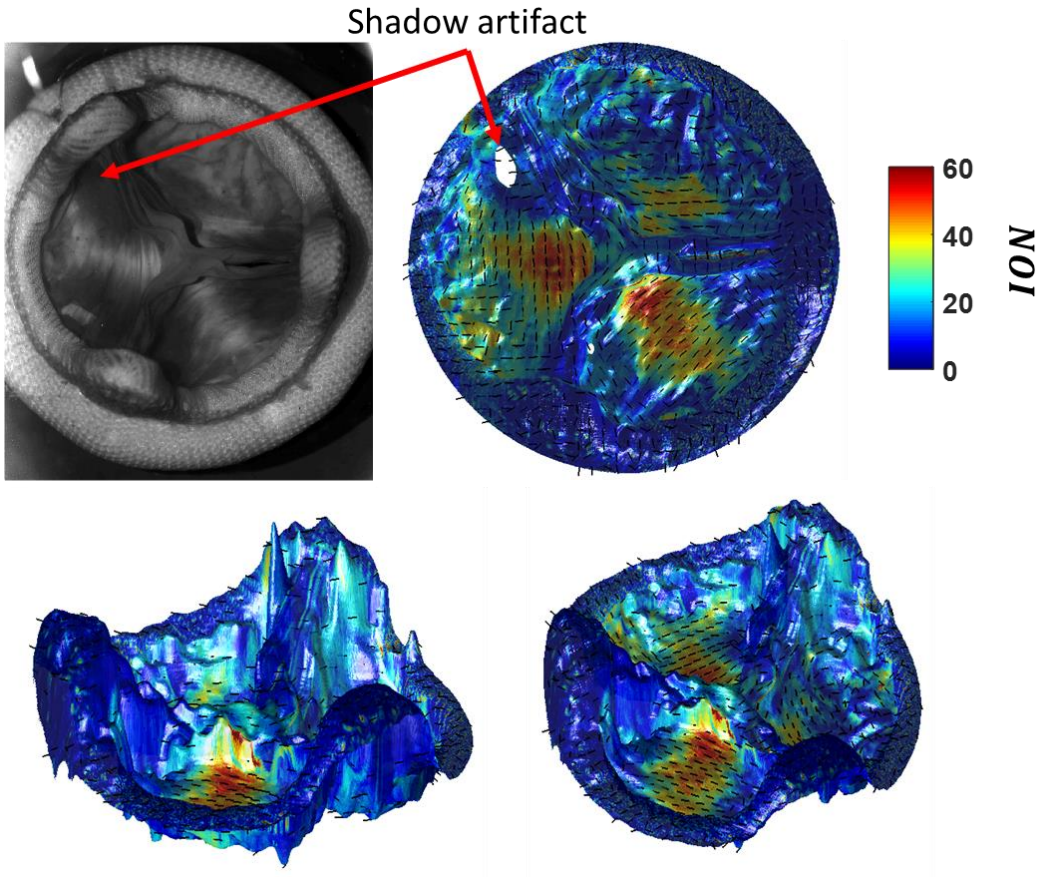

Figure 5.6: Extracted pSFDI and phase profilometry data, demonstrating the capability to extract fiber microstructure maps from an intact 3D-tissue geometry. Shadow artifacts suggest that multiple angles of acquisition may be necessary for samples with rugged geometry.

Fiber orientation was represented by quiver plots overlaid at sparse points across the sample surface. The fiber alignment was high in the belly region of the valve leaflets, as expected, and the fibers were aligned appropriately relative to expected physiological orientations. In some areas of extreme height differences, shadows restricted the ability to extract accurate phase changes. An example of a shadow artifact that was manually removed is depicted in the sample. These artifacts were removed manually where possible.

5.4.4 Discussion

Although the preliminary results were promising, several potential improvements could have been implemented. Firstly, areas of shadowing occurred due to the surface geometry that resulted in difficulties in the recovering phase, which subsequently distorted the heights recovered in areas of shadow. While these were manually current for this sample, improvements could be enabled by imaging the sample at three different angles, such that in each image set, one leaflet is fully exposed to the illumination of the system.

Secondly, the effect of surface topology on the polarized light signal should be investigated. Surface areas which are out-of-plane of the imaging system do not adhere to the assumptions of in-plane fiber geometry relative to the system geometry. Therefore, the extracted $\boldsymbol{NOI}$ metric may be regionally inaccurate. Two potential improvements could be implemented to ensure that the measurements are accurate. First, a height- and surface-angle empirical calibration could be conducted, similar to one by Gioux et al., to correct optical properties extracted with **SFDI** for uneven surface topology (Gioux, Mazhar et al. 2009). In summary, a fiber phantom with known alignment could be imaged as its height and tilt in both axes is changed. Changes in the **pSFDI** signal could then be empirically corrected as a function of height and angle. A second, more exhaustive correction method would entail modeling a range of collection angles (**Chapter 4**). However, this method

would disallow the use of a linearized fitting model; this would result in significantly more computationally-expensive fitting times of approximately days for high-resolution images.

5.5 SUMMARY

This chapter has demonstrated the utility of **pSFDI** for imaging collagen structure in multi-layered native and bioprosthetic heart valve leaflet tissues. In static imaging, pSFDI provided results which are comparable to an existing gold standard (SALS) with additional sensitivity to layered fiber architecture. This offers a rapid method for evaluating the heterogeneous, multi-layered fiber microstructure in both native and bioprosthetic valve leaflet materials.

The non-destructive nature of and improvements in imaging speed of **pSFDI** render the technique readily compatible with existing tissue mechanical analyses; this allows controlled dynamic study of local fiber kinematics across large fields of view at multiple time points. This research has yielded evidence of two fiber kinematic phenomena, fiber recruitment and collagen fiber uncrimping, which have large implications for understanding microstructural contributions to tissue- and organ-level scales of dynamic function. Additionally, changes in fiber structure near suture points in the samples provide insights into the boundary conditions used in the computational modeling of biaxial tissue mechanics.

Finally, the **3D-pSFDI** experiment provided a proof-of-concept for future research in assessing fiber structure in intact valves without excising the tissues. This ability promises tremendous impact in terms of studying the long-term fiber kinematics in **BHV**s, since fiber structure in individual **BHV** leaflets could be studied at multiple time points, rather than merely endpoints. Additionally, it could be applied to assess the changes in **TAVR** valves before and after they are packed into a small lumen for catheter delivery. This is a particularly important area of study which could contribute to the adoption of TAVR as a reliable alternative to the current gold standard invasive valve replacement surgeries.

Chapter 6: Conclusion

This dissertation elucidates the use of light-scattering to probe tissue microstructures that are directly related to physiological state and condition of tissues. This was achieved by developing theoretical models which indicate how spatially-modulated and polarized light scatter from spheres and cylinders, which represent common tissue microstructures of interest. The primary benefits to the described models included increasing processing speed and more direct interpretation of light-scattering measurements in terms of tissue microstructure. Overall, this will allow rapid, non-destructive mapping of tissue microstructure across tissue- and organ-level spatial and temporal scales.

The novel empirical model of sub-diffuse reflectance imaged with **sd-SFDI** provides substantial speed improvements relative to existing non-linear models and lookup tables. This increased processing speed is crucial to incorporating **sd-SFDI** as a surgical guidance tool in tissue-conserving surgeries, in which mapping of tumor boundaries requires extensive tissue preparation times. This research has demonstrated the ability to extract model parameters that were directly sensitive to changes in the scattering particle size of cells and nuclei. Furthermore, this was translated into identifying regions of increased cellular proliferation in tissue samples from Mohs micrographic surgery, which matched the results from similar studies of tumors in breast tissues. To our knowledge, this is the first report of using sub-diffuse scattering to characterize skin cancer lesions from Mohs micrographic surgery. Ultimately, this technique could be used to directly determine tumor boundaries or as a screening tool to reduce search areas for complimentary diagnostic techniques so that they can improve clinical workflows.

One of the primary limitations of the **sd-SFDI** work is the lack of an established sub-diffuse reflectance model for directly extracting the $\boldsymbol{\gamma}$ parameter from our

measurements. This was primarily due to challenges in establishing the system-specific coefficients required for the semi-empirical Kanick model to accurately extract optical properties. Fitting these coefficients was rendered difficult by the complexity of the model, which resulted in many local minima fits that did not allow for accurate optical property extraction from the microbead phantoms with known scattering properties. Due to the increased flexibility and optical property range, a Monte Carlo model incorporating sub-diffuse scattering parameters has been suggested as a reference model for future research.

Additionally, the particles used in the TiO_2 reflectance standard were not well-defined or easily quantified. This indicated that while the standard could be used to negate the impact of pixel-specific **MTF** of the system (such as spatial variance in illumination intensity), it could not be used directly as the required reference measurement that is generally used in inverse models. A new standard with a known scattering particle size distribution should be constructed for future reference measurements. Furthermore, research has already been initiated concerning a fixed-geometry imaging system which can achieve high spatial frequency ranges. An extended set of 20 **MMS** samples has also been collected for imaging and will be accompanied by more extensive demarcations of tumor and normal tissue regions from a trained physician. This increased number of samples and known sample regions will allow assessment of intra- and inter-patient variance of light scattering measurements from different tissue regions. Finally, a long-term objective is to investigate the ability of this technique to map microstructure onto *in vivo* tumor lesions, allowing tumor boundaries to be determined prior to surgical resection.

The primary impact of our polarized light-imaging research was to allow extraction of absolute measures of fiber alignment from optical anisotropy. Previous methods have typically inferred relative fiber alignment, which limited comparisons of alignment measurements with single data sets. The combined **pSFDI** technique demonstrated multi-

layer fiber alignment discrimination in thin ($< 1mm$) tissue samples. Additionally, the speed of imaging allowed the pseudo-dynamic imaging of collagen fiber kinematics during tissue deformation, which provided a powerful means for examining the contributions of local fiber microstructure to macroscopic tissue function.

Although the imaging speed ($< 5s$) was adequate for pseudo-dynamic imaging, there may be short-term fiber kinematics related to stress-relaxation and creep in the tissues. Improvements to the system will primarily be offered by the possibility of the hardware synchronization of the projector and camera, which was a major limitation to the imaging speed. This hardware triggering scheme is expected to achieve a total imaging time of less than one second based on the minimum exposure times necessary for the camera and projector.

Two fiber kinematic phenomena, including fiber recruitment and collagen uncrimping, were inferred from data collected during dynamic tissue studies. However, more comprehensive studies are planned for assessing the translation of these fiber kinematics into mechanical performance. In addition to these insights, the **pSFDI** data is currently being utilized to provide a texture for digital image correlation (DIC) to recover local strain fields; this enables local microstructure and strains to be assessed in relation to the large-scale tissue mechanical behavior. This permits assessment of the contributions of microstructural heterogeneity, either from native tissue and damaged tissues, to both short-term mechanical performance and long-term tissue remodeling. Since tissues do not need to be sacrificed during imaging, fiber architecture changes during accelerated wear-testing can be mapped at multiple times. Specifically, this technique facilitates the investigation of the accuracy of the affine fiber kinematic assumptions that are adopted in structural constitutive models of microscale fiber contributions to macroscopic tissue deformations.

The validation of the **3D-pSFDI** technique would further permit imaging of entire **BHV**s during testing without the need for sacrificing the entire valve. However, future research assessing the impact of surface topography on the extracted **pSFDI** alignment metrics must first be explored. This could be achieved in two ways: either by experimental calibration or by additional modeling. A calibration technique similar to that for single-snapshot optical property extraction could be used to correct for sample topography (Gioux, Mazhar et al. 2009). However, for **pSFDI**, this calibration would need to be considerably more involved, as both the topographical information as well as the fiber orientation must be taken into account. Alternatively, a fiber-model with non-normal incidence could be considered. However, this would still necessitate the incorporation of both fiber orientation as well as surface topography into the inverse model to extract correct optical properties. Both such techniques are likely to have extensive processing times for each data set, which would be highly non-linear.

Appendices

APPENDIX A: TITANIUM DIOXIDE (TiO_2) REFERENCE STANDARD

A.1 Fabrication

A 13 cm X 13 cm X 3 cm cuboid mold was $3D$ printed for the phantom to cure in. A full 500g bottle of Sylgard 184 PDMS Silicone (Ellsworth Adhesives, Germantown WI) and 1 g of $d < 5\mu m$ TiO_2 particles (Sigma Aldrich, St. Louis MO) were used to create a 2mg/g mix ratio of scattering particles to base. The particles were mixed into the silicone curing agent by hand in a small flask, then sonicated for 10 minutes. The cure/particle mix was then mixed into the silicone base for 10 minutes by hand and sonicated for another 10 minutes. The resulting mixture was then poured into the mold and subjected to a vacuum of -20 $mmHg$ before rapidly purging to atmospheric pressure. This process was repeated 20 times to reduced bubble formation in the mold. The mix was then cured for three days at room temperature conditions to further ensure bubbles had time to dissipate.

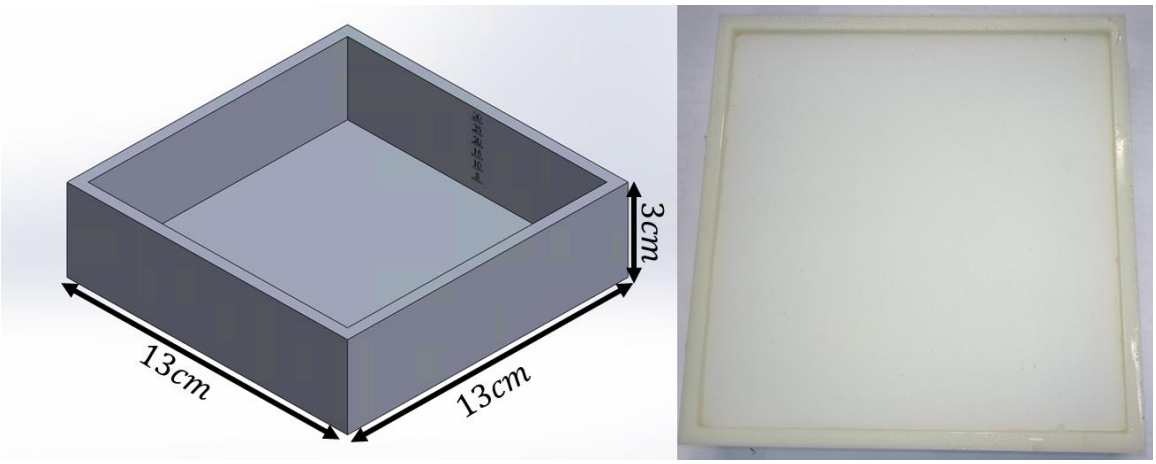

Figure A.1: Diffuse reflectance standard mold (left) and final appearance (right).

After curing, the surface of the sample was sanded with 200 grit sandpaper across the surface, rinsed with water, and sanded with a 400 grit sandpaper to remove the majority of specular reflections from the surface. The standard was then washed once more, dried, and packing tape was used to remove any remaining free particles on the surface.

A.2 Reflectance Characterization

Images of a calibrated 20% reflectance standard and the TiO_2 reflectance standard were captured under identical lighting conditions at $450\ nm$, $530\ nm$, and $620\ nm$ (the center wavelengths of the projection system LEDs). Both image sets were median filtered with a $25\ X\ 25$ pixel window. The average diffuse reflectance was calculated for each wavelength, as shown in the graph and table below.

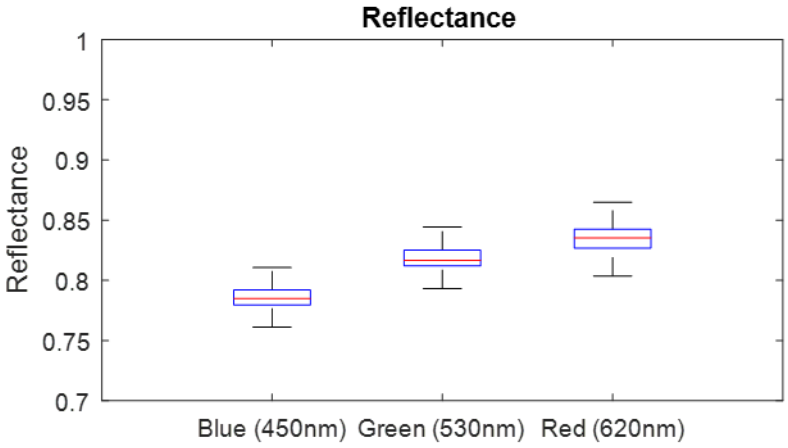

Reflectance	Blue	Green	Red
Mean (Std. Dev)	78.9% (1.7%)	82.1% (1.7%)	83.6% (1.8%)

Figure A.2: TiO_2 standard mean reflectance and variance at each projector wavelength/

A.3 TiO_2 Particle Size Analysis

Although we achieved good reflectance values, attempts to calculate the reduced scattering coefficient were hampered by the large and difficult to quantify polydispersity of the particle sizes, although dynamic light scattering, scanning electron microscopy, and tunneling electron microscopy were all considered. Scanning electron microscopy images highlight this issue (**Figures A.3-A.5**). For future studies, a reflectance standard with a well-defined particle size distribution would be useful for reference measurements in **sd-SFDI** studies, as the Mie calculations for reduced scattering coefficients would be tractable.

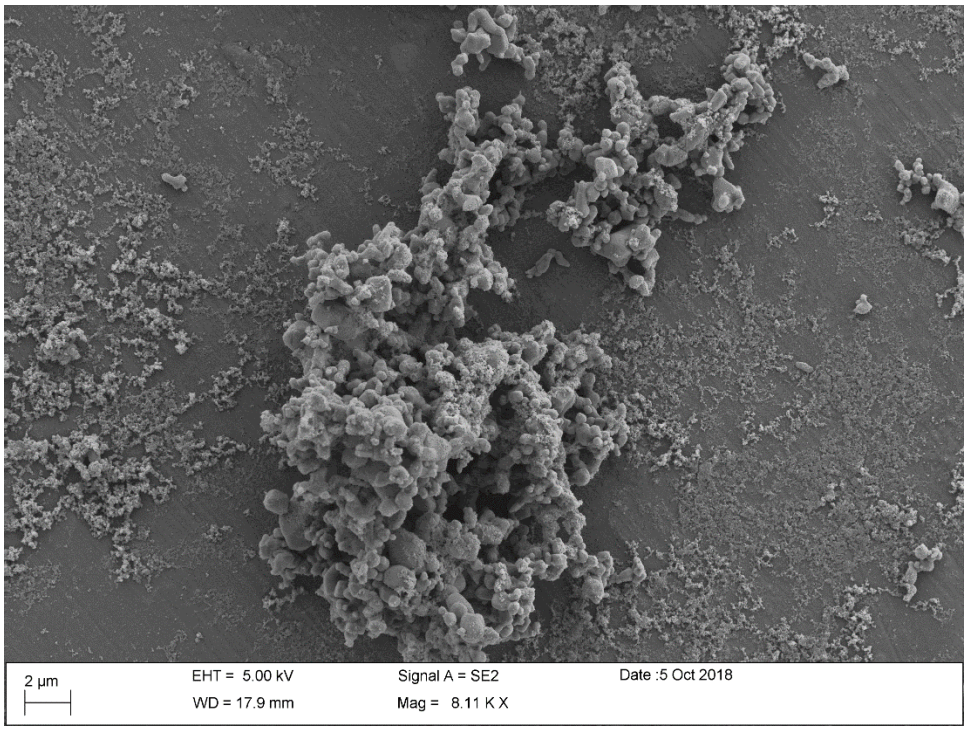

Figure A.3: SEM images of TiO_2 particles, indicating high polydispersity.

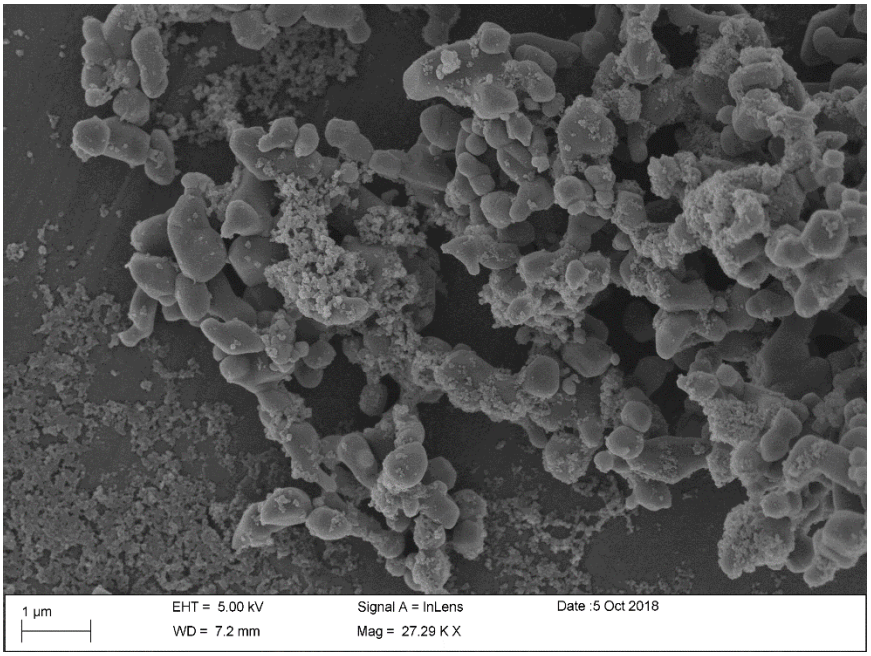

Figure A.4: SEM images of TiO_2 particles, indicating high polydispersity.

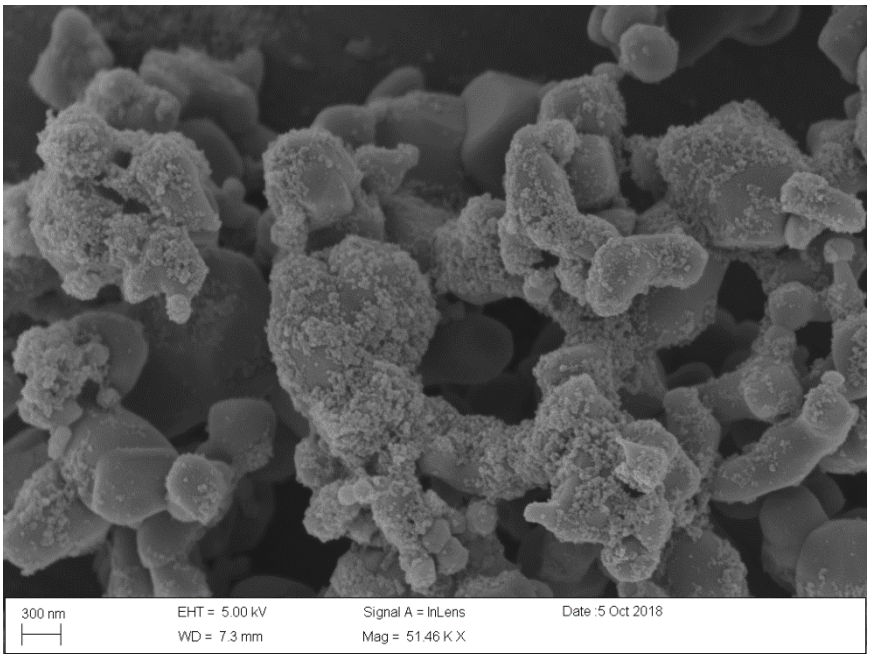

Figure A.5: SEM images of TiO_2 particles, indicating high polydispersity.

APPENDIX B: SCATTERING BEAD PHANTOM CALCULATIONS

Mie scattering theory was used to calculate the average scattering efficiencies of three particle size distributions corresponding to calibrated polystyrene microspheres (Polysciences Inc., Warrington PA). The diameters of the beads were: $\overline{d_1} = 0.0878\ \mu m\ (SD: 0.01 \mu m)$, $\overline{d_2} = 0.19\ \mu m\ (SD: 0.01\ \mu m)$, $\overline{d_3} = 0.99\ \mu m\ (SD: 0.03\ \mu m)$. Using the listed concentrations for each bead distribution, two dilutions of each size bead in distilled water was formulated so that a reduced scattering coefficient of $\boldsymbol{\mu_s'(\lambda = 530\ nm) =}\ 2\ mm^{-1}$ and $3\ mm^{-1}$ were achieved for each bead size. The reduced scattering coefficient, anisotropy parameter (**g**), and sub-diffuse anisotropy parameter ($\boldsymbol{\gamma}$) were then calculated for each wavelength ($\boldsymbol{\lambda} = 450\ nm, 530\ nm, 620\ nm$).

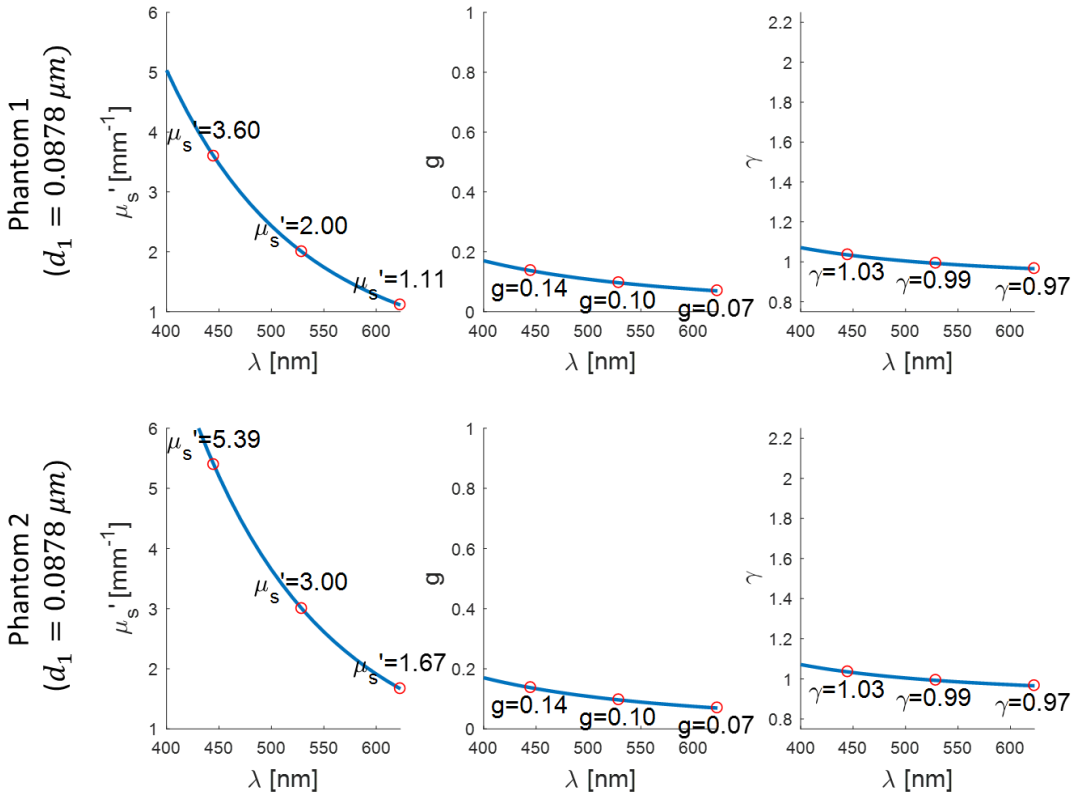

Figure B.1: Mie calculations of ~100 *nm* bead optical scattering parameters.

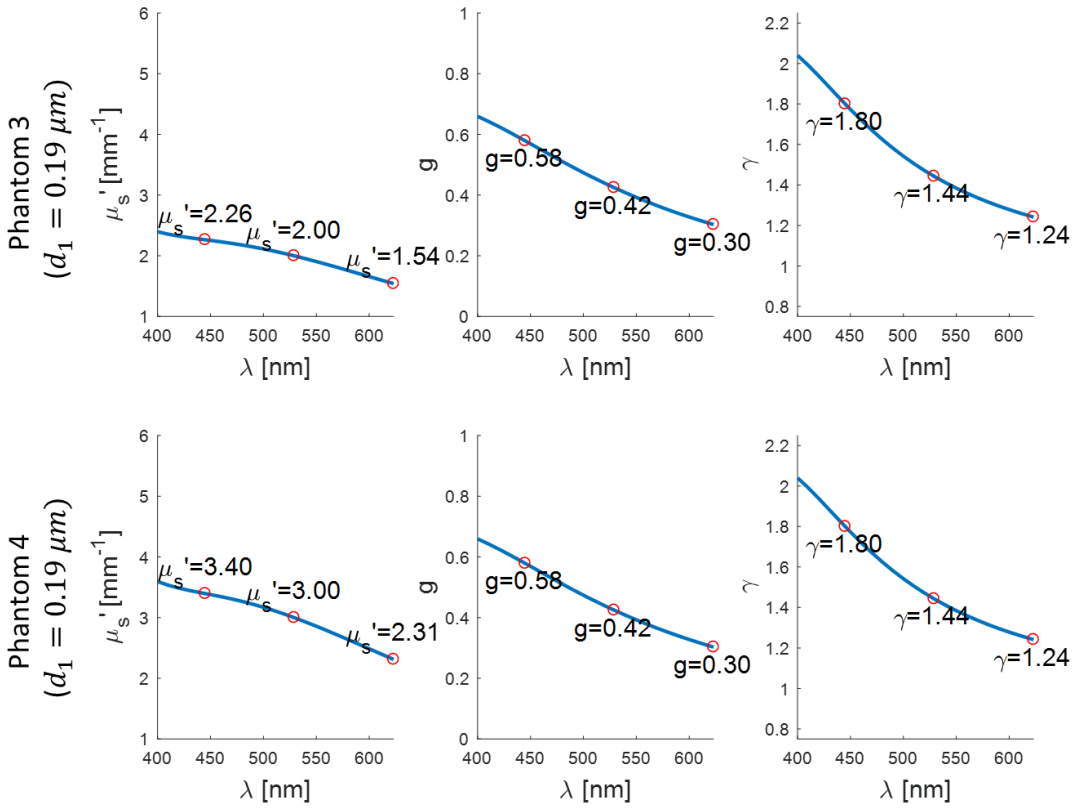

Figure B.2: Mie calculations of $\sim 200\ nm$ bead optical scattering parameters.

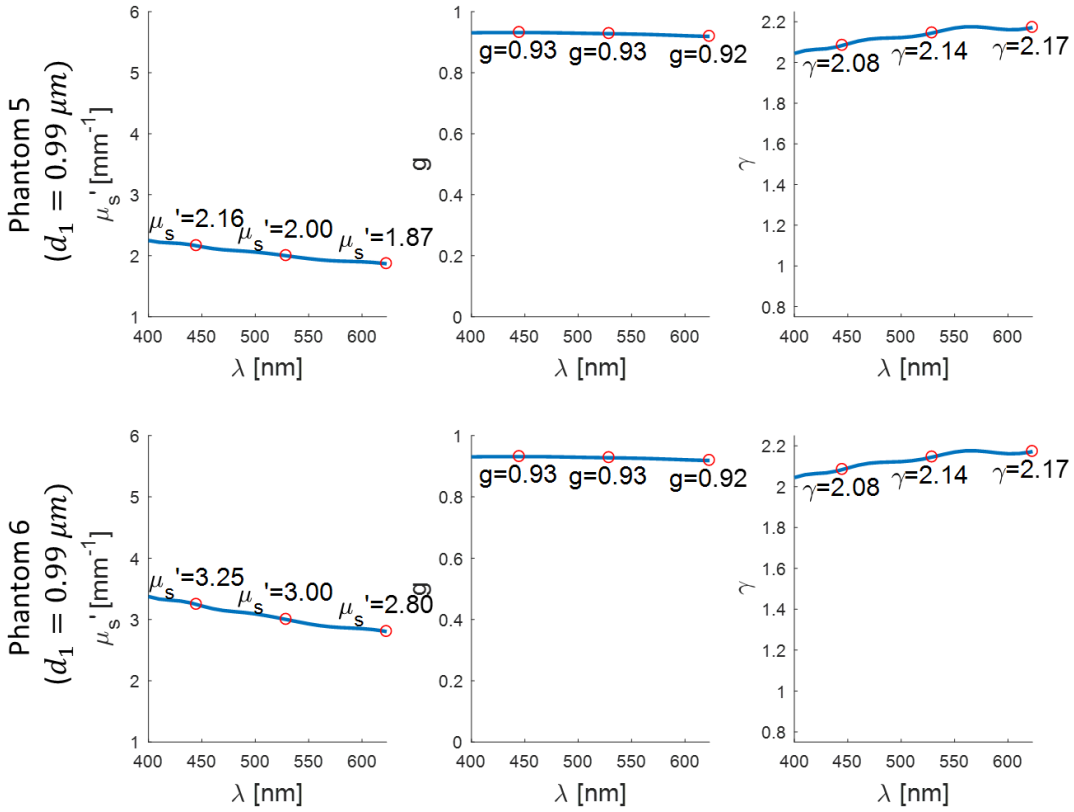

Figure B.3: Mie calculations of ~1 μm bead optical scattering parameters.

APPENDIX C: MUELLER MATRIX FORMALISM FOR CO-POLARIZATION IMAGING SYSTEM

The full derivation of our polarized light model begins from **EQ 4.6**:

$$\vec{S}_{out} = \tau_{sys} M_p R_p\big(-(\theta \pm \varphi)\big) M_s R_p\big((\theta \pm \varphi)\big) M_p \vec{S}_{in} \qquad \textbf{(4.7)}$$

The initial Stokes vector describing the incident light ($\boldsymbol{\vec{S}_{in}}$), along with the Mueller matrix components representing the polarizer ($\boldsymbol{M_p}$) and rotational transformations ($\boldsymbol{R_p}$), are defined as follows:

$$\vec{S}_{in} = \begin{pmatrix} 1 \\ 0 \\ 0 \\ 0 \end{pmatrix} \qquad \textbf{(C.1)}$$

$$M_p = \frac{1}{2}\begin{pmatrix} 1 & 1 & 0 & 0 \\ 1 & 1 & 0 & 0 \\ 0 & 0 & 0 & 0 \\ 0 & 0 & 0 & 0 \end{pmatrix} \qquad \textbf{(C.2)}$$

$$R_p\big((\theta \pm \varphi)\big) = \begin{pmatrix} 1 & 0 & 0 & 0 \\ 0 & cos\big(2(\theta \pm \varphi)\big) & sin\big(2(\theta \pm \varphi)\big) & 0 \\ 0 & -sin\big(2(\theta \pm \varphi)\big) & -cos\big(2(\theta \pm \varphi)\big) & 0 \\ 0 & 0 & 0 & 1 \end{pmatrix} \qquad \textbf{(C.3)}$$

The Mueller matrix for the sample ($\boldsymbol{M_s}$) is given as the special case scattering $\boldsymbol{T}$-matrix derived for normally incident light scattering from infinitely long cylinders:

$$M_s = \begin{bmatrix} M_{11} & M_{12} & M_{13} & M_{14} \\ M_{21} & M_{22} & M_{23} & M_{24} \\ M_{31} & M_{32} & M_{33} & M_{34} \\ M_{41} & M_{42} & M_{43} & M_{44} \end{bmatrix} = \frac{2}{\pi x}\begin{bmatrix} T_{11} & T_{12} & 0 & 0 \\ T_{12} & T_{11} & 0 & 0 \\ 0 & 0 & T_{33} & T_{34} \\ 0 & 0 & -T_{34} & T_{33} \end{bmatrix} \qquad \textbf{(C.4)}$$

The full solution for the $\boldsymbol{T}$-matrix elements, along with efficient computational algorithms, has been described extensively by Bohren & Huffman. The inputs required to solve for $\boldsymbol{T_{11}}$, $\boldsymbol{T_{12}}$, $\boldsymbol{T_{33}}$, and $\boldsymbol{T_{34}}$are the relative refractive index of the cylinder and the medium ($\boldsymbol{m}$), the size parameter ($\boldsymbol{x}$), and the system collection angles ($\boldsymbol{\psi}$). Plugging **EQ C.1 – C.4** into **EQ 4.6** can be shown to simplify to:

$$\vec{S}_{out} = \frac{\tau_{sys}}{4}\begin{bmatrix} M_{11}(1+\cos^2(2(\theta \pm \varphi))) + 2M_{12}\cos(2(\theta \pm \varphi)) + M_{33}\sin^2(2(\theta \pm \varphi)) \\ M_{11}(1+\cos^2(2(\theta \pm \varphi))) + 2M_{12}\cos(2(\theta \pm \varphi)) + M_{33}\sin^2(2(\theta \pm \varphi)) \\ 0 \\ 0 \end{bmatrix}$$

(C.5)

EQ C.5 shows that the intensity response detected by the camera is now entirely dependent on the linear polar response, and the Stokes vector can therefore be collapsed into **EQ 4.7**.

APPENDIX D: LINEARIZED FITTING MODEL FOR PSFDI

To allow more rapid fitting, a modified but mathematically identical form of **EQ 4.7** is used. Each sinusoidal term includes a non-linear phase offset. For linearized fitting, it is transformed using the identity $\boldsymbol{a \cdot \sin(\theta) + b \cdot \cos(\theta) = c \cdot \cos(\theta + \varphi)}$, where $\boldsymbol{c = \sqrt{a^2 + b^2}}$) and $\boldsymbol{\varphi = atan2(a, b)}$. This results in a Fourier expansion form of **EQ 4.7**:

$$I(\theta) = a_0 + b_1 \sin(2\theta) + b_2 \cos(2\theta) + b_3 \sin(4\theta) + b_4 \cos(4\theta) \qquad \textbf{(D.1)}$$

In this form, a linearized representation of the reflectance is $\boldsymbol{I = Sb}$, where $\boldsymbol{I}$ is the detected reflectance intensity, $\boldsymbol{S}$ is the Fourier expansion representation of the model in **EQ D.1**, and $\boldsymbol{b}$ is a vector containing the five transformed model coefficients from **EQ D.1**. Solving this system of equations by $\boldsymbol{b = S\backslash I}$ allows extraction of the coefficients by Gaussian elimination (Matlab function *mldivide*). Subsequently, a 1 second fitting time was achieved for a 1.5 −megapixel image, compared to several hours with the *lsqnonlin* fitting algorithms for the original equation containing a non-linear phase offset term. After fitting, the original form of the model coefficients and phase offset were recovered using the same identities. A custom Matlab script, *PSFDI_fitting.m*, will return the coefficients $\boldsymbol{a_0}$, $\boldsymbol{a_2}$, $\boldsymbol{a_4}$, the primary fiber direction $\boldsymbol{\varphi}$, and the resulting fit curve for a given input image data set whose first two dimensions are spatial axes ($\boldsymbol{X, Y}$) and third dimension is polarizer angle ($\boldsymbol{\theta}$).

APPENDIX E: CUSTOM ELECTROSPINNING MANDREL SYSTEM

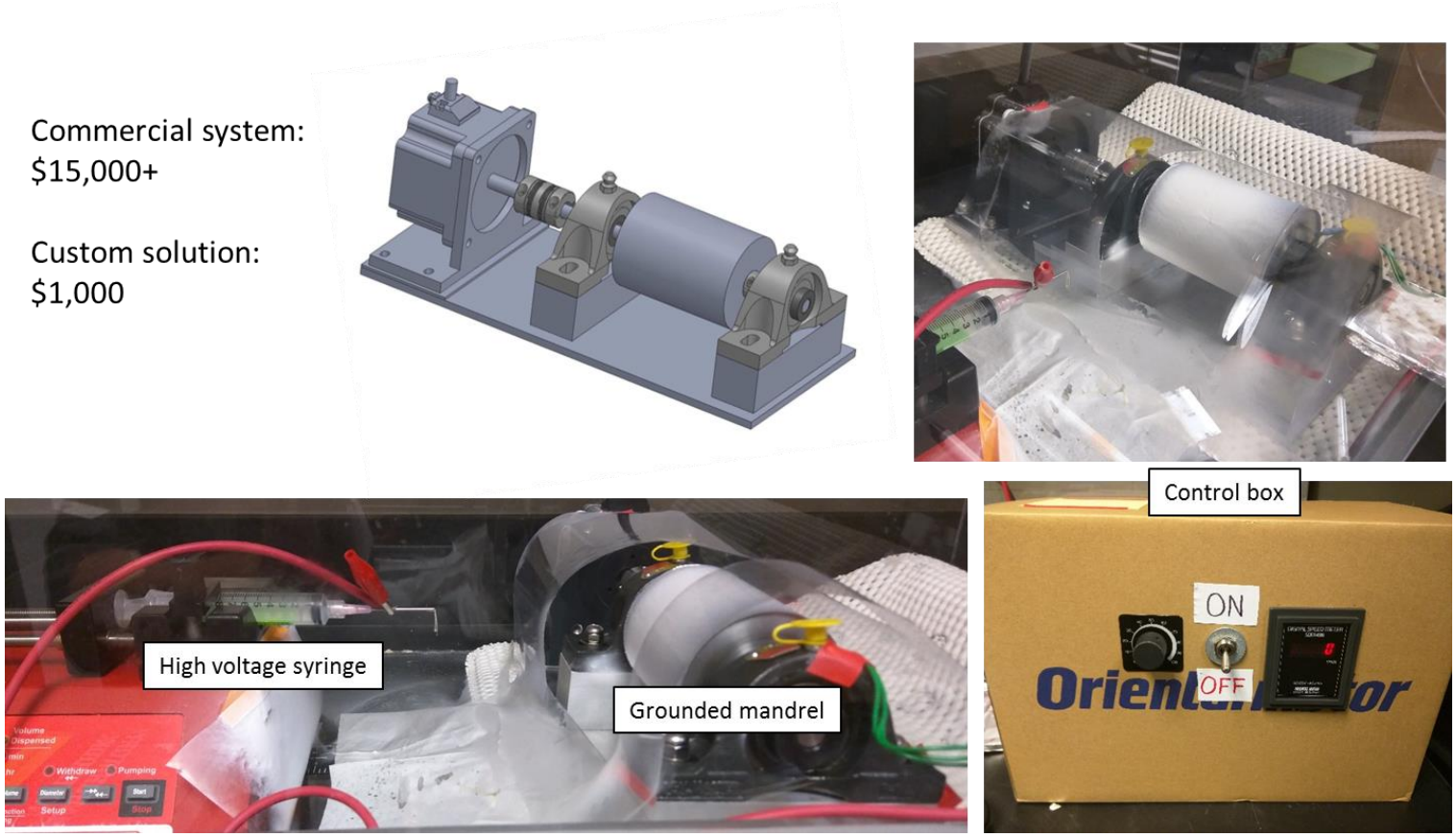

Figure E.1: Custom electrospinning mandrel design.

APPENDIX F: FIBER ORIENTATION ANALYSIS FROM SEM IMAGES

The process of processing SEM images of electrospun fibers to extract the orientation distribution function (***ODF***) is outlined in **Figure F.1**, and is based on a method described by Mega *et al*. The custom Matlab function *PSFDI_megaODF* can be used to extract the normalized ***ODF*** from any input image. The bandpass filter low frequency cutoff was set to $3\ [1/pixels]$, the Gaussian maximum frequency cutoff was set to $4X$ the low frequency cutoff, and the median filter was set to $3X3$ pixels for the processed data in this work.

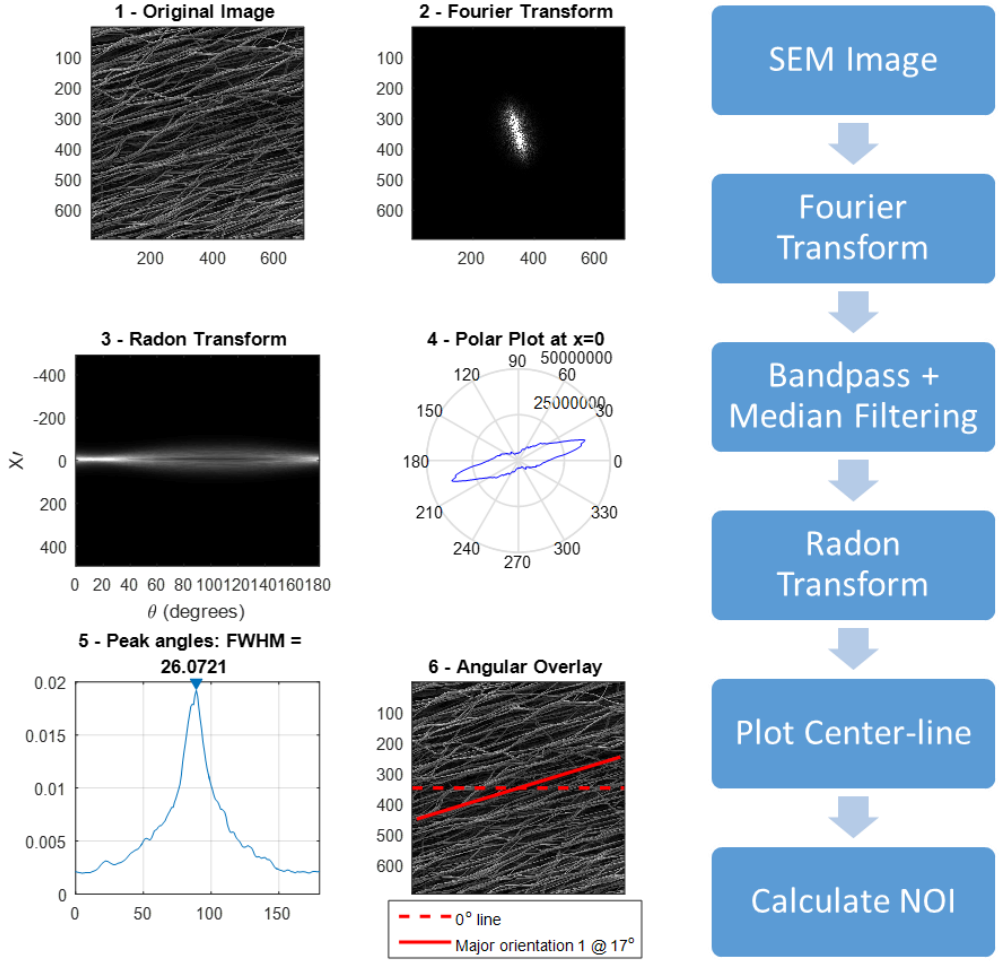

Figure F.1: Orientation analysis of fibers in SEM images.

References

Adams, S. B., M. J. Roberts, N. A. Patel, S. Plummer, J. Rogowska, D. L. Stamper, J. G. Fujimoto and M. E. Brezinski (2002). The use of polarization sensitive optical coherence tomography and elastography to assess connective tissue. Conference on Lasers and Electro-Optics, 2003. CLEO'03.

Aggarwal, A., V. S. Aguilar, C.-H. Lee, G. Ferrari, J. H. Gorman, R. C. Gorman and M. S. Sacks (2013). Patient-specific modeling of heart valves: from image to simulation. International Conference on Functional Imaging and Modeling of the Heart, Springer.

Allen, A. C., E. Barone, O. Cody, K. Crosby, L. J. Suggs and J. Zoldan (2017). "Electrospun poly (N-isopropyl acrylamide)/poly (caprolactone) fibers for the generation of anisotropic cell sheets." Biomaterials science **5**(8): 1661-1669.

Amoroso, N. J., A. D'Amore, Y. Hong, W. R. Wagner and M. S. Sacks (2011). "Elastomeric electrospun polyurethane scaffolds: the interrelationship between fabrication conditions, fiber topology, and mechanical properties." Advanced Materials **23**(1): 106-111.

Angelo, J., C. R. Vargas, B. T. Lee, I. J. Bigio and S. Gioux (2016). "Ultrafast optical property map generation using lookup tables." Journal of biomedical optics **21**(11): 110501.

Angelo, J. P., S.-J. Chen, M. Ochoa, U. Sunar, S. Gioux and X. Intes (2018). "Review of structured light in diffuse optical imaging." Journal of biomedical optics **24**(7): 071602.

Angelo, J. P., M. van de Giessen and S. Gioux (2017). "Real-time endoscopic optical properties imaging." Biomedical optics express **8**(11): 5113-5126.

Angelo, J. P., V. Venugopal, F. Fantoni, V. Poher, I. J. Bigio, L. Herve, J.-M. Dinten and S. Gioux (2014). "Depth-enhanced fluorescence imaging using masked detection of structured illumination." Journal of biomedical optics **19**(11): 116008.

Ayoub, S., K. C. Tsai, A. H. Khalighi and M. S. Sacks (2018). "The Three-Dimensional Microenvironment of the Mitral Valve: Insights into the Effects of Physiological Loads." Cellular and Molecular Bioengineering **11**(4): 291-306.

Badea, C. T., B. Fubara, L. W. Hedlund and G. A. Johnson (2005). "4-D micro-CT of the mouse heart." Molecular Imaging **4**(2): 15353500200504187.

Balas, C. (2009). "Review of biomedical optical imaging—a powerful, non-invasive, non-ionizing technology for improving in vivo diagnosis." Measurement science and technology **20**(10): 104020.

Bashkatov, A. N., E. A. Genina, V. I. Kochubey and V. V. Tuchin (2000). Estimation of wavelength dependence of refractive index of collagen fibers of scleral tissue. EOS/SPIE European Biomedical Optics Week, International Society for Optics and Photonics.

Bevilacqua, F. and C. Depeursinge (1999). "Monte Carlo study of diffuse reflectance at source–detector separations close to one transport mean free path." JOSA A **16**(12): 2935-2945.

Billiar, K. and M. Sacks (1997). "A method to quantify the fiber kinematics of planar tissues under biaxial stretch." Journal of biomechanics **30**(7): 753-756.

Billiar, K. L. and M. S. Sacks (2000). "Biaxial mechanical properties of the native and glutaraldehyde-treated aortic valve cusp: part II—a structural constitutive model." Journal of biomechanical engineering **122**(4): 327-335.

Billiar, K. L. and M. S. Sacks (2000). "Biaxial mechanical properties of the natural and glutaraldehyde treated aortic valve cusp—part I: experimental results." Journal of biomechanical engineering **122**(1): 23-30.

Bloom, W., D. W. Fawcett and A. A. Maximow (1962). "Textbook of histology."

Boas, D. A., C. Pitris and N. Ramanujam (2016). Handbook of biomedical optics, CRC press.

Bodenschatz, N., P. Krauter, A. Liemert and A. Kienle (2016). "Quantifying phase function influence in subdiffusively backscattered light." Journal of biomedical optics **21**(3): 035002.

Bodenschatz, N., P. Krauter, A. Liemert, J. Wiest and A. Kienle (2015). "Model-based analysis on the influence of spatial frequency selection in spatial frequency domain imaging." Applied Optics **54**(22): 6725-6731.

Bodenschatz, N., P. Krauter, S. Nothelfer, F. Foschum, F. Bergmann, A. Liemert and A. Kienle (2015). "Detecting structural information of scatterers using spatial frequency domain imaging." Journal of biomedical optics **20**(11): 116006-116006.

Bohren, C. F. and D. R. Huffman (2008). Absorption and scattering of light by small particles, John Wiley & Sons.

Brakenhoff, G., H. Voort, E. Spronsen and N. Nanninga (1989). "Three-dimensional imaging in fluorescence by confocal scanning microscopy." Journal of microscopy **153**(2): 151-159.

Brenner, D. J. and C. D. Elliston (2004). "Estimated Radiation Risks Potentially Associated with Full-Body CT Screening 1." Radiology **232**(3): 735-738.

Brenner, D. J., C. D. Elliston, E. J. Hall and W. E. Berdon (2001). "Estimated risks of radiation-induced fatal cancer from pediatric CT." American journal of roentgenology **176**(2): 289-296.

Brezinski, M. E. (2006). Optical coherence tomography: principles and applications, Academic press.

Brown, E., T. McKee, A. Pluen, B. Seed, Y. Boucher and R. K. Jain (2003). "Dynamic imaging of collagen and its modulation in tumors in vivo using second-harmonic generation." Nature medicine **9**(6): 796-800.

Budnev, V., I. Ginzburg, G. Meledin and V. Serbo (1975). "The two-photon particle production mechanism. Physical problems. Applications. Equivalent photon approximation." Physics Reports **15**(4): 181-282.

Carleton, J. B., A. D'Amore, K. R. Feaver, G. J. Rodin and M. S. Sacks (2015). "Geometric characterization and simulation of planar layered elastomeric fibrous biomaterials." Acta biomaterialia **12**: 93-101.

Carp, S. A., S. A. Prahl and V. Venugopalan (2004). "Radiative transport in the delta-P1 approximation: accuracy of fluence rate and optical penetration depth predictions in turbid semi-infinite media." Journal of Biomedical Optics **9**(3): 632-648.

Case, K. M. and P. F. Zweifel (1967). "Linear transport theory."

Chamot, S., E. Migacheva, O. Seydoux, P. Marquet and C. Depeursinge (2010). "Physical interpretation of the phase function related parameter γ studied with a fractal distribution of spherical scatterers." Optics express **18**(23): 23664-23675.

Chenault, D. B. and R. A. Chipman (1993). "Measurements of linear diattenuation and linear retardance spectra with a rotating sample spectropolarimeter." Applied optics **32**(19): 3513-3519.

Cheong, W.-F., S. A. Prahl and A. J. Welch (1990). "A review of the optical properties of biological tissues." IEEE journal of quantum electronics **26**(12): 2166-2185.

Chue-Sang, J., N. Holness, M. Gonzalez, J. Greaves, I. Saytashev, S. Stoff, A. Gandjbakhche, V. V. Chernomordik, G. Burkett and J. C. Ramella-Roman (2018). "Use of Mueller matrix colposcopy in the characterization of cervical collagen anisotropy." Journal of biomedical optics **23**(12): 121605.

Clark, M. A., F. G. Duhay, A. K. Thompson, M. J. Keyes, L. G. Svensson, R. O. Bonow, B. T. Stockwell and D. J. Cohen (2012). "Clinical and economic outcomes after surgical aortic valve replacement in Medicare patients." Risk management and healthcare policy **5**: 117.

Cook, J. and J. A. Zitelli (1998). "Mohs micrographic surgery: a cost analysis." Journal of the American Academy of Dermatology **39**(5): 698-703.

Cothren, R., R. Richards-Kortum, M. Sivak Jr, M. Fitzmaurice, R. Rava, G. Boyce, M. Doxtader, R. Blackman, T. Ivanc and G. Hayes (1990). "Gastrointestinal tissue diagnosis by laser-induced fluorescence spectroscopy at endoscopy." Gastrointestinal Endoscopy **36**(2): 105-111.

Courtney, T., M. S. Sacks, J. Stankus, J. Guan and W. R. Wagner (2006). "Design and analysis of tissue engineering scaffolds that mimic soft tissue mechanical anisotropy." Biomaterials **27**(19): 3631-3638.

Cuccia, D. J., F. Bevilacqua, A. J. Durkin, F. R. Ayers and B. J. Tromberg (2009). "Quantitation and mapping of tissue optical properties using modulated imaging." Journal of biomedical optics **14**(2): 024012-024012-024013.

Cuccia, D. J., F. Bevilacqua, A. J. Durkin and B. J. Tromberg (2004). Depth-sectioned imaging and quantitative analysis in turbid media using spatially modulated illumination. Biomedical Topical Meeting, Optical Society of America.

Cuccia, D. J., F. Bevilacqua, A. J. Durkin and B. J. Tromberg (2005). "Modulated imaging: quantitative analysis and tomography of turbid media in the spatial-frequency domain." Opt. Lett **30**(11): 1354-1356.

D'Amore, A., J. A. Stella, W. R. Wagner and M. S. Sacks (2010). "Characterization of the complete fiber network topology of planar fibrous tissues and scaffolds." Biomaterials **31**(20): 5345-5354.

De Boer, J. F., T. E. Milner, M. J. van Gemert and J. S. Nelson (1997). "Two-dimensional birefringence imaging in biological tissue by polarization-sensitive optical coherence tomography." Optics letters **22**(12): 934-936.

De Boer, J. F., S. M. Srinivas, B. H. Park, T. H. Pham, Z. Chen, T. E. Milner and J. S. Nelson (1999). "Polarization effects in optical coherence tomography of various biological tissues." Selected Topics in Quantum Electronics, IEEE Journal of **5**(4): 1200-1204.

Degen, C., M. Poggio, H. Mamin, C. Rettner and D. Rugar (2009). "Nanoscale magnetic resonance imaging." Proceedings of the National Academy of Sciences **106**(5): 1313-1317.

Deitzel, J., J. Kleinmeyer, D. Harris and N. B. Tan (2001). "The effect of processing variables on the morphology of electrospun nanofibers and textiles." Polymer **42**(1): 261-272.

Denk, W., D. W. Piston and W. W. Webb (1995). Two-photon molecular excitation in laser-scanning microscopy. Handbook of biological confocal microscopy, Springer**:** 445-458.

Denk, W., J. H. Strickler and W. W. Webb (1990). "Two-photon laser scanning fluorescence microscopy." Science **248**(4951): 73-76.

Denk, W. and K. Svoboda (1997). "Photon upmanship: why multiphoton imaging is more than a gimmick." Neuron **18**(3): 351-357.

Dickinson, M., G. Bearman, S. Tille, R. Lansford and S. Fraser (2001). "Multi-spectral imaging and linear unmixing add a whole new dimension to laser scanning fluorescence microscopy." Biotechniques **31**(6): 1272-1279.

DiMarzio, C. A. (2011). Optics for engineers, Crc Press.

Ding, Z., H. Ren, Y. Zhao, J. S. Nelson and Z. Chen (2002). "High-resolution optical coherence tomography over a large depth range with an axicon lens." Optics Letters **27**(4): 243-245.

Dögnitz, N. and G. Wagnières (1998). "Determination of tissue optical properties by steady-state spatial frequency-domain reflectometry." Lasers in medical science **13**(1): 55-65.

Doornbos, R., R. Lang, M. Aalders, F. Cross and H. Sterenborg (1999). "The determination of in vivo human tissue optical properties and absolute chromophore concentrations using spatially resolved steady-state diffuse reflectance spectroscopy." Physics in medicine and biology **44**(4): 967.

Doshi, J. and D. H. Reneker (1993). Electrospinning process and applications of electrospun fibers. Industry Applications Society Annual Meeting, 1993., Conference Record of the 1993 IEEE, IEEE.

Drexler, W., U. Morgner, F. Kärtner, C. Pitris, S. Boppart, X. Li, E. Ippen and J. Fujimoto (1999). "< i> In vivo</i> ultrahigh-resolution optical coherence tomography." Optics letters **24**(17): 1221-1223.

Dunn, A. K., C. Smithpeter, A. J. Welch and R. Richards-Kortum (1996). "Sources of contrast in confocal reflectance imaging." Applied optics **35**(19): 3441-3446.

Eckert, C. E., R. Fan, B. Mikulis, M. Barron, C. A. Carruthers, V. M. Friebe, N. R. Vyavahare and M. S. Sacks (2013). "On the biomechanical role of glycosaminoglycans in the aortic heart valve leaflet." Acta biomaterialia **9**(1): 4653-4660.

Edmunds, L. H., R. E. Clark, L. H. Cohn, G. L. Grunkemeier, D. C. Miller and R. D. Weisel (1996). "Guidelines for reporting morbidity and mortality after cardiac valvular operations." Asian Cardiovascular and Thoracic Annals **4**(2): 126-129.

Elston, C. W. and I. O. Ellis (1991). "Pathological prognostic factors in breast cancer. I. The value of histological grade in breast cancer: experience from a large study with long-term follow-up." Histopathology **19**(5): 403-410.

Erickson, T. A., A. Mazhar, D. J. Cuccia, A. J. Durkin and J. W. Tunnell (2010). "Lookup-table method for imaging optical properties with structured illumination beyond the diffusion theory regime." Journal of biomedical optics **15**(3): 036013.

Farrell, T. J., M. S. Patterson and B. Wilson (1992). "A diffusion theory model of spatially resolved, steady-state diffuse reflectance for the noninvasive determination of tissue optical properties invivo." Medical physics **19**(4): 879-888.

Feng, X., A. J. Moy, H. T. Nguyen, Y. Zhang, J. Zhang, M. C. Fox, K. R. Sebastian, J. S. Reichenberg, M. K. Markey and J. W. Tunnell (2018). "Raman biophysical markers in skin cancer diagnosis." Journal of biomedical optics **23**(5): 057002.

Flannery, B. P., H. W. Deckman, W. G. Roberge and K. L. D'AMICO (1987). "Three-dimensional X-ray microtomography." Science **237**(4821): 1439-1444.

Fung, Y.-C. (1990). Biomechanics, Springer.

Gelse, K., E. Pöschl and T. Aigner (2003). "Collagens—structure, function, and biosynthesis." Advanced drug delivery reviews **55**(12): 1531-1546.

Ghosh, N., P. K. Gupta, A. Pradhan and S. K. Majumder (2006). "Anomalous behavior of depolarization of light in a turbid medium." Physics Letters A **354**(3): 236-242.

Ghosh, N. and I. A. Vitkin (2011). "Tissue polarimetry: concepts, challenges, applications, and outlook." Journal of biomedical optics **16**(11): 110801-11080129.

Ghosh, N., I. A. Vitkin and M. F. Wood (2008). "Mueller matrix decomposition for extraction of individual polarization parameters from complex turbid media exhibiting multiple scattering, optical activity, and linear birefringence." Journal of biomedical optics **13**(4): 044036-044036-044014.

Ghosh, N., M. F. Wood, S. h. Li, R. D. Weisel, B. C. Wilson, R. K. Li and I. A. Vitkin (2009). "Mueller matrix decomposition for polarized light assessment of biological tissues." Journal of biophotonics **2**(3): 145-156.

Gilbert, T. W., S. Wognum, E. M. Joyce, D. O. Freytes, M. S. Sacks and S. F. Badylak (2008). "Collagen fiber alignment and biaxial mechanical behavior of porcine urinary bladder derived extracellular matrix." Biomaterials **29**(36): 4775-4782.

Gioux, S., A. Mazhar, D. J. Cuccia, A. J. Durkin, B. J. Tromberg and J. V. Frangioni (2009). "Three-dimensional surface profile intensity correction for spatially modulated imaging." Journal of biomedical optics **14**(3): 034045-034045-034011.

Gioux, S., A. Stockdale, R. Oketokoun, Y. Ashitate, N. J. Durr, L. A. Moffitt, J. V. Frangioni, A. Mazhar, B. J. Tromberg and A. J. Durkin (2011). "First-in-human pilot study of a spatial frequency domain oxygenation imaging system." Journal of biomedical optics **16**(8): 086015.

Gloster, J. H., K. R. Harris and R. K. Roenigk (1996). "A comparison between Mohs micrographic surgery and wide surgical excision for the treatment of dermatofibrosarcoma protuberans." Journal of the American Academy of Dermatology **35**(1): 82-87.

Goldberg, S. N., C. J. Grassi, J. F. Cardella, J. W. Charboneau, G. D. Dodd III, D. E. Dupuy, D. Gervais, A. R. Gillams, R. A. Kane and F. T. Lee Jr (2005). "Image-guided tumor ablation: standardization of terminology and reporting criteria." Journal of vascular and interventional radiology **16**(6): 765-778.

Goldstein, D. H. (2003). Polarized Light, revised and expanded, CRC press.

Göppert-Mayer, M. (1931). "Über elementarakte mit zwei quantensprüngen." Annalen der Physik **401**(3): 273-294.

Goth, W., J. Lesicko, M. S. Sacks and J. W. Tunnell (2016). "Optical-Based Analysis of Soft Tissue Structures." Annual Review of Biomedical Engineering **18**(1): null.

Goth, W., B. Yang, J. Lesicko, A. Allen, M. S. Sacks and J. W. Tunnell (2016). Polarized spatial frequency domain imaging of heart valve fiber structure. SPIE BiOS, International Society for Optics and Photonics.

Goth, W., B. Yang, J. Lesicko, R. Stevens, M. Sacks and J. W. Tunnell (2015). Polarized spatial frequency domain imaging of soft tissue fiber distributions. Engineering Conferences International, Vail, CO.

Guo, X., M. F. Wood and A. Vitkin (2007). "Monte Carlo study of pathlength distribution of polarized light in turbid media." Optics express **15**(3): 1348-1360.

Guo, X., M. F. Wood and A. Vitkin (2008). "A Monte Carlo study of penetration depth and sampling volume of polarized light in turbid media." Optics Communications **281**(3): 380-387.

Haacke, E. M., R. W. Brown, M. R. Thompson and R. Venkatesan (1999). "Magnetic resonance imaging." Physical principles and sequence design.

Haskell, R. C., L. O. Svaasand, T.-T. Tsay, T.-C. Feng, M. S. McAdams and B. J. Tromberg (1994). "Boundary conditions for the diffusion equation in radiative transfer." JOSA A **11**(10): 2727-2741.

Hayakawa, C. K., K. Karrobi, V. Pera, D. Roblyer and V. Venugopalan (2018). "Optical sampling depth in the spatial frequency domain." Journal of biomedical optics **24**(7): 071603.

He, H., M. Sun, N. Zeng, E. Du, S. Liu, Y. Guo, J. Wu, Y. He and H. Ma (2014). "Mapping local orientation of aligned fibrous scatterers for cancerous tissues using backscattering Mueller matrix imaging." Journal of biomedical optics **19**(10): 106007-106007.

HealthJade (2018). Heart Valve Stenosis. https://healthjade.com/aortic-valve-stenosis/.

Helmchen, F. and W. Denk (2005). "Deep tissue two-photon microscopy." Nature methods **2**(12): 932-940.

Hodgkin, D. and J. Lister (1827). "XXVI. Notice of some miscroscopic observations of the blood and animal tissues." The Philosophical Magazine, or Annals of Chemistry, Mathematics, Astronomy, Natural History and General Science **2**(8): 130-138.

Hotaling, N. A., K. Bharti, H. Kriel and C. G. Simon (2015). "DiameterJ: a validated open source nanofiber diameter measurement tool." Biomaterials **61**: 327-338.

Hsieh, J. (2009). Computed tomography: principles, design, artifacts, and recent advances, SPIE Bellingham, WA.

Huang, D., E. A. Swanson, C. P. Lin, J. S. Schuman, W. G. Stinson, W. Chang, M. R. Hee, T. Flotte, K. Gregory and C. A. Puliafito (1991). "Optical coherence tomography." Science **254**(5035): 1178-1181.

Hull, E. L. and T. H. Foster (2001). "Steady-state reflectance spectroscopy in the P 3 approximation." JOSA A **18**(3): 584-599.

Hulst, H. C. and H. Van De Hulst (1957). Light scattering by small particles, Courier Dover Publications.

Ishimaru, A. (1989). "Diffusion of light in turbid material." Applied optics **28**(12): 2210-2215.

Iung, B. and A. Vahanian (2011). "Epidemiology of valvular heart disease in the adult." Nature Reviews Cardiology **8**(3): 162-172.

Ivančič, M., P. Naglič, F. Pernuš, B. Likar and M. Bürmen (2018). "Efficient estimation of subdiffusive optical parameters in real time from spatially resolved reflectance by artificial neural networks." Optics letters **43**(12): 2901-2904.

Jacques, S. L. (2013). "Optical properties of biological tissues: a review." Physics in medicine and biology **58**(11): R37.

Jacques, S. L. and B. W. Pogue (2008). "Tutorial on diffuse light transport." Journal of Biomedical Optics **13**(4): 041302-041302-041319.

Jacques, S. L. and J. C. Ramella-Roman (2004). Polarized light imaging of tissues, Royal Society of Chemistry**:** 591-607.

Jacques, S. L., J. C. Ramella-Roman and K. Lee (2002). "Imaging skin pathology with polarized light." Journal of biomedical optics **7**(3): 329-340.

Jacques, S. L., J. R. Roman and K. Lee (2000). "Imaging superficial tissues with polarized light." Lasers in surgery and medicine **26**(2): 119-129.

Joyce, E. M., J. Liao, F. J. Schoen, J. E. Mayer Jr and M. S. Sacks (2009). "Functional collagen fiber architecture of the pulmonary heart valve cusp." The Annals of thoracic surgery **87**(4): 1240-1249.

Kaiser, W. and C. Garrett (1961). "Two-Photon Excitation in Ca F 2: Eu 2+." Physical Review Letters **7**(6): 229.

Kanick, S. C., D. M. McClatchy, V. Krishnaswamy, J. T. Elliott, K. D. Paulsen and B. W. Pogue (2014). "Sub-diffusive scattering parameter maps recovered using wide-field high-frequency structured light imaging." Biomedical optics express **5**(10): 3376-3390.

Keller, E. and R. Goldman (2006). Light Microscopy, 8, Cold Spring Harbor Laboratory Press, Woodbury, NY.

Kemp, N., H. Zaatari, J. Park, H. G. Rylander III and T. Milner (2005). "Form-biattenuance in fibrous tissues measured with polarization-sensitive optical coherence tomography (PS-OCT)." Optics express **13**(12): 4611-4628.

Kienle, A., L. Lilge, M. S. Patterson, R. Hibst, R. Steiner and B. C. Wilson (1996). "Spatially resolved absolute diffuse reflectance measurements for noninvasive determination of the optical scattering and absorption coefficients of biological tissue." Applied optics **35**(13): 2304-2314.

Kim, K. H., C. Buehler and P. T. C. So (1999). "High-speed, two-photon scanning microscope." Applied optics (2004) **38**(28): 6004-6009.

Kinsey, J. L. (1977). "Laser-induced fluorescence." Annual Review of Physical Chemistry **28**(1): 349-372.

Kolarsick, P. A., M. A. Kolarsick and C. Goodwin (2011). "Anatomy and physiology of the skin." Journal of the Dermatology Nurses' Association **3**(4): 203-213.

Kondinski, A. (2010). Picture of solution containing gold nanoparticles. Gold255.jpg. https://kondinski.webs.com.

Konecky, S. D., A. Mazhar, D. Cuccia, A. J. Durkin, J. C. Schotland and B. J. Tromberg (2009). "Quantitative optical tomography of sub-surface heterogeneities using spatially modulated structured light." Optics express **17**(17): 14780-14790.

Kuhn, J. R. and M. Poenie (2002). "Dynamic polarization of the microtubule cytoskeleton during CTL-mediated killing." Immunity **16**(1): 111-121.

Laughney, A. M., V. Krishnaswamy, T. B. Rice, D. J. Cuccia, R. J. Barth, B. J. Tromberg, K. D. Paulsen, B. W. Pogue and W. A. Wells (2013). "System analysis of spatial frequency domain imaging for quantitative mapping of surgically resected breast tissues." Journal of biomedical optics **18**(3): 036012.

Laughney, A. M., V. Krishnaswamy, E. J. Rizzo, M. C. Schwab, R. J. Barth, D. J. Cuccia, B. J. Tromberg, K. D. Paulsen, B. W. Pogue and W. A. Wells (2013). "Spectral discrimination of breast pathologies in situ using spatial frequency domain imaging." Breast Cancer Research **15**(4): R61.

Lauterbur, P. C. (1973). "Image formation by induced local interactions: examples employing nuclear magnetic resonance." Nature **242**(5394): 190-191.

Lee, C.-H. and M. S. Sacks (2016). Fibers to organs: how collagen fiber properties modulate the closing behavior of the mitral valve. Structure-Based Mechanics of Tissues and Organs, Springer**:** 365-381.

Leiter, U., T. Eigentler and C. Garbe (2014). Epidemiology of skin cancer. Sunlight, vitamin D and skin cancer, Springer**:** 120-140.

Liao, R., X. Jiang, Y. He, H. Ma, D. Li, N. Zeng and T. Yun (2010). "Rotating linear polarization imaging technique for anisotropic tissues." Journal of biomedical optics **15**(3): 036014-036014-036016.

Lin, A. J., M. A. Koike, K. N. Green, J. G. Kim, A. Mazhar, T. B. Rice, F. M. LaFerla and B. J. Tromberg (2011). "Spatial frequency domain imaging of intrinsic optical property contrast in a mouse model of Alzheimer's disease." Annals of biomedical engineering **39**(4): 1349-1357.

Lin, W., B. Zeng, Z. Cao, X. Chen, K. Yang and M. Xu (2018). "Quantitative diagnosis of tissue microstructure with wide-field high spatial frequency domain imaging." Biomedical Optics Express **9**(7): 2905-2916.

Liu, L., J. A. Gardecki, S. K. Nadkarni, J. D. Toussaint, Y. Yagi, B. E. Bouma and G. J. Tearney (2011). "Imaging the subcellular structure of human coronary atherosclerosis using micro-optical coherence tomography." Nature medicine **17**(8): 1010-1014.

Long, D. A. and D. Long (1977). Raman spectroscopy, McGraw-Hill New York.

Lu, S.-Y. and R. A. Chipman (1996). "Interpretation of Mueller matrices based on polar decomposition." JOSA A **13**(5): 1106-1113.

Lu, Y., R. Li and R. Lu (2016). "Fast demodulation of pattern images by spiral phase transform in structured-illumination reflectance imaging for detection of bruises in apples." Computers and Electronics in Agriculture **127**: 652-658.

Lu, Y., R. Li and R. Lu (2016). "Gram–Schmidt orthonormalization for retrieval of amplitude images under sinusoidal patterns of illumination." Applied optics **55**(25): 6866-6873.

Madan, V., J. T. Lear and R.-M. Szeimies (2010). "Non-melanoma skin cancer." The Lancet **375**(9715): 673-685.

Marieb, E. N. and K. Hoehn (2007). Human anatomy & physiology, Pearson Education.

Mark, J. E. (2007). Physical properties of polymers handbook, Springer.

Mazhar, A., D. J. Cuccia, S. Gioux, A. J. Durkin, J. V. Frangioni and B. J. Tromberg (2010). "Structured illumination enhances resolution and contrast in thick tissue fluorescence imaging." Journal of biomedical optics **15**(1): 010506.

Mazhar, A., S. Dell, D. J. Cuccia, S. Gioux, A. J. Durkin, J. V. Frangioni and B. J. Tromberg (2010). "Wavelength optimization for rapid chromophore mapping using spatial frequency domain imaging." Journal of biomedical optics **15**(6): 061716.

Mazhar, A., S. Saggese, A. C. Pollins, N. L. Cardwell, L. B. Nanney and D. J. Cuccia (2014). "Noncontact imaging of burn depth and extent in a porcine model using spatial frequency domain imaging." Journal of biomedical optics **19**(8): 086019.

McClatchy, D. M., E. J. Rizzo, W. A. Wells, C. C. Black, K. D. Paulsen, S. C. Kanick and B. W. Pogue (2018). "Light scattering measured with spatial frequency domain imaging can predict stromal versus epithelial proportions in surgically resected breast tissue." Journal of biomedical optics **24**(7): 071605.

McClatchy, D. M., E. J. Rizzo, W. A. Wells, P. P. Cheney, J. C. Hwang, K. D. Paulsen, B. W. Pogue and S. C. Kanick (2016). "Wide-field quantitative imaging of tissue microstructure using sub-diffuse spatial frequency domain imaging." Optica **3**(6): 613-621.

McClatchy III, D. M., P. J. Hoopes, B. W. Pogue and S. C. Kanick (2017). "Monochromatic subdiffusive spatial frequency domain imaging provides in-situ sensitivity to intratumoral morphological heterogeneity in a murine model." Journal of biophotonics **10**(2): 211-216.

McGuire, J. F., N. G. Norman and S. Dyson (2009). "Nonmelanoma skin cancer of the head and neck I: histopathology and clinical behavior." American journal of otolaryngology **30**(2): 121-133.

Mega, Y., M. Robitaille, R. Zareian, J. McLean, J. Ruberti and C. DiMarzio (2012). "Quantification of lamellar orientation in corneal collagen using second harmonic generation images." Optics letters **37**(16): 3312-3314.

Mie, G. (1908). "Beiträge zur Optik trüber Medien, speziell kolloidaler Metallösungen." Annalen der physik **330**(3): 377-445.

Minsky, M. (1961). Microscopy apparatus, Google Patents.

Misfeld, M. and H.-H. Sievers (2007). "Heart valve macro-and microstructure." Philosophical Transactions of the Royal Society of London B: Biological Sciences **362**(1484): 1421-1436.

Movasaghi, Z., S. Rehman and I. U. Rehman (2007). "Raman spectroscopy of biological tissues." Applied Spectroscopy Reviews **42**(5): 493-541.

Murray, J. M. (2005). "Confocal microscopy, deconvolution, and structured illumination methods." Live Cell Imaging—A Laboratory Manual. RD Goldman and DL Spector, editors. Cold Spring Harbor Laboratory Press, Cold Spring Harbor, NY: 239-279.

Nadeau, K. P., A. J. Durkin and B. J. Tromberg (2014). "Advanced demodulation technique for the extraction of tissue optical properties and structural orientation contrast in the spatial frequency domain." Journal of biomedical optics **19**(5): 056013-056013.

Nadeau, K. P., T. B. Rice, A. J. Durkin and B. J. Tromberg (2015). "Multifrequency synthesis and extraction using square wave projection patterns for quantitative tissue imaging." Journal of biomedical optics **20**(11): 116005-116005.

Naglič, P., F. Pernuš, B. Likar and M. Bürmen (2017). "Lookup table-based sampling of the phase function for Monte Carlo simulations of light propagation in turbid media." Biomedical optics express **8**(3): 1895-1910.

Nehal, K. S., D. Gareau and M. Rajadhyaksha (2008). Skin imaging with reflectance confocal microscopy. Seminars in cutaneous medicine and surgery, WB Saunders.

Nie, S. and S. R. Emory (1997). "Probing single molecules and single nanoparticles by surface-enhanced Raman scattering." science **275**(5303): 1102-1106.

Nkomo, V. T., J. M. Gardin, T. N. Skelton, J. S. Gottdiener, C. G. Scott and M. Enriquez-Sarano (2006). "Burden of valvular heart diseases: a population-based study." The Lancet **368**(9540): 1005-1011.

O'Sullivan, T. D., A. E. Cerussi, B. J. Tromberg and D. J. Cuccia (2012). "Diffuse optical imaging using spatially and temporally modulated light." Journal of biomedical optics **17**(7): 071311.

Osnabrugge, R. L., D. Mylotte, S. J. Head, N. M. Van Mieghem, V. T. Nkomo, C. M. LeReun, A. J. Bogers, N. Piazza and A. P. Kappetein (2013). "Aortic stenosis in the elderly: disease prevalence and number of candidates for transcatheter aortic valve replacement: a meta-analysis and modeling study." Journal of the American College of Cardiology **62**(11): 1002-1012.

Parry, D. A. (1988). "The molecular fibrillar structure of collagen and its relationship to the mechanical properties of connective tissue." Biophysical chemistry **29**(1): 195-209.

Patterson, G. H. and D. W. Piston (2000). "Photobleaching in two-photon excitation microscopy." Biophysical journal **78**(4): 2159-2162.

Patton, K. T. and G. A. Thibodeau (2014). Mosby's Handbook of Anatomy & Physiology-E-Book, Elsevier Health Sciences.

Pawley, J. (2010). Handbook of biological confocal microscopy, Springer.

Pibarot, P. and J. G. Dumesnil (2009). "Prosthetic heart valves selection of the optimal prosthesis and long-term management." Circulation **119**(7): 1034-1048.

Pircher, M., E. Götzinger, R. Leitgeb, H. Sattmann, O. Findl and C. K. Hitzenberger (2004). "Imaging of polarization properties of human retina in vivo with phase resolved transversal PS-OCT." Optics Express **12**(24): 5940-5951.

Ponticorvo, A., D. M. Burmeister, B. Yang, B. Choi, R. J. Christy and A. J. Durkin (2014). "Quantitative assessment of graded burn wounds in a porcine model using spatial frequency domain imaging (SFDI) and laser speckle imaging (LSI)." Biomedical optics express **5**(10): 3467-3481.

Ponticorvo, A., E. Taydas, A. Mazhar, T. Scholz, H.-S. Kim, J. Rimler, G. R. Evans, D. J. Cuccia and A. J. Durkin (2013). "Quantitative assessment of partial vascular occlusions in

a swine pedicle flap model using spatial frequency domain imaging." Biomedical optics express **4**(2): 298-306.

Prasad, P. N. and D. J. Williams (1991). Introduction to nonlinear optical effects in molecules and polymers, Wiley New York etc.

Prasad, P. V. (2006). Magnetic resonance imaging: methods and biologic applications, Springer.

Qi, J. and D. S. Elson (2017). "Mueller polarimetric imaging for surgical and diagnostic applications: a review." Journal of biophotonics **10**(8): 950-982.

Rajadhyaksha, M., R. Anderson and R. H. Webb (1999). "Video-Rate Confocal Scanning Laser Microscope for Imaging Human Tissues< i> In Vivo</i>." Applied optics **38**(10): 2105-2115.

Ramella-Roman, J. C., K. Lee, S. A. Prahl and S. L. Jacques (2004). "Design, testing, and clinical studies of a handheld polarized light camera." Journal of Biomedical Optics **9**(6): 1305-1310.

Rohrbach, D. J., D. Muffoletto, J. Huihui, R. Saager, K. Keymel, A. Paquette, J. Morgan, N. Zeitouni and U. Sunar (2014). "Preoperative mapping of nonmelanoma skin cancer using spatial frequency domain and ultrasound imaging." Academic radiology **21**(2): 263-270.

Rubart, M. (2004). "Two-photon microscopy of cells and tissue." Circulation research **95**(12): 1154-1166.

Sacks, M. S. (2000). "Biaxial mechanical evaluation of planar biological materials." Journal of elasticity and the physical science of solids **61**(1-3): 199-246.

Sacks, M. S. (2003). "Incorporation of experimentally-derived fiber orientation into a structural constitutive model for planar collagenous tissues." Journal of biomechanical engineering **125**(2): 280-287.

Sacks, M. S. and F. J. Schoen (2002). "Collagen fiber disruption occurs independent of calcification in clinically explanted bioprosthetic heart valves." Journal of biomedical materials research **62**(3): 359-371.

Sacks, M. S., F. J. Schoen and J. E. Mayer Jr (2009). "Bioengineering challenges for heart valve tissue engineering." Annual review of biomedical engineering **11**: 289-313.

Sacks, M. S., D. B. Smith and E. D. Hiester (1997). "A small angle light scattering device for planar connective tissue microstructural analysis." Annals of biomedical engineering **25**(4): 678-689.

Sandberg, L. B., N. T. Soskel and J. G. Leslie (1981). "Elastin structure, biosynthesis, and relation to disease states." New England Journal of Medicine **304**(10): 566-579.

Schoen, F., R. Levy, A. Nelson, W. Bernhard, A. Nashef and M. Hawley (1985). "Onset and progression of experimental bioprosthetic heart valve calcification." Laboratory investigation; a journal of technical methods and pathology **52**(5): 523-532.

Schoen, F. J. and R. J. Levy (2005). "Calcification of tissue heart valve substitutes: progress toward understanding and prevention." The Annals of thoracic surgery **79**(3): 1072-1080.

Sexton, M., D. B. Jones and M. E. Maloney (1990). "Histologic pattern analysis of basal cell carcinoma: study of a series of 1039 consecutive neoplasms." Journal of the American Academy of Dermatology **23**(6): 1118-1126.

Shriner, D. L., D. K. McCoy, D. J. Goldberg and R. F. Wagner Jr (1998). "Mohs micrographic surgery." Journal of the American Academy of Dermatology **39**(1): 79-97.

Shung, K. K. and G. A. Thieme (1992). Ultrasonic scattering in biological tissues, CRC Press.

Singhal, P., A. Luk and J. Butany (2013). "Bioprosthetic heart valves: impact of implantation on biomaterials." ISRN Biomaterials **2013**.

SkinCancerFoundation (2018). Mohs Surgery Step-by-Step. MohsBro-web-illo-3. https://www.skincancer.org/skin-cancer-information/mohs-surgery/step-by-step, Skin Cancer Foundation.

Smeets, N., D. Kuijpers, P. Nelemans, J. Ostertag, M. Verhaegh, G. Krekels and H. Neumann (2004). "Mohs' micrographic surgery for treatment of basal cell carcinoma of the face——results of a retrospective study and review of the literature." British journal of dermatology **151**(1): 141-147.

Smith-Bindman, R., J. Lipson, R. Marcus, K.-P. Kim, M. Mahesh, R. Gould, A. B. de González and D. L. Miglioretti (2009). "Radiation dose associated with common computed tomography examinations and the associated lifetime attributable risk of cancer." Archives of internal medicine **169**(22): 2078-2086.

Smith, C. R., M. B. Leon, M. J. Mack, D. C. Miller, J. W. Moses, L. G. Svensson, E. M. Tuzcu, J. G. Webb, G. P. Fontana and R. R. Makkar (2011). "Transcatheter versus surgical aortic-valve replacement in high-risk patients." New England Journal of Medicine **364**(23): 2187-2198.

Smithpeter, C. L., A. K. Dunn, A. Welch and R. Richards-Kortum (1998). "Penetration Depth Limits of< i> In Vivo</i> Confocal Reflectance Imaging." Applied optics **37**(13): 2749-2754.

So, P. T., C. Y. Dong, B. R. Masters and K. M. Berland (2000). "Two-photon excitation fluorescence microscopy." Annual review of biomedical engineering **2**(1): 399-429.

Srinivasan, V., H.-C. Liu and M. Halioua (1984). "Automated phase-measuring profilometry of 3-D diffuse objects." Applied optics **23**(18): 3105-3108.

Star, W. M. (1995). Diffusion theory of light transport. Optical-thermal response of laser-irradiated tissue, Springer**:** 131-206.

Stella, J. A., J. Liao and M. S. Sacks (2007). "Time-dependent biaxial mechanical behavior of the aortic heart valve leaflet." Journal of biomechanics **40**(14): 3169-3177.

Stella, J. A. and M. S. Sacks (2007). "On the biaxial mechanical properties of the layers of the aortic valve leaflet." Journal of biomechanical engineering **129**(5): 757-766.

Stoller, P., K. M. Reiser, P. M. Celliers and A. M. Rubenchik (2002). "Polarization-modulated second harmonic generation in collagen." Biophysical journal **82**(6): 3330-3342.

Sun, M., H. He, N. Zeng, E. Du, Y. Guo, S. Liu, J. Wu, Y. He and H. Ma (2014). "Characterizing the microstructures of biological tissues using Mueller matrix and transformed polarization parameters." Biomedical optics express **5**(12): 4223-4234.

Sun, W. and P. Lal (2002). "Recent development on computer aided tissue engineering—a review." Computer methods and programs in biomedicine **67**(2): 85-103.

Sun, W., M. S. Sacks, T. L. Sellaro, W. S. Slaughter and M. J. Scott (2003). "Biaxial mechanical response of bioprosthetic heart valve biomaterials to high in-plane shear." Journal of biomechanical engineering **125**(3): 372-380.

Tearney, G., M. Brezinski, J. Fujimoto, N. Weissman, S. Boppart, B. Bouma and J. Southern (1996). "Scanning single-mode fiber optic catheter–endoscope for optical coherence tomography." Optics Letters **21**(7): 543-545.

Tearney, G. J., M. E. Brezinski, B. E. Bouma, S. A. Boppart, C. Pitris, J. F. Southern and J. G. Fujimoto (1997). "In vivo endoscopic optical biopsy with optical coherence tomography." Science **276**(5321): 2037-2039.

Teh, I., D. McClymont, R. A. Burton, M. L. Maguire, H. J. Whittington, C. A. Lygate, P. Kohl and J. E. Schneider (2016). "Resolving fine cardiac structures in rats with high-resolution diffusion tensor imaging." Scientific reports **6**: 30573.

Tower, T. T., M. R. Neidert and R. T. Tranquillo (2002). "Fiber alignment imaging during mechanical testing of soft tissues." Annals of biomedical engineering **30**(10): 1221-1233.

Tranquart, F., N. Grenier, V. Eder and L. Pourcelot (1999). "Clinical use of ultrasound tissue harmonic imaging." Ultrasound in medicine & biology **25**(6): 889-894.

Tuchin, V. V. (2007). Tissue optics: light scattering methods and instruments for medical diagnosis, SPIE press Bellingham.

Valdes, P. A., J. P. Angelo, H. S. Choi and S. Gioux (2017). "qF-SSOP: real-time optical property corrected fluorescence imaging." Biomedical optics express **8**(8): 3597-3605.

Vannier, M. W. and J. L. Marsh (1996). "Three-dimensional imaging, surgical planning, and image-guided therapy." Radiologic Clinics of North America **34**(3): 545-563.

Vargas, J., J. A. Quiroga, C. Sorzano, J. Estrada and J. Carazo (2012). "Two-step demodulation based on the Gram–Schmidt orthonormalization method." Optics letters **37**(3): 443-445.

Vedrine, P., G. Aubert, F. Beaudet, J. Belorgey, J. Beltramelli, C. Berriaud, P. Bredy, P. Chesny, A. Donati and G. Gilgrass (2008). "The whole body 11.7 T MRI magnet for Iseult/INUMAC project." Applied Superconductivity, IEEE Transactions on **18**(2): 868-873.

Vervandier, J. and S. Gioux (2013). "Single snapshot imaging of optical properties." Biomedical optics express **4**(12): 2938-2944.

Vesely, I. (2003). "The evolution of bioprosthetic heart valve design and its impact on durability." Cardiovascular Pathology **12**(5): 277-286.

Vyavahare, N., D. Hirsch, E. Lerner, J. Z. Baskin, F. J. Schoen, R. Bianco, H. S. Kruth, R. Zand and R. J. Levy (1997). "Prevention of bioprosthetic heart valve calcification by ethanol preincubation efficacy and mechanisms." Circulation **95**(2): 479-488.

Vyavahare, N., M. Ogle, F. J. Schoen, R. Zand, D. C. Gloeckner, M. Sacks and R. J. Levy (1999). "Mechanisms of bioprosthetic heart valve failure: fatigue causes collagen denaturation and glycosaminoglycan loss." Journal of biomedical materials research **46**(1): 44-50.

Walley, V. M., C. A. Keon, M. Khalili, D. Moher, M. Campagna and W. J. Keon (1992). "Ionescu-Shiley valve failure I: experience with 125 standard-profile explants." The Annals of thoracic surgery **54**(1): 111-116.

Wang, L. V. and H.-i. Wu (2012). Biomedical optics: principles and imaging, John Wiley & Sons.

Wang, X.-j., T. E. Milner, M. C. Chang and J. S. Nelson (1996). "Group refractive index measurement of dry and hydrated type I collagen films using optical low-coherence reflectometry." Journal of biomedical optics **1**(2): 212-216.

Wax, A., C. Yang, V. Backman, K. Badizadegan, C. W. Boone, R. R. Dasari and M. S. Feld (2002). "Cellular organization and substructure measured using angle-resolved low-coherence interferometry." Biophysical journal **82**(4): 2256-2264.

Whittaker, P. and P. B. Canham (1991). "Demonstration of quantitative fabric analysis of tendon collagen using two-dimensional polarized light microscopy." Matrix **11**(1): 56-62.

Wiest, J., N. Bodenschatz, A. Brandes, A. Liemert and A. Kienle (2015). "Polarization influence on reflectance measurements in the spatial frequency domain." Physics in medicine and biology **60**(15): 5717.

Wilson, T. (1990). "Confocal microscopy." Academic Press: London, etc **426**: 1-64.

Wirth, D., M. Sibai, J. Olson, B. C. Wilson, D. W. Roberts and K. Paulsen (2018). "Feasibility of using spatial frequency-domain imaging intraoperatively during tumor resection." Journal of biomedical optics **24**(7): 071608.

Wood, M. F., N. Ghosh, E. H. Moriyama, B. C. Wilson and I. A. Vitkin (2009). "Proof-of-principle demonstration of a Mueller matrix decomposition method for polarized light tissue characterization in vivo." Journal of biomedical optics **14**(1): 014029-014029-014025.

Xing, L., B. Thorndyke, E. Schreibmann, Y. Yang, T.-F. Li, G.-Y. Kim, G. Luxton and A. Koong (2006). "Overview of image-guided radiation therapy." Medical Dosimetry **31**(2): 91-112.

Yafi, A., F. K. Muakkassa, T. Pasupneti, J. Fulton, D. J. Cuccia, A. Mazhar, K. N. Blasiole and E. N. Mostow (2017). "Quantitative skin assessment using spatial frequency domain imaging (SFDI) in patients with or at high risk for pressure ulcers." Lasers in surgery and medicine **49**(9): 827-834.

Yafi, A., T. S. Vetter, T. Scholz, S. Patel, R. B. Saager, D. J. Cuccia, G. R. Evans and A. J. Durkin (2011). "Postoperative quantitative assessment of reconstructive tissue status in cutaneous flap model using spatial frequency domain imaging." Plastic and reconstructive surgery **127**(1): 117.

Yang, B., J. Lesicko, M. Sharma, M. Hill, M. Sacks and J. W. Tunnell (2014). Collagen Fiber Orientation Mapping with Top Layer Discrimination using Polarized Light Spatial Frequency Domain Imaging (pSFDI) on Native Heart Tissue. Biomedical Optics, Optical Society of America.

Yang, B., J. Lesicko, M. Sharma, M. Hill, M. S. Sacks and J. W. Tunnell (2015). "Polarized light spatial frequency domain imaging for non-destructive quantification of soft tissue fibrous structures." Biomedical optics express **6**(4): 1520-1533.

Yang, B., M. Sharma and J. W. Tunnell (2013). "Attenuation-corrected fluorescence extraction for image-guided surgery in spatial frequency domain." Journal of biomedical optics **18**(8): 080503.

Zhang, W. and M. S. Sacks (2017). "Modeling the response of exogenously crosslinked tissue to cyclic loading: The effects of permanent set." Journal of the mechanical behavior of biomedical materials **75**: 336-350.

Zhou, W.-S. and X.-Y. Su (1994). "A direct mapping algorithm for phase-measuring profilometry." Journal of modern optics **41**(1): 89-94.

Zipfel, W. R., R. M. Williams, R. Christie, A. Y. Nikitin, B. T. Hyman and W. W. Webb (2003). "Live tissue intrinsic emission microscopy using multiphoton-excited native fluorescence and second harmonic generation." Proceedings of the National Academy of Sciences **100**(12): 7075-7080.